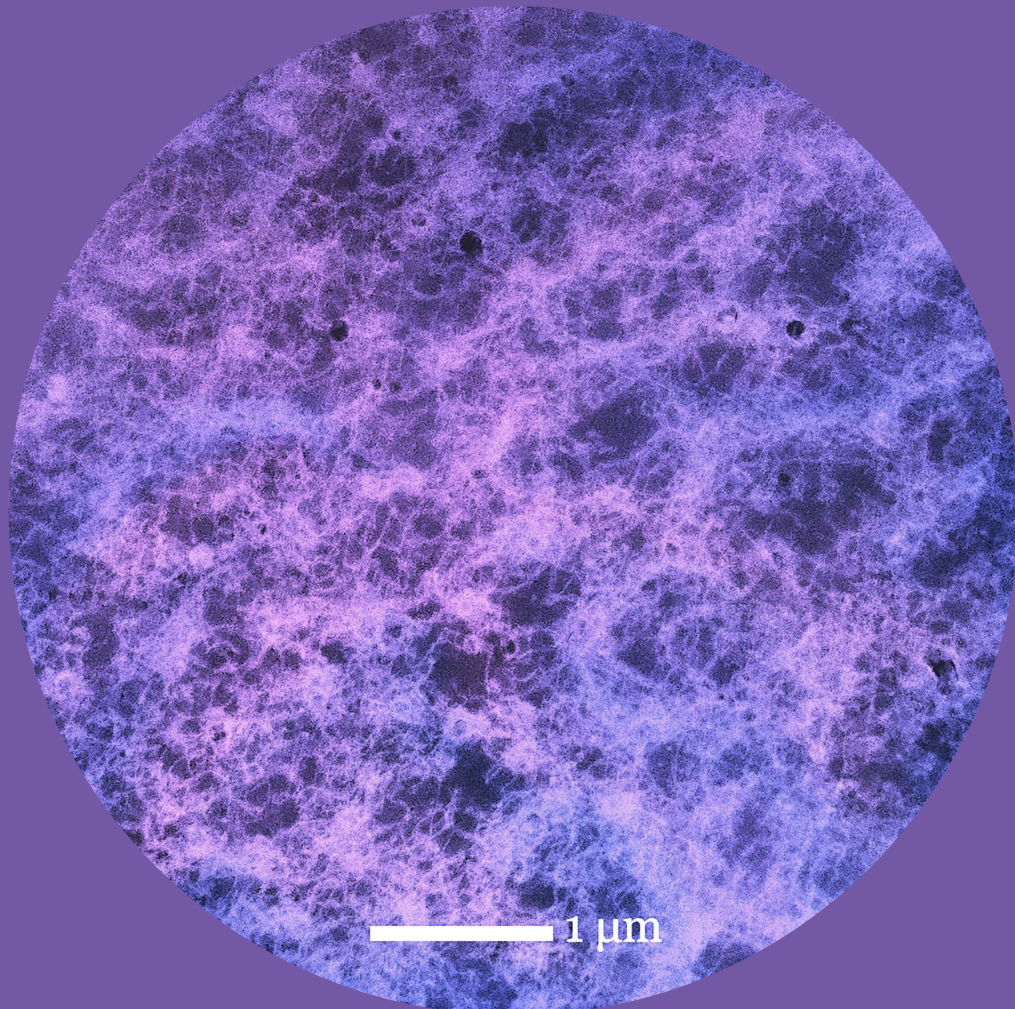


# Control of microstructure and properties of Cr-Fe-Ni based multicomponent alloys

---

Xuan Yang



# Control of microstructure and properties of Cr-Fe-Ni based multicomponent alloys

**Xuan Yang**

A doctoral dissertation completed for the degree of Doctor of Science (Technology) to be defended, with the permission of the Aalto University School of Chemical Engineering, at a public examination held at the lecture hall Ke2 of the school on 28th January 2022 at 1:00 p.m.

**Aalto University  
School of Chemical Engineering  
Department of Chemistry and Materials Science  
Advanced and Functional Materials**

**Supervising professor**

Professor Jari Koskinen, Aalto University, Finland

**Thesis advisors**

Professor Emeritus Simo-Pekka Hannula, Aalto University, Finland

D.Sc. (Tech.) Yanling Ge, VTT Technical Research Centre of Finland, Finland

**Preliminary examiners**

Professor Pasi Peura, Tampere University, Finland

Professor Antti Salminen, University of Turku, Finland

**Opponent**

Professor Sheng Guo, Chalmers University of Technology, Sweden

Aalto University publication series

**DOCTORAL DISSERTATIONS 1/2022**

© 2022 Xuan Yang

ISBN 978-952-64-0652-7 (printed)

ISBN 978-952-64-0653-4 (pdf)

ISSN 1799-4934 (printed)

ISSN 1799-4942 (pdf)

<http://urn.fi/URN:ISBN:978-952-64-0653-4>

Images: cover image by Xuan Yang

Unigrafia Oy  
Helsinki 2022

Finland



Printed matter  
4041-0619

**Author**

Xuan Yang

**Name of the doctoral dissertation**

Control of microstructure and properties of Cr-Fe-Ni based multicomponent alloys

**Publisher** School of Chemical Engineering**Unit** Department of Chemistry and Materials Science**Series** Aalto University publication series DOCTORAL DISSERTATIONS 1/2022**Field of research** Materials Science**Manuscript submitted** 9 November 2021**Date of the defence** 28 January 2022**Permission for public defence granted (date)** 15 December 2021**Language** English **Monograph** **Article dissertation** **Essay dissertation****Abstract**

Traditional metal alloys have been well developed for years, while less and less are left to be explored. In this context multicomponent alloys present an innovative alloy design strategy that breaks through the limitations of traditional design framework, and is shown to result in excellent physical and chemical properties. This thesis focuses on two kinds of multicomponent alloys, i.e., equiatomic CrMnFeNi alloy and non-equiatomic AlCoCr<sub>0.75</sub>Cu<sub>0.5</sub>FeNi alloy. Laser powder bed fusion (LPBF) is employed to carry out the fabrication of bulk alloys from gas-atomized powder. The influence of process parameters on the microstructure has been determined, and properties in relation to microstructural changes have been evaluated. Particularly, concerning possible target applications, hydrogen effects and magnetic behavior have been investigated on LPBF-built CrMnFeNi and AlCoCr<sub>0.75</sub>Cu<sub>0.5</sub>FeNi alloy, respectively.

It is found that CrMnFeNi alloy produced by LPBF shows a single face-centered cubic (FCC) phase structure, owing to the favored FCC formation in rapid solidification during LPBF process. A hierarchical microstructure constituting of melt pools, grains, cellular structures including dendritic, elongated and equiaxed cells, as well as ultrafine sub-cells, has been observed. A large density of dislocations in association with segregation of Mn and Ni has been detected in the boundaries of melt pools, grains and cellular structures. When employing the same laser power, a faster scanning speed leads to a formation of more homogeneous and refined microstructure, accordingly, a higher Vickers hardness of 248 ± 8 HV<sub>0.5</sub> is achieved. In hydrogen-charged TEM sample, hydrogen-induced planar faults, cracks and nanocrystals are identified. Absorbed hydrogen concentration is nearly 20 times higher than conventional austenitic stainless steel, which is attributed to both multicomponent alloy design strategy and LPBF process.

AlCoCr<sub>0.75</sub>Cu<sub>0.5</sub>FeNi alloy is fabricated by LPBF applying two sets of process parameters. Laser power, scanning speed and volumetric energy density contribute to different aspects during the manufacturing, thus they need to be properly optimized. Typical rapidly solidified hierarchical microstructure is also characterized. A high Vickers microhardness of 604.6 ± 6.8 HV<sub>0.05</sub> is measured regardless of the defects present. The degree of spinodal decomposition into two types of body-centered cubic (BCC) phase structures, i.e., A<sub>2</sub> and B<sub>2</sub> phase, has been found to depend on cooling rate, that is, A<sub>2</sub> phase formation is promoted under a relatively slower rate during rapid solidification. As the slowest scanning speed is employed under the same laser power, the largest saturation magnetization of 65.3 emu/g at 9 T and 300 K is reached. The control and enhancement of magnetic properties can be easily conducted via spinodal decomposition by optimizing process parameters in LPBF process.

Findings of this thesis demonstrate the feasibility and potentiality of manufacturing multicomponent alloys by LPBF process, which provides benefits for the development of new alloys for advanced applications in the future.

**Keywords** high entropy alloys; laser powder bed fusion; selective laser melting; solidification microstructure; hydrogen charging; magnetic properties

**ISBN (printed)** 978-952-64-0652-7**ISBN (pdf)** 978-952-64-0653-4**ISSN (printed)** 1799-4934**ISSN (pdf)** 1799-4942**Location of publisher** Helsinki**Location of printing** Helsinki**Year** 2022**Pages** 132**urn** <http://urn.fi/URN:ISBN:978-952-64-0653-4>



# Acknowledgements

This doctoral dissertation has been conducted in years 2017-2021 at the group of Advanced and Functional Materials, Department of Chemistry and Materials Science, Aalto University School of Chemical Engineering. The support of China Scholarship Council fellowship (grant number 201706040062), Foundation for Aalto University Science and Technology, and Aalto University School of Chemical Engineering are acknowledged with gratitude.

I'd like to express my deepest and sincerest appreciation to my dear supervisor and advisor Prof. Simo-Pekka Hannula. You offered this valuable opportunity for me to pursue understandings in the fascinating world of high-entropy alloys, and provided me with guidance, encouragement, motivation, comforts, as well as full support throughout my whole studies in Finland. I especially appreciate your help, patience and understanding during the pandemic period. You set an example to me as a methodical, rigorous, energetic, and motivated scientist who always embraces innovations and challenges. It has been such a pleasant and rare experience to learn from one as knowledgeable and experienced as you. What I gained from the academic discipline you gave would benefit my future. My gratitude also goes to my supervisor Prof. Jari Koskinen, for taking responsibility of me after Prof. Simo-Pekka Hannula's retirement, and providing generous help and support. I'm grateful to my thesis advisor Dr. Yanling Ge, thank you for offering me numerous help with experiments, characterizations, and academic writing, especially giving me the learning chances from you, one of the best experts in the areas of electron microscopy and X-ray techniques.

I genuinely appreciate the time, contributions, and help of all co-authors: Dr. Yuriy Yagodzinsky, Dr. Oleg Heczko, Dr.-Ing. Volker Uhlenwinkel, Dr. Eryang Lu, Joonas Lehtonen, Dr. Lauri Kollo, Roy Björkstrand, Dr. Mika Salmi and all others. I sincerely thank Prof. Pasi Peura from Tampere University and Prof. Antti Salminen from University of Turku for examining this thesis critically and carefully. I'd like to acknowledge Dr. Lide Yao and Dr. Hua Jiang from Aalto University OtaNano Nanomicroscopy Center, for your guidance and help with electron microscopy.

All my colleagues and technical staff, I'm thankful for your great support, help, and friendliness. I wish to thank Dr. Shima Moosakhani, for being warmhearted, kind, thoughtful, supportive, and amazing. I always remember the first day when we met at the office, you held out the hand of friendship to me. I'd like to thank Dr. Frans Nilsén, for offering generous help whenever I

asked, and revising my first draft. I cherish your friendship with me. I want to thank Dr. Ilkka Penttinen, for your interesting topics and stories that I enjoy a lot. I'm grateful to Vasuki Durairaj for the great work on language check of this thesis. My thanks also go to Dr. Saima Ali, Dr. Henrika Granbohm, and Dr. Michal Trebala. I offer my special thanks to my dear friends, Dr. Fangxin Zou, Ya Zhu, and Yujiao Dong. I enjoy every meal we have together, they warm and comfort me especially during the pandemic, and I value your friendships with me.

One scene from a movie entitled *Measuring the World* encourages me through the academic journey. It is a dialogue when Humboldt asked Gauss what science was. Gauss's answer can be paraphrased as: if one acquires an understanding of stars before giving up, that, could be science. My special appreciations go to some good in this world, including but not limited to Li Yuchun, for being my role model and inspiring me since 2005; Nintendo, for creating those wonderful worlds; *Doctor Who*, for the imaginative stories about time and stars; and Arashi, for producing the brilliant music, concerts, and variety shows.

I dedicate my love with this humble work to meine geliebte Yumeng Xue. Thank you for materializing my childhood dreams, most importantly, being one of them that realized. You are the singularity of me. I treasure all the fantastic adventures you share with me, the countless times you accompany me, the songs you sing and play for me. I'm grateful for you being you. From your passion, enthusiasm, and astonishment, I see an eternal summertime in you that never fades, full of wonders, the smell of rain, and the chirping of cicadas. I can ask no more. Dedicating my master and doctoral thesis to you is a proud achievement of my life. Now I finally get to say this to you: trust me, I am a doctor.

Finally, I express my deepest and warmest gratitude to my parents, Qiuping and Mingshun, for your infinite and unconditional love. You have been, and shall always be my pride.

Espoo, 8 November 2021

Xuan Yang

# Contents

Acknowledgements.....	1
List of Abbreviations and Symbols .....	5
List of Publications .....	7
Author's Contribution.....	8
1. Introduction .....	9
2. State of the art.....	15
2.1 Categories of multicomponent alloys.....	15
2.2 Equiatomic CrFeNiMn alloy .....	17
2.2.1 Fabrication of multicomponent alloys via conventional methods .....	17
2.2.2 Fabrication of multicomponent alloys via rapid solidification techniques.....	19
2.2.3 Effects of hydrogen.....	23
2.3 AlCoCr <sub>0.75</sub> Cu <sub>0.5</sub> FeNi alloy .....	25
2.3.1 Conventional processing of AlCoCr <sub>0.75</sub> Cu <sub>0.5</sub> FeNi alloy .....	25
2.3.2 Application of rapid solidification techniques for AlCoCr <sub>0.75</sub> Cu <sub>0.5</sub> FeNi alloy processing .....	26
3. Experimental .....	31
3.1 Manufacturing Cr-Fe-Ni based multicomponent alloys .....	31
3.1.1 Gas atomization (GA).....	31
3.1.2 Laser powder bed fusion (LPBF) .....	31
3.1.3 Pulsed electric current sintering (PECS) .....	34
3.2 Characterization methods.....	34
3.2.1 Physical properties .....	34
3.2.2 Microstructure .....	34
3.2.3 Crystal structures and defects .....	35
3.2.4 Chemical composition.....	35
3.2.5 Hydrogen permeation and desorption .....	35
4. Results and discussion.....	37

4.1 Equiautomic CrFeNiMn alloy produced via SLM.....	37
4.1.1 SLM-induced hierarchical microstructure .....	37
4.1.2 Hydrogen induced effects .....	44
4.2 AlCoCr <sub>0.75</sub> Cu <sub>0.5</sub> FeNi alloy produced via SLM .....	49
4.2.1 SLM-produced microstructure .....	49
4.2.2 Tailoring magnetic properties by spinodal decomposition .	54
5. Conclusions .....	59
References .....	63

# List of Abbreviations and Symbols

## Abbreviations

AD	Archimedes density
AM	Additive manufacturing
ASS	Austenitic stainless steels
BCC	Body-centered cubic
BSE	Back-scattered electron
CCAs	Compositionally complex alloys
EBSD	Electron backscatter diffraction
EDS	Energy-dispersive X-ray spectrometry
FCC	Face-centered cubic
GA	Gas atomization
HE	Hydrogen embrittlement
HEAs	High-entropy alloys
LPBF	Laser powder bed fusion
MPEAs	Multi-principal element alloys
NPPs	Nuclear power plants
PAS	Positron annihilation spectroscopy
PECS	Pulsed electric current sintering
RD	Relative density
RS	Rapid solidification
SE	Secondary electron
SEM	Scanning electron microscopy
SLM	Selective laser melting
STEM	Scanning transmission electron microscopy

TDS	Thermal desorption spectroscopy
TEM	Transmission electron microscopy
XRD	X-ray diffraction
XRF	X-ray fluorescence spectroscopy

## Symbols

$\Delta G_{\text{mix}}$	Mixing Gibbs free energy, J
$\Delta H_{\text{mix}}$	Mixing enthalpy, kJ/mol
$\Delta S_{\text{conf}}$	Mixing configurational entropy, J/(mol·K)
$\Delta S_{\text{mix}}$	Mixing entropy, J/(mol·K)
at%	Atomic percent
$h$	Hatch spacing, $\mu\text{m}$
$H$	Field strength, T
HV	Vickers hardness
$M$	Magnetization, emu/g
$M_s$	Saturation magnetization, emu/g
$P$	Laser power, W
$R$	Universal gas constant, J/(mol·K)
$T$	Temperature, K
$t$	Layer thickness, $\mu\text{m}$
$T_c$	Curie temperature, K
$v$	Scanning speed, mm/s
VED	Volumetric energy density, J/mm <sup>3</sup>
vol. %	Volume percentage
wt%	Weight percent

# List of Publications

This doctoral dissertation consists of a summary of the following publications, which are referred to in the text by their respective roman numerals:

**I.** Xuan Yang, Yanling Ge, Joonas Lehtonen, Simo-Pekka Hannula. 2020. Hierarchical microstructure of laser powder bed fusion produced face-centered-cubic-structured equiatomic CrFeNiMn multicomponent alloy. *Materials*. 13 (20), 4498. DOI: <https://doi.org/10.3390/ma13204498>

**II.** Xuan Yang, Yuriy Yagodzinsky, Yanling Ge, Eryang Lu, Joonas Lehtonen, Lauri Kollo, Simo-Pekka Hannula. 2021. Hydrogen effects in equiatomic CrFeNiMn alloy fabricated by laser powder bed fusion. *Metals*. 11 (6), 872. DOI: <https://doi.org/10.3390/met11060872>

**III.** Xuan Yang, Oleg Heczko, Joonas Lehtonen, Roy Björkstrand, Mika Salmi, Volker Uhlenwinkel, Yanling Ge, Simo-Pekka Hannula. Microstructure and properties of additively manufactured AlCoCr<sub>0.75</sub>Cu<sub>0.5</sub>FeNi multicomponent alloy: controlling magnetic properties by laser powder bed fusion via spinodal decomposition. Submitted to *Materials & Design*.

# Author's Contribution

**Publication I:** Hierarchical microstructure of laser powder bed fusion produced face-centered-cubic-structured equiatomic CrFeNiMn multicomponent alloy

XY designed the experiments under the supervision and guidance of Prof. SPH and YG. The experiments and analysis were conducted by XY, together with YG. JL contributed to the fabrication of specimens by selective laser melting. XY was responsible for writing the manuscript. Prof. SPH and YG critically reviewed the results, discussion and conclusions, as well as writing.

**Publication II:** Hydrogen effects in equiatomic CrFeNiMn alloy fabricated by laser powder bed fusion

XY designed the experiments under the supervision and guidance of Prof. SPH and YG, and was responsible for main experiments, characterizations and analysis. YY performed the thermal desorption spectroscopy measurements, and contributed to the analysis of results and discussion. YG and XY were responsible for the characterization by transmission electron microscope. EL conducted the positron annihilation spectroscopy measurements, analyzed the results, and wrote the corresponding section of manuscript. JL and LK contributed to the fabrication of specimens by selective laser melting. XY wrote the manuscript along with EL, and the manuscript was revised based on comments from all co-authors. Prof. SPH and YG critically reviewed the results, discussion and conclusions, as well as writing.

**Publication III:** Microstructure and properties of additively manufactured AlCoCr<sub>0.75</sub>Cu<sub>0.5</sub>FeNi multicomponent alloy: controlling magnetic properties by laser powder bed fusion via spinodal decomposition

XY designed the experiments under the supervision and guidance of Prof. SPH and YG, and was responsible for main experiments, characterizations and analysis. OH performed the measurements of magnetic properties. JL carried out the electron backscatter diffraction analysis and processed the results. RB and MS were responsible for the fabrication of specimens by selective laser melting. VU contributed to the gas atomization of the powder. The manuscript was written by XY, and revised according to comments from all co-authors. Prof. SPH critically reviewed the results, discussion and conclusion, as well as writing.

# 1. Introduction

Great innovations in materials make indispensable contributions to the human society. Of all materials invented throughout the history, alloys play an essential role. An alloy is created by mixing one metal with other metallic or metalloid elements, to make more solid and durable tools. The very notion of adding tin into copper marks the beginning of the Bronze Age. Alloys are therefrom defined as the mixture of two or more elements, and at least one of the dominant compositions is a metal, known as the primary or base metal.

Based on this primary metal principle, different types of alloys and their manufacturing techniques have been developed over the past centuries. So far, approximately 30 alloy systems have been explored and applied to fulfill various practical applications [1]. They are classified according to their primary metal element, for instance, iron dominates the compositions of different iron alloys and steels. These conventional primary metal alloy systems have been properly established after generations of hard work, and few are left to be discovered. However, novel emerging technologies in recent years have created new demands on material properties that cannot be fully met by conventional alloys. In order to materialize such innovations and extraordinary properties, the traditional alloy design framework must be broken through.

One strategy is to introduce the concept of alloys consisting of multiple principal elements, namely the elements are equal in concentrations (generally equiautomic or equimolar). No longer restrained by the primary metal principle, this provides a large number of possibilities for permutations and combinations with multiple elements. However, this notion of multicomponent alloys was impracticable to materialize until the recent past decades due to two major reasons. Firstly, almost all of the research on traditional (one-primary-principle) alloys are on the basis of the phase diagrams, which indicate that complicated microstructure and equilibrium intermetallic compounds (IMs) or intermediate phases (IPs) are readily formed according to ternary phase diagrams [2]. Thus, it is reasonable to expect even more complex structures, instead of simple solid solutions, in the multiple principal element alloying systems, thereby leading to unfavorable brittle products. Furthermore, the complexity of multicomponent alloys' nature places greater demands on the controllability and efficiency of the metallurgy techniques.

Regardless of these difficulties, great potential and promising properties of the multicomponent alloys attract researchers' attention from all over the world. Gradually they manage to piece together a more complete picture of complex

alloy systems, and make contributions to both solid-state physics and materials science. Cantor et al. initiated the research on multicomponent alloys in 1981, and the results were published in 2004 [2]. In this research [3], they reported that the as-cast five component  $\text{Fe}_{20}\text{Cr}_{20}\text{Mn}_{20}\text{Ni}_{20}\text{Co}_{20}$  alloy exhibited a single-phase dendritic solid solution in form of face-centered cubic (FCC) crystal structure. Alloys consisting of six to nine components, made by adding transition metals including Ti, V, and Nb into the FeCrMnNiCo system, formed the majority primary dendritic FCC phase. Their findings proved that it is feasible to form much fewer phases than allowed by the Gibbs phase rule under equilibrium or non-equilibrium conditions, and especially, it is practical to achieve the single-phase solid solution in an alloy system containing multiple principal elements.

In the same year of 2004, Yeh et al. published two articles on multicomponent alloys [4,5]. This new alloy design approach was originally referred by them as high-entropy alloys (HEAs), as they found that mixing five or more elements with a content of each at 5-35 at% causes the increase of the configurational entropy in the system [5]. They evaluated the evolution of phase formation in as-cast  $\text{CuCoNiCrAl}_x\text{Fe}$  alloy (where  $0 \leq x \leq 3$ , in molar fraction), and found that a single FCC phase occurred when  $x = 0\text{--}0.5$ , a mixture of the body-centered cubic (BCC) and FCC phase was formed as  $x$  was higher than 0.8, finally a single BCC phase structure appeared when  $x$  exceeded 2.8 [5]. They also revealed the properties of  $\text{CuCoNiCrAl}_x\text{Fe}$  alloy [5]: the hardness of the alloy increased with the BCC content and achieved the highest value of 655 HV5 while  $x = 2.8$ . When the alloy was of single FCC structure, i.e.,  $x = 0.5$ , the compressive yield strength was retained up to the temperature of 800 °C. Other properties such as high-temperature wear resistance, oxidation resistance and compression strength were also found to be excellent [4,6]. These observations on the combinations of superior properties disclosed the promising potentials of HEAs for broad applications, including tools, molds, and mechanical parts. Therefrom, HEAs have attracted researchers' attention across the world, and they are considered to be the promising area to develop new alloys with superior microstructures and properties for the future.

To date, single phase solid solution in multicomponent alloys is normally identified as FCC, BCC, hexagonal close-packed (HCP), and orthorhombic phase structures [7]. As is well known, the solid solution type influences the properties significantly. An example of the mechanical properties was already given by Yeh et al. [5] in the research mentioned above, i.e., FCC-structured alloys exhibited great ductility with relatively low strength, while BCC-structured alloys possessed high strength with weak ductility. Kao et al. [8] determined the influence of crystal structure on the functional properties including the magnetic properties of  $\text{Al}_x\text{CrFeCoNi}$  ( $0 \leq x \leq 2$ ) alloys. Under the homogenized condition, single BCC phase structure was formed in the alloy when  $x \geq 1.25$ . At the evaluated temperatures of 5, 50, and 300 K, alloys with single BCC phase were ferromagnetic, and the saturation magnetization ( $M_s$ ) had greater values than those of the alloys with a single FCC phase as well as a mixing of FCC + BCC phase tested under the same conditions.

The type of solid solution depends on the chemical composition. For instance, Tung et al. [9] reported that in the AlCoCrCuFeNi alloy system, the Co, Cu and Ni elements promoted the FCC structure formation, while Al and Cr contributed to the BCC structure formation. Furthermore, the solid solution type is also related to the solidification process. In the research on the influence of solidification rates by Elmer et al. [10], it was observed that at low cooling rates during solidification, the austenite dominated the solidification structure in the stainless steels with low  $\text{Cr}_{\text{eq}}/\text{Ni}_{\text{eq}}$  ratio, while ferrite was the primary phase in the stainless steels with high  $\text{Cr}_{\text{eq}}/\text{Ni}_{\text{eq}}$  ratio. However, at high cooling rates, the solidification structure was single austenitic and single ferritic in alloys with low and high  $\text{Cr}_{\text{eq}}/\text{Ni}_{\text{eq}}$  ratio, respectively. Particularly, for one steel exhibiting a moderate  $\text{Cr}_{\text{eq}}/\text{Ni}_{\text{eq}}$  ratio of 1.60, the structure solidified primarily as ferrite at low cooling rates, and as metastable austenite at high cooling rates [10]. Therefore, both chemical compositions and fabrication methods should be taken into consideration when designing the new alloys.

Amongst the FCC-structured multicomponent alloys, the quinary CoCrFeNiMn alloy has been most extensively studied. However, this alloy is not universally appropriate to all kinds of application scenarios. Particularly considering the nuclear application, cobalt alloying element is unwanted. The isotopes of cobalt generated after neutron activation are the primary sources of radiation in the nuclear power plants (NPPs), which increases the risk of plant personnel, and results in the high disposal cost [11]. One of the approaches to avoid these disadvantages is to remove the cobalt alloying element, and produce the quaternary CrFeNiMn alloy. The non-equiautomic cobalt-free  $\text{FeNiMnCr}_{18}$  (in at%) alloy was successfully fabricated by Wu and Bei [12], which exhibited a single-phase FCC structure, and the tested mechanical properties including strength and ductility were similar to the quinary CoCrFeNiMn alloy. The microstructural evolution and mechanical properties of the  $\text{FeNiMnCr}_{18}$  alloy under ion irradiation, in the midrange doses of 0.03 to 10 displacements per atom (dpa) at temperatures up to 700 °C, were further investigated by Kumar et al. [13]. The phase structure was stable after irradiation up to 10 dpa at evaluated temperature. No voids were formed, which indicated the greater swelling resistance. Much less degree of radiation-induced solute segregation (RIS) was detected than that of Fe-Cr-Ni austenitic stainless steels. Their results proved that this alloy had an excellent radiation resistance which was comparable to the conventional austenitic stainless steels. It is therefore suggested that the quaternary CrFeNiMn alloy has promising potentials in the advanced nuclear applications.

One of the representative BCC-structured multicomponent alloys is the refractory TiZrHfNbTa based system [7]. The fabrication of this kind of alloy is difficult as it requires high temperature during the processing, and the alloys could be brittle. Consequently, they are of less interest to researchers when compared to the FCC-structured multicomponent alloys. On the other hand, the alternative lies in the multicomponent alloys with Al alloying elements, such as  $\text{CuCoNiCrAl}_x\text{Fe}$  and  $\text{Al}_x\text{CrFeCoNi}$ . It is mentioned above that single BCC phase structure was formed in  $\text{CuCoNiCrAl}_x\text{Fe}$  alloy when  $x > 2.8$  [5]. The FCC to BCC

transition usually occurs in these alloys when aluminum content is increased [5,14]. Particularly, Singh et al. [15] reported the investigations on the fabrication of equiatomic AlCoCrCuFeNi alloy employing splat quenching, one of the rapid solidification (RS) techniques. According to their observations, the splat-quenched alloy was of single BCC phase, rather than a dual phase structure of FCC and BCC phase in the as-cast alloy. This strongly indicates that RS would introduce a different microstructural formation in the multicomponent alloys, and it is feasible to achieve a single BCC structure in the AlCoCrCuFeNi based alloys.

Rapid solidification refers to a variety of techniques developed since the 1970s, which are widely employed in the industries nowadays for materials manufacturing and processing, such as powders, wires, foils and coatings. Such techniques include gas atomization, spray forming, splat quenching, melt spinning, etc. During these processes, the cooling rate generally exceeds  $10^4$  K/s. Due to the rapid extraction of thermal energy, undercooling of the melts occurs before the initiation of solidification [16]. As a result, the rapidly solidified materials possess homogenized chemical compositions and refined microstructures with enhanced mechanical and physical properties in comparison to materials fabricated conventionally [17].

Amid the numerous technologies involving RS, laser powder bed fusion (LPBF) is considered to be a compelling fabrication approaches, fast developing through the past two decades. It is one of the additive manufacturing (AM) methods that are popularly known as 3D printing. As the name suggests, LPBF describes the process that uses a laser beam to fuse the raw materials layer by layer speedily, and the raw materials used to build the bulk product are initially in the powder form. LPBF is also commonly known as selective laser melting (SLM) [18]. SLM is predominantly employed to build strong parts with complicated geometrical shapes rapidly. Excellent local controllability as well as RS during the processing, makes SLM an appropriate candidate to produce those materials which are difficult or even improbable to be produced by the traditional manufacturing methods, e.g., multicomponent alloys. Brif et al. [19] were the first to investigate the printability of a multicomponent alloy and then prepare it successfully using SLM. They reported that the selectively laser melted equiatomic FeCoCrNi alloy formed a single FCC crystal structure with homogeneous chemical distributions, and it exhibited a combination of high strength and ductility, which was as good as SLM-built stainless steels [19]. Their research unquestionably promotes the application of SLM in the fabrication of multicomponent alloys. A large number of researchers have started to explore the feasibility of selectively laser melted multicomponent alloys since then, which facilitates the knowledge and development of both SLM and multicomponent alloys. To achieve optimized productions with the SLM process, the starting raw materials, namely the metal powder, are preferably produced by inert gas atomization (GA), as it provides fine powder production with high density in spherical shape [20].

The objectives of this thesis involve the investigations of microstructure and properties of two Cr-Fe-Ni based multiple principal alloy systems, i.e., the

equiatomic CrFeNiMn alloy and the non-equiautomic AlCoCr<sub>0.75</sub>Cu<sub>0.5</sub>FeNi alloy. Neither of these two multicomponent alloys, successfully produced by SLM process from gas-atomized powder, has been reported previously, and consequently the knowledge concerning these remains scarcely few. Deeper and better understanding of these alloys is not only beneficial for the improvement and development of alloy design, but also forms a vital piece in the picture of advanced materials. The preparation of these two multicomponent alloys by SLM and their detailed characterization are thus considered to be the novelty of this thesis.

In this thesis, characterization of the microstructure includes the determination of porosity, crystal structures, chemical compositions, and rapidly solidified structures of the equiatomic CrFeNiMn alloy and the non-equiautomic AlCoCr<sub>0.75</sub>Cu<sub>0.5</sub>FeNi alloy produced by SLM process from the gas-atomized powder. The influence of input process parameters is studied, and the formation mechanisms of crystal structures are addressed. The properties such as hardness and magnetic behavior are determined, and the microstructural evolution induced changes in these properties are also studied. Furthermore, considering that the specific design purpose of CrFeNiMn alloy lies in advanced nuclear application, the influences of hydrogen on this alloy are also thoroughly investigated. Lattice defects in the specimens are identified by positron annihilation spectroscopy (PAS), hydrogen absorption under electrochemical hydrogen charging is determined by thermal desorption spectroscopy (TDS), and the microstructure changes of the hydrogen-charged specimen are studied by transmission electron microscopy (TEM). In addition, pulsed electric current sintering (PECS) is also used to process the same raw powder, as references for both multicomponent alloys, in order to compare the microstructure and properties with those obtained in SLM-built specimens. The concerning research questions are presented as follows:

1. What is the microstructure of equiatomic CrFeNiMn alloy produced by SLM, and how does the scanning speed affect the microstructure and then the hardness? (**Publication I**)
2. What are the influences of hydrogen in the equiatomic CrFeNiMn alloy produced by SLM? How are they different from that fabricated by PECS and conventional 316L stainless steels under the same experimental condition? (**Publication II**)
3. What is the microstructure of AlCoCr<sub>0.75</sub>Cu<sub>0.5</sub>FeNi alloy produced by SLM, how do the process parameters contribute to the formation of microstructure, and what are the effects of microstructure on the microhardness and magnetic properties? (**Publication III**)

The thesis is comprised of a summary and the appended three publications, which are referred to in the text by their corresponding Roman numerals. They all relate to the control of the microstructural features and properties of Cr-Fe-Ni based multicomponent alloys. Chapter 1 contains the introduction in general, to present the formation of research ideas on the basis of the existing research, and the objectives and research questions are described. Chapter 2 presents the detailed literature reviews of the current state-of-the-art research on the

## Introduction

equiatomic CrFeNiMn alloy and the non-equiautomic AlCoCr<sub>0.75</sub>Cu<sub>0.5</sub>FeNi alloy, as well as introduces the fabrication methods used in this research including SLM and PECS. Chapter 3 consists of the preparation details of the alloy specimens during the corresponding manufacturing processes, and a brief description of the characterization tools involved in analyzing the microstructure and properties of the specimens in this thesis. Chapter 4 presents the main findings in the publications along with discussions. Finally, Chapter 5 constitutes the conclusions, and provides suggestions for research in the future.

## 2. State of the art

### 2.1 Categories of multicomponent alloys

The alloying design strategy of mixing multiple principal elements in high concentrations has been widely accepted. Initially these alloys were named as HEAs by Yeh et al. [5], corresponding to the higher mixing entropy in the alloy system that forms single-phase solid solutions with five or more elements, in comparison to the traditional alloys with only one or two major elements. Herein, entropy is used as a guideline to define and design high-entropy alloys as well as related materials. When combining elements to produce an alloy, Gibbs free energy ( $G$ ) is the key factor to control phase formation, when kinetic factors are not considered. It is known that a system will try to minimize its  $G$  under isothermal and isobaric conditions. Adopting this assumption in the multicomponent systems which form the solid solutions, the mixing Gibbs free energy  $\Delta G_{mix}$  is expressed as follows:

$$\Delta G_{mix} = \Delta H_{mix} - T\Delta S_{mix} \quad (1)$$

where  $\Delta H_{mix}$  is the mixing enthalpy,  $\Delta S_{mix}$  is the mixing entropy, and  $T$  refers to the temperature at which the elements are mixed. The mixing enthalpy in a multicomponent system can be determined by [21]:

$$\Delta H_{mix} = \sum_{i=1, j \neq i}^n 4\Delta H_{AB}^{mix} x_i x_j \quad (2)$$

where  $\Delta H_{AB}^{mix}$  is the mixing enthalpy of a binary equiatomic AB alloy. While the mixing enthalpy in the alloy system usually has several origins, only the configurational entropy is considered here to simplify the calculation, as it makes the most dominant contributions. According to the Boltzmann equation, the mixing entropy of a regular solution state containing  $n$  elements is given by [21]:

$$\Delta S_{conf} = -R \sum_{i=1}^n c_i (\ln c_i) \quad (3)$$

where  $R$  (8.31 J/(mol·K)) is gas constant. The mixing entropy would be the maximum when the atomic ratio of alloys is equal, and  $\Delta S_{mix}^{max}$  is:

$$\Delta S_{conf}^{max} = R \ln(n) \quad (4)$$

As depicted in Fig. 2.1, the term “high entropy” represents the mixing entropy  $\Delta S_{conf} \geq 1.5R$  alloy systems [7]. Furthermore, the traditional (low entropy) alloys correspond to alloys with mixing entropy  $\Delta S_{conf} \leq R$ , and the range between the low and high mixing entropy comprises the medium entropy. In this thesis, the

mixing entropy of the equiatomic CrFeNiMn alloy is calculated to be  $\Delta S_{\text{conf}} = 11.53 \text{ J}/(\text{mol}\cdot\text{K})$ , which falls within the scope of medium-entropy alloys; and the mixing entropy of the non-equiatomic AlCoCr<sub>0.75</sub>Cu<sub>0.5</sub>FeNi alloy is  $\Delta S_{\text{conf}} = 14.68 \text{ J}/(\text{mol}\cdot\text{K})$ , which is categorized as a high-entropy alloy.

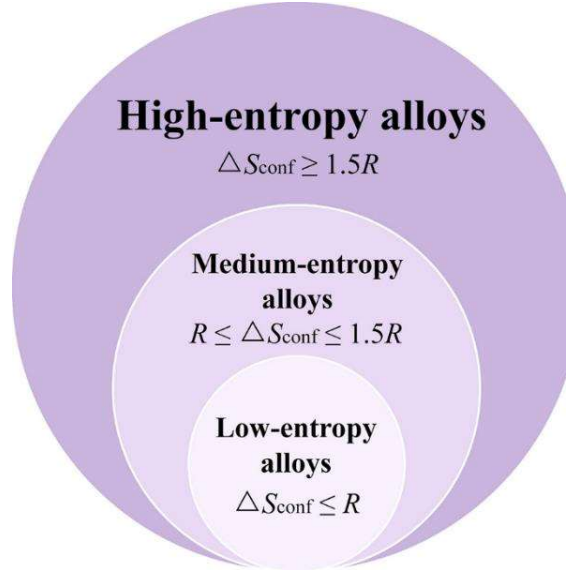


**Fig. 2.1.** Categorization of multicomponent alloys based on the mixing entropy in system (modified from [2]).

“High entropy” is introduced as a descriptor for the prediction of phase formation, i.e., in an alloy with five or more elements, the mixing entropy is high and single-phase solid solution forms. However, a majority of HEAs produced in the early years consists of multiple phases [7]. Furthermore, for many alloys with less than five major elements, such as equiatomic CrFeNiMn alloy, stable single-phase solid solutions can be reached. For instance, a CrFeCoNi alloy forms a single-phase FCC structure with fully recrystallized microstructures [22]. The phase stabilization in such alloys is likely dependent on enthalpy instead of entropy [7]. Otto et al. [23] evaluated the role of configurational entropy in the single-phase solid solution stability. They replaced each element individually in the CoCrFeMnNi alloy, with another element possessing the same crystal structure at room temperature and similar size or electronegativity, for example, Co was replaced by Ti. The configurational entropy was supposed to remain the same, as well as the single-phase solid solution formation. Yet, they found that configurational entropy in the equiatomic quinary alloys altered significantly. Those which were expected to have a single phase turned out to have multiphase, and their configurational entropies were low [23]. Based on the results, they proposed that only those alloys that achieve a true solid solution can be considered as high-entropy alloys, and those which form several phases and possess lower entropies are suggested to be referred as multicomponent alloys [23]. The alloys in this thesis are thus introduced as multicomponent alloys.

Since entropy is insufficient to act as a predictor for this categorization of newly developed alloys, several alternative names of this alloy design strategy

are proposed along with the research ongoing, in order to categorize those recently discovered alloys that do not fit into the high-entropy category. In the overview article by Miracle and Senkov [24], they introduce the concepts of multi-principal element alloys (MPEAs) and compositionally complex alloys (CCAs). These concepts are schematically presented in Fig. 2.2. HEAs are used in the scenario where the configurational entropy is high and the aim is to create a single-phase solid solution. MPEAs, which are identical to multicomponent alloys, include all alloys with concentrated, multiple principal elements such as ternary and quaternary alloys, but do not fit the definitions of HEAs. CCAs specifically correspond to those with multiple phase structures.

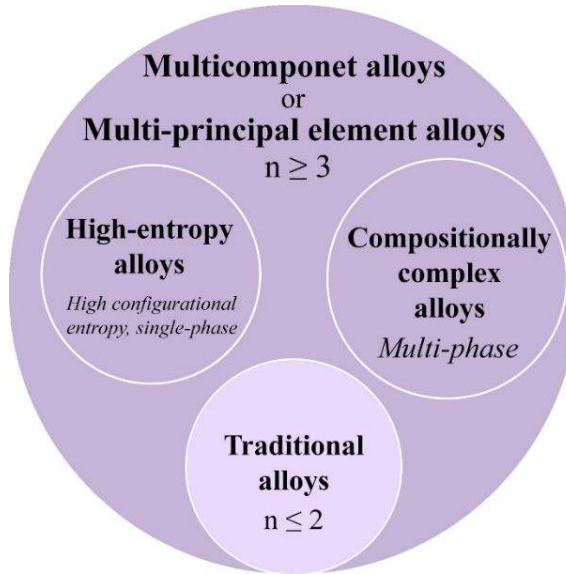


**Fig. 2.2.** Categorization of alloys according to the number of major elements (n) in the system (summarized from [24]).

## 2.2 Equiautomic CrFeNiMn alloy

### 2.2.1 Fabrication of multicomponent alloys via conventional methods

As mentioned in Chapter 1, the cobalt element is not favorable in some specific applications such as NPPs, and accordingly, it is removed from the quinary CoCrFeNiMn alloy, and the quaternary CrFeNiMn alloy is created. Wu and Bei [12] first reported the successful fabrication of the non-equiautomic FeNiMnCr<sub>18</sub> (in at%) alloy by arc melting. The results presented by Wu and Bei [12] demonstrated that this alloy exhibits great mechanical properties in comparison to CoCrFeNiMn alloy. Yield strength was around 450 MPa at room temperature, and remained higher than that of CoCrFeNiMn alloy up to 473 K. At the temperature of 673 K, its yield strength is slightly lower than that of CoCrFeNiMn alloy, and the value for both alloys is similar (~150 MPa) as the test temperature is increased to 873 K [12]. Then the further research by Kumar et al. [13] concerning the mechanical behaviors and microstructural changes of this alloy after the Ni ion irradiation, at temperatures up to 700 °C and radiation doses in the range from 0.03 to 10 dpa, revealed its better phase stability as well

as similar radiation resistance compared to conventional stainless steel. The promising mechanical behavior and radiation resistance therefore attracts research interests towards this Co-free non-equiautomic FeNiMnCr<sub>18</sub> alloy, and many research articles on it have followed. Li et al. [25] evaluated the mechanical properties of neutron-irradiated FeNiMnCr<sub>18</sub> alloy at 60 °C under the radiation doses from 0.1 to 1 dpa. After irradiation, no phase transformation was detected, and the increasing trend of yield strength and Vickers hardness was similar to 316 stainless steel. Their observations indicated that this alloy had identical behavior when comparing to conventional austenitic stainless steels. Apart from the mechanical properties, the magnetic properties of FeNiMnCr<sub>18</sub> alloy were studied by the first principle study as well [26,27].

Besides the FeNiMnCr<sub>18</sub> alloy, other Co-free CrFeNiMn alloys with different chemical compositions have also been developed. Stepanov et al. [28] prepared a series of Fe<sub>40</sub>Mn<sub>28</sub>Ni<sub>32-x</sub>Cr<sub>x</sub> ( $x = 4, 12, 18$  and  $24$ , in at%) alloys by vacuum arc-melting. The samples exhibited single phase FCC structure at  $x = 4, 12$  and  $18$ , but at  $x = 24$  the phase structure constituted of a mixture of FCC phase and tetragonal  $\sigma$  phase, with the estimated volume fractions of 55% and 45%, respectively. Yield strength of the single phase alloy was found to rise from 210 to 310 MPa, and the elongation to fracture was decreased from 71% to 54%, as the content of Cr increased from 4 to 18 at% [28]. Nutor et al. [29] prepared Fe<sub>50</sub>Mn<sub>27</sub>Ni<sub>10</sub>Cr<sub>13</sub> (in at%) alloy by arc melting, and investigated its mechanical properties and corrosion resistance. In the as-cast, cold-rolled, and annealed samples, single FCC phase structure was formed, and the measured yield strength and elongation were 90 MPa and 40%, 575 MPa and 5%, and 205 MPa and 42%, respectively. The alloy presented a comparable corrosion resistance behavior in NaOH solution as well as H<sub>2</sub>SO<sub>4</sub> solution, and a better corrosion resistance against HCl solution as well as NaCl solution, in comparison to the reference 304 stainless steel. These results suggest that the Fe<sub>50</sub>Mn<sub>27</sub>Ni<sub>10</sub>Cr<sub>13</sub> alloy have a combination of good mechanical performances as well as corrosion resistance. Zhang et al. [30] determined the effect of Cr content in the Cr<sub>x</sub>MnFeNi ( $x = 0.8\text{--}1.5$ , in molar fraction) alloy fabricated by induction melting. A single FCC structure was formed when  $x = 0.8$ , after that a mixture of BCC and FCC crystal structure was detected, and the mass fraction of BCC phase gradually increased from 1.2% to 23.1% as the Cr content grew from  $x = 1$  to 1.5. A higher solid solution strengthening in comparison to conventional FCC alloys was observed. This was ascribed to the large lattice friction stress introduced by the serious lattice distortion [30]. In addition, Dong et al. [31] fabricated a Co-free CrFeNiMn alloy by vacuum induction melting with a chemical composition of 17.9 wt% Cr, 27.5 wt% Fe, 28.1 wt% Ni and 26.5 wt% Mn. They studied the environmental degradation behavior i.e., stress corrosion cracking (SCC) and oxidation in high-temperature hydrogenated water, which is a simulated environment of the primary coolant in pressurized water reactor (PWR). X-ray diffraction pattern only disclosed the FCC phase structure, while the Cr-enriched  $\sigma$  phase participants were also observed in the secondary electron (SE) image. The constant extension rate tensile test, performed under a pressure of 15 MPa at a temperature of 320 °C, gave a yield strength of 136 MPa.

Furthermore, a great number of intergranular cracking was observed after the test, which suggested that this alloy was susceptible to the initiation of SCC [31]. They also found that Cr resulted in the formation of a protective oxide layer around the grain boundaries, which is beneficial for resisting the penetrative intergranular oxidation, although the oxidation layer was pretty porous resulting from the Mn distribution [31].

In the research discussed above, one apparent feature in common is that the alloys are all close to equiatomic, yet still non-equiatomic. The preparation of equiatomic CrFeNiMn alloy with single-phase solid solution has scarcely been reported before. It has been found that a higher chromium concentration in the alloy provides a stronger solid solution strengthening [28] as well as a good corrosion resistance [29]. However, in order to achieve the single FCC phase structure, the chromium content in the alloy needs to be kept below 18 wt% [12]. This is because chromium would act as a BCC phase stabilizer. Furthermore, according to the research on the phase equilibrium between austenite and ferrite in the Cr-Fe-Ni-Mn system by Raghavan [32], as the chromium content exceeded 18 wt%, the manganese turned out to destabilize the FCC structure rather than stabilizing it as when the chromium content was lower. In exception, it is to be noted that Bian et al. [33] produced the  $\text{Fe}_{40}\text{Mn}_{20}\text{Cr}_{20}\text{Ni}_{20}$  (in at%) alloy composing of a single FCC phase structure. They suggested that the alloy was formed under non-equilibrium solidification, and the small fraction of BCC was avoided by the rapid cooling following the casting [33]. However, with the rising content of Cr in the alloy system, more BCC phase would form [30], which could be difficult to avoid. Thus it appears unlikely to produce equiatomic CrFeNiMn alloy with single-phase solid solution using traditional methods.

### **2.2.2 Fabrication of multicomponent alloys via rapid solidification techniques**

Additive manufacturing (AM) involving the rapid solidification process was first employed by Brif et al. [19] in the fabrication of multicomponent alloys, as a means to fulfill the requirement of high controllability during the process resulting from the complex compositions in the system with multiple principal elements. They explored the feasibility of producing equiatomic FeCoCrNi alloy utilizing selective laser melting. The SLM-produced sample retained the single FCC phase structure. Furthermore, it exhibited a yield strength of 600 MPa, which was more than 3 times higher than that of arc-melting and as-casted samples. The mechanical performances of SLM-built equiatomic FeCoCrNi alloy were comparable to both conventional and SLM-fabricated stainless steels [19]. This combination of great strength and good ductility was attributed to the microstructure introduced by the rapid solidification during the SLM process, including the homogeneous chemical distributions and refined grain size [19]. The successful preparation of multicomponent alloys by SLM and the promising results attract researchers to devote more efforts towards the investigations of selectively laser melted multicomponent alloys.

As illustrated in Fig. 2.3, a laser beam is utilized to fully melt the raw powder in the SLM process, and as the laser beam moves according to the programmed

scanning pattern, one layer is built. Then the fabrication piston is moved down, new powder is supplied into the building platform from powder delivery platform by the roller, and another layer is built on the top of previous layer. Finally, the sample is built layer by layer into a bulk with any pre-designed shape.

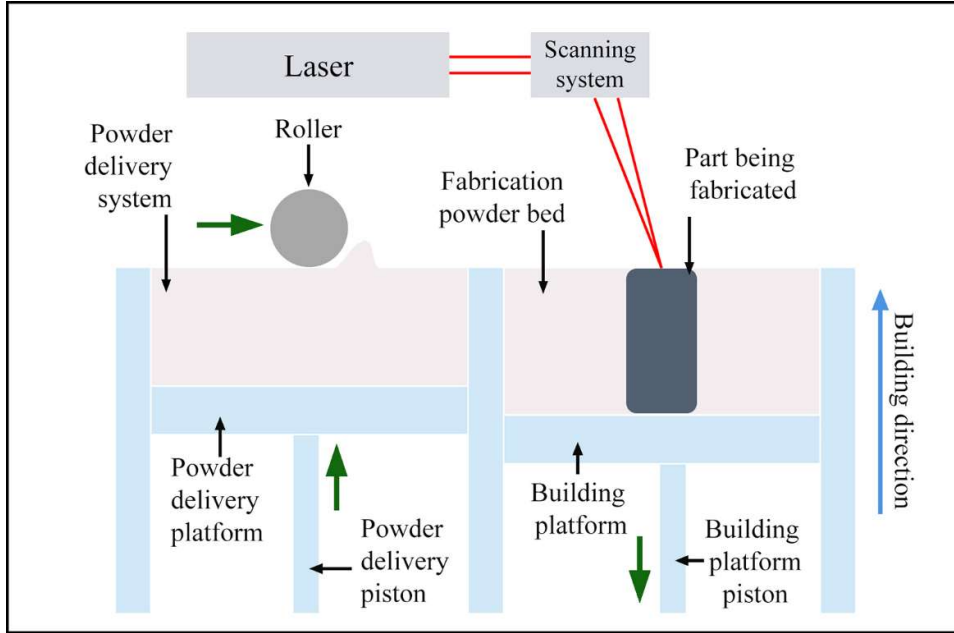


**Fig. 2.3.** A schematic representation of selective laser melting process (modified from [34]).

There are several parameters involved in the process, i.e., laser power  $P$  (W), scanning speed  $v$  (mm/s), hatch spacing  $h$  ( $\mu\text{m}$ ) and layer thickness  $t$  ( $\mu\text{m}$ ). Hatch spacing refers to the distance between the center of two consecutive and adjacent scans. The comprehensive influence of these process factors can be determined by the volumetric energy density (VED), which is given as follows:

$$VED = \frac{P}{v \cdot h \cdot t} \quad (5)$$

According to previous studies on the SLM process [35–39], it is essential to optimize the process parameters in order to achieve a final product with a high density, and good physical and chemical properties, as the properties are dependent on the rapidly solidified microstructure. Representative morphologies of typical structures on the xy-plane are presented in Fig. 2.4. The xy-plane corresponds to the layer which is built perpendicular to building direction. These structures include the island scanning pattern, comprising of melt pool tracks (Fig. 2.4a), magnified melt pool boundaries and cellular structure (Fig. 2.4b), and high magnification equiaxed cells and a large density of dislocations concentrated both in the interior and at the boundaries of the cells (Figs. 2.4c and d).

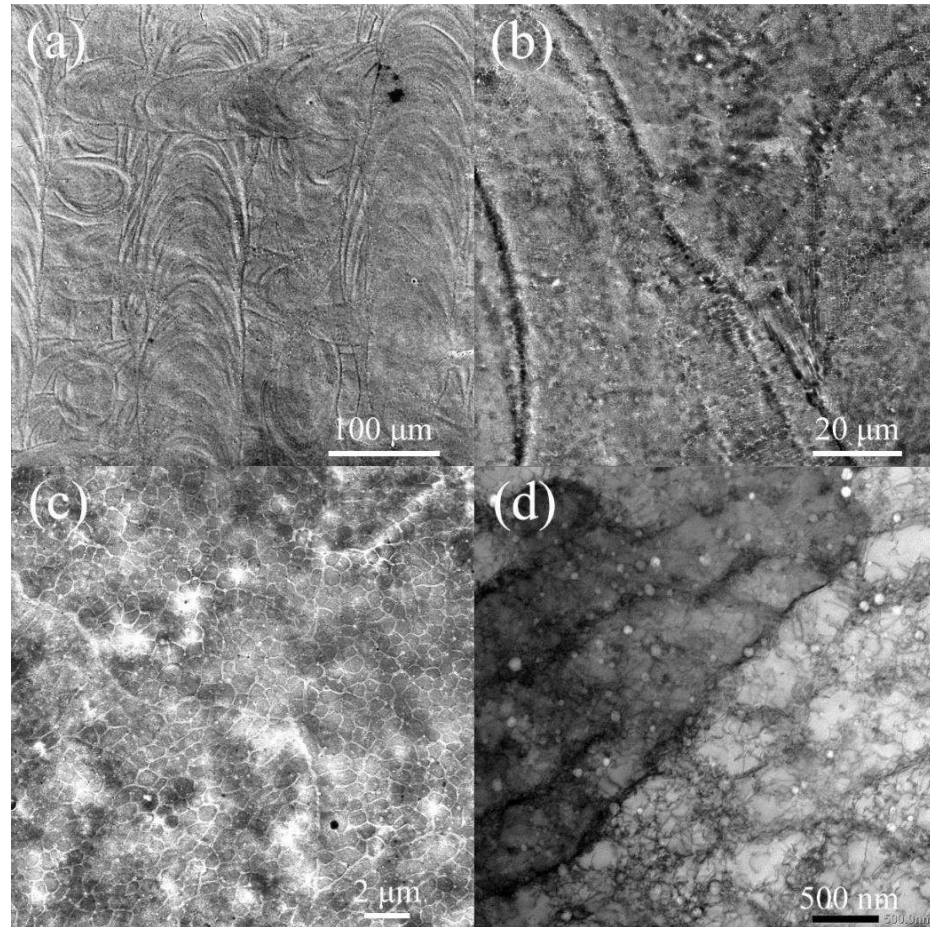


**Fig. 2.4.** Representative observations on xy-plane of electrochemically etched SLM-produced alloy. SE images of (a) island scanning patterns composing of melt pool tracks, (b) melt pool boundaries and cellular structure, and (c) magnified cells. (d) Scanning transmission electron microscope (STEM) image of cellular structure in correlation with a high density of dislocations (images by Xuan Yang).

Li et al. [40] were the first to report the fabrication of the classical CoCrFeNiMn alloy through SLM. It was noted that the density of as-built samples gradually rose as the input VED grew, up to a value of  $74 \text{ J/mm}^3$ , where the highest relative density of 98.2% was reached. After that, the density was decreased due to the formation of keyhole [40]. XRD curves depicted that the starting gas-atomized powder as well as all as-built samples exhibited plain FCC crystal structure. The lattice parameter was found to reduce with the increase of VED, which was ascribed to the severer Mn loss under the higher VED. Furthermore, the segregation of Mn at the melt pool boundaries was detected. The highest ultimate tensile value of 601 MPa was obtained as the VED rose to  $123 \text{ J/mm}^3$ , owing to the rapidly solidified structure including ultrafine grains and  $\sigma$  phase precipitates [40]. Zhu et al. [41] systematically disclosed the hierarchical microstructure of laser melted CoCrFeNiMn alloy, i.e., columnar grains, melt pools, cellular structures, and dislocations. The as-built sample showed a great combined strength and ductility when comparing to the as-cast and as-recrystallized samples. Particularly, the rapidly solidified microstructure was found to be beneficial to the improved mechanical properties [41–44].

In general, the strength of metallic alloys is known to comprise of the following factors [45]: i) Peierl's stress (lattice friction), ii) solid solution strengthening (both by substitutional and interstitial atoms), iii) precipitation hardening, iv) grain boundary strengthening (including twins), and v) dislocation strengthening (strain hardening) comprising of dislocation structures such as dislocation cells and boundaries. Depending on the alloy, a number if not all of these factors influence the strength of the alloy. However, there is no comprehensive treatment on these factors for multicomponent alloys and there is a wide variety of opinions on how the summation of the individual factors should be made. Therefore, various attempts to rationalize the strength of multicomponent alloys have been made.

After the observation of the cellular structures (i.e., cells or sub grains), researchers have tried to rationalize the relationship between cell size and yield strength according to Hall-Petch relation [41,43]. Wang et al. [43] proposed in a research concerning the 316L stainless steel produced by SLM, that the strength and hardening depended not only on the cellular structures but were also associated with the microstructure induced by rapid solidification, including the elemental segregation, high angle grain boundaries (HAGBs), low angle grain boundaries (LAGBs), and high density dislocations. Moreover, Zhu et al. [41] stated that the improved strength in SLM-built specimens was mainly attributed to dislocation strengthening, friction stress, and grain boundary strengthening, and it was not simply scaled with cell size on the basis of Hall-Petch relation. Anyhow, it has been demonstrated that SLM is capable of inducing a refined and hierarchical microstructure which benefits the physical, chemical, and mechanical properties of the alloy. Therefore, it would be interesting to explore the microstructure of equiatomic CrFeNiMn alloy produced by SLM process.

Considering the starting materials for SLM process, an appropriate selection is the metallic powder obtained by gas atomization, because it possesses smooth spherical morphology and fine-scale uniform microstructure. The fabrication and microstructure of the equiatomic CrFeNiMn powder manufactured by gas atomization have been reported in the preliminary work conducted by our research group (Advanced and Functional Materials group at Department of Chemistry and Materials Science, Aalto University) [46]. It was found that the powder exhibited a dominant FCC phase in addition to a small fraction of BCC phase. The estimated weight percentages of BCC phase structure were found to be decreasing with the increasing particle class size (i.e., the size range of particles), that is, in powders with particle class sizes of < 20  $\mu\text{m}$ , 20-45  $\mu\text{m}$ , 45-90  $\mu\text{m}$ , and 90-150  $\mu\text{m}$ , the BCC phase was ~5.5 wt%, ~1.8 wt%, ~1.2 wt% and ~0.4 wt%, respectively. The relatively larger amount of BCC phase in the powder having a smaller particle class size was proposed to relate to the higher cooling rate experienced by the smaller powder particles. Furthermore, the smaller powder particles also exhibited a finer grain size. Consequently, the highest nano hardness of  $4.25 \pm 0.73$  GPa was obtained by the powder exhibiting a particle class size < 20  $\mu\text{m}$ , due to the larger amount of BCC phase and finer grains. In addition, the difference determined in the phase structure was also

represented by the  $M_s$ , where the FCC exhibited the paramagnetic behavior, while BCC structure contributed to ferromagnetic. Thus the smaller powder particle containing more BCC phase showed improved soft magnetic behavior [46]. This powder was also processed by pulsed electric current sintering (PECS), also commonly known as spark plasma sintering (SPS), in order to compare the final microstructure with the SLM process. In PECS, large pulsed direct electric current and uniaxial pressure are employed to rapidly consolidate the powder [47]. In this process, the powder is first loaded into a graphite die coated with a graphite paper and stacked between the punches. Then a pulsed direct current is employed to generate spark discharges between the space of the particles, thus creating a local high temperature, and a uniaxial force is also applied during the process, finally leading to the consolidation of powder in a few minutes [48]. It has many advantages including high efficiency, reproducibility, and reliability, as well as high controllability of the process.

### **2.2.3 Effects of hydrogen**

As a potential candidate in the advanced nuclear application, it is crucial to evaluate the performances of equiatomic CrFeNiMn alloy in that target application scenario. One of the serious environmental degradations in NPPs could be resulted from hydrogen embrittlement (HE), which occurs when hydrogen atoms diffuse into the metal and transport within it. HE results in the formation of cracks, as well as loss of strength and ductility, eventually leading to failure of the construction materials [49]. In the NPPs, hydrogen usually originates from the corrosion of construction components, or is added into the primary coolant for the purpose of scavenging oxygen and minimizing the corrosion [50]. During the diffusion and transportation of hydrogen into the bulk, hydrogen atoms may be trapped in the sites such as lattice defects and interfaces. As the amount of hydrogen accumulated locally at a potential crack site surpasses the critical threshold, hydrogen induced cracking could initiate. The quantification of hydrogen concentration in a metal represents the hydrogen uptake ability, which is crucial to determine the susceptibility for cracking and hydrogen embrittlement. Thermal desorption spectroscopy (TDS) has been proved to be one of the most effective tools for the measurement of absorbed hydrogen content, and analysis of hydrogen trapped in the lattice and defects of the alloys [51–53]. In addition, positron annihilation spectroscopy (PAS) is a hypersensitive and non-destructive technique to characterize the open volume defects in materials, including the vacancies and voids. The combination of both characterization tools is effective to disclose the hydrogen uptake ability of additively manufactured equiatomic CrFeNiMn alloy.

The influences of hydrogen on multicomponent alloys have been explored only in recent years. Almost all conventional metallic materials investigated in the past suffer from HE, however, it is likely that the multicomponent alloys behave differently when encountering hydrogen. This has been shown in a series of research conducted by Luo and his colleagues [54–56]. The microstructural evolution and mechanical performance of CoCrFeMnNi alloy manufactured by casting, rolling and annealing were first determined [54] by performing tensile

tests under *in-situ* electrochemical hydrogen charging. The results indicated that strength and ductility of CoCrFeMnNi alloy were enhanced after hydrogen was introduced into the alloy, under several different electrochemical charging conditions. This behavior was attributed to the presence of nano twinning. The stacking fault energy of CoCrFeMnNi alloy was  $\sim 19 \text{ mJ}\cdot\text{m}^2$  [57], and it was found to be further decreased by hydrogen, accordingly leading to the formation of high density of nano twins. Those nano twins contributed to strain-hardening, accordingly promoting the improvement of strength and ductility [54]. The formation of nanotwins in the hydrogen charged CoCrFeMnNi alloy was further confirmed under cryogenic condition [55]. Following electrochemical charging and cryogenic deformation, a gradient nano-twin structure was observed below the top surface to the depth of over  $35 \mu\text{m}$ , as well as coarse twins at the sample center. Hydrogen induced nanoscale and coarse twins resulted in the increase of strain hardening, which overcame the hydrogen induced embrittlement. Based on the observations, they proposed the self-accommodation mechanism of CoCrFeMnNi alloy, i.e., the more hydrogen atoms were concentrated locally, the lower the stacking fault energy became, thereby a higher formation rate of twins was achieved, and improved mechanical properties were reached. Zhao et al. [58] reported that no new phase was detected after electrochemical hydrogen charging. Furthermore, they determined that under the same gaseous charging condition, the CoCrFeMnNi alloy exhibited merely  $\sim 5\%$  loss of ductility, which was much lesser than those of conventional stainless steels ( $\sim 61\%$  in 304 and  $\sim 27\%$  in 316L), even though it absorbed a higher amount of hydrogen, which indicated the excellent resistance of CoCrFeMnNi alloy against the gaseous hydrogen embrittlement [59]. However, Nygren et al. [60] found that, on the contrary, the alloy experienced a decline of ductility after gaseous hydrogen charging, in conjunction with an alteration from ductile microvoid coalescence failure to intergranular fracture. Thus, they concluded that CoCrFeMnNi alloy was susceptible to HE.

The majority of existing research concerning the hydrogen effects on additively manufactured alloys has been conducted on the SLM-produced stainless steels, while the contributions of microstructure induced by rapid solidification are under debate [61–64]. Lee et al. [61] found similar  $\alpha'$  martensite transformation in both SLM-built and conventional 304L steel, thus leading to the conclusion that the solidification cells do not affect the phase stability and hydrogen trapping behavior. In addition, Park et al. [62] disclosed that the SLM-processed 316L steel absorbed less hydrogen and possessed similar hydrogen solubility and an apparent hydrogen diffusivity lowered by the solidification cellular structure, when compared to the conventional 316L steel. It was stated that dislocations, as well as segregated elements concentrated in the walls of cellular structures, were relatively insensitive to hydrogen, and did not make contributions to hydrogen uptake ability as significantly as the cell interiors did [62]. In contrast, Lin et al. [63] claimed higher hydrogen diffusion rate owing to the cellular structure in SLM-built 316L steel. Under a low diffusion, most of the hydrogen atoms tended to diffuse in the cell walls; as the diffusion rate increased to a certain degree, the hydrogen would spread and

diffuse into the interiors of cells, which led to defects formation in them. These observations suggested that the cell walls were acting as rapid transportation channels for hydrogen. Furthermore, Kong et al. [64] barely noticed the martensite transformation in the SLM 316L steel after electrochemical hydrogen charging, while they observed that the wrought 316L steel experienced the phase transformation under the same charging condition. This improved phase stability was ascribed to the fine cellular structure in conjunction with the high density of dislocations [64]. The research on hydrogen uptake in the selectively laser melted multicomponent alloys remains few. It is known that the high solubility of hydrogen in CoCrFeMnNi alloy is benefited from the relatively high content of Cr and Mn, lattice distortion, as well as nanoscale heterogeneity in the multicomponent alloys, compared to the conventional stainless steels [59,65]. Kim et al. [65] suggested that the resistance of SLM-processed CoCrFeMnNi alloy against HE can be ascribed to the high solubility of hydrogen, and the promotion of twin formation during deformation. Particularly, the mechanism of hydrogen transportation in SLM-processed microstructure proposed by Lin et al. [63], i.e., the boundaries of cells and grains are behaving as rapid transportation paths for hydrogen, was adapted by Fu et al. [66] in the research concerning the SLM-built CoCrFeMnNi alloy. They suggested that hydrogen atoms would concentrate in cellular structures, as well as in other trapping sites including grain boundaries, dislocations and micro voids, then further increase the local residual strain and external tensile load, resulting in the initiation of hydrogen-induced cracking. They removed most of the dislocations in the SLM-built sample by annealing, and the tensile tests under in-situ electrochemical hydrogen charging showed that the strength was slightly decreased due to the loss of dislocations, yet the ductility was noticeably increased. The initiation and propagation of hydrogen-induced cracking were decelerated, and accordingly the resistance to hydrogen was enhanced.

## 2.3 AlCoCr<sub>0.75</sub>Cu<sub>0.5</sub>FeNi alloy

### 2.3.1 Conventional processing of AlCoCr<sub>0.75</sub>Cu<sub>0.5</sub>FeNi alloy

The research concerning the AlCoCrCuFeNi based multicomponent alloys has been ongoing since Yeh et al. published the article in which the notion of HEAs was first explicated back in 2004 [5], and progressively it has developed into one of the most investigated multicomponent alloy systems [67,68,9,69,70,15,71]. In fact, it is the Al<sub>x</sub>CoCrCuFeNi (in which  $0 \leq x \leq 3$ , in molar fraction) alloy that was explored by Yeh et al. as a representative to demonstrate that it is practical for the multiple principal alloy system to form a simple solid solution [5]. Moreover, they reported that the solid solution structure was adjustable by altering the content of aluminum in Al<sub>x</sub>CoCrCuFeNi alloy [5,67], as described in Chapter 1. In addition, adding aluminum alloying element into multicomponent alloys also results in many advantages including a lower density, improved strength, superior corrosion resistance and oxidation resistance [72–75]. Tung et al. [9] explored the elemental effects on the phase

formation of the AlCoCrCuFeNi based alloy, by reducing the content of each element to 0.5 (in molar ratio, other elements were equimolar) in the system individually. All samples exhibited a simple solid solution structure, and similar to the findings in the research on steels, Ni, Co, and Cu favored the FCC formation, and Al and Cr promoted the BCC formation [9]. Compared to FCC phase, BCC phase possessed higher strength, owing to the lattice structure and solution hardening [9]. Kuznetsov et al. [70] determined the tensile properties of equiatomic AlCoCrCuFeNi alloy, and revealed its excellent yield strength of 790 MPa at room temperature for the as-cast condition, and that of 1040 MPa for the hot forged condition. Zhang et al. [69] examined the influence of microstructure on mechanical and magnetic properties of equiatomic AlCoCrCuFeNi alloy. The as-cast sample contained both FCC and BCC phase structure, and the as-annealed sample was composed of two types of FCC phase and BCC phase. As a result of possessing more BCC structure, the as-cast sample revealed a large hardness value of 515.5 HV<sub>5</sub> and improved compressive strength of 1.82 GPa [69]. The as-cast sample also showed a soft magnetic behavior in correlation with a higher  $M_s$  of 38.18 emu/g (at room temperature) [69], comparable to those of soft ferrite materials [76]. Singh et al. [77] further noticed that the magnetic behavior of equiatomic AlCoCrCuFeNi alloy was in correlation with the spinodal decomposition. The  $M_s$  values of the as-cast, splat-quenched, and aged samples were determined to be 46, 44 and 48 emu/g at 14T and 300 K, respectively. The difference in ferromagnetism was rationalized by the decomposition of Cr-Fe-Co enriched phase into the ferromagnetic Fe-Co enriched phase and antiferromagnetic Cr enriched phase. The degree of decomposition increased in the order of splat-quenched, as-cast, and aged, thus resulting in the largest  $M_s$  for the aged sample [77]. Additionally, the AlCoCrCuFeNi based system has also been developed with the addition of other elements including Ti, V, Si, and B. These alloys show great mechanical properties, wear resistance and oxidation resistance [6,78–80]. The investigations on these various alloy systems would unquestionably promote the development of multicomponent alloys.

### **2.3.2 Application of rapid solidification techniques for AlCoCr<sub>0.75</sub>Cu<sub>0.5</sub>FeNi alloy processing**

As described in the previous section, the AlCoCrCuFeNi based alloys prepared by traditional processes including casting, rolling, forging and annealing usually contain a dual phase structure of FCC and BCC phase, and in order to reach a single-phase solid solution, the content of alloying elements needs to be adjusted. For instance, the phase structure of AlCoCrCuFeNi, Al<sub>0.5</sub>CoCrCuFeNi and AlCoCrCu<sub>0.5</sub>FeNi (in molar ratio) alloys are determined as FCC+BCC, FCC and BCC, respectively [9]. On the other hand, former research works have presented the feasibility of achieving a single BCC crystal structure in the equiatomic AlCoCrCuFeNi alloy through splat quenching [15] and ultrarapid quenching [71], i.e., the treatments involving a rapid cooling rate. Therefore, among various techniques, SLM exhibits high controllability, and the potential

to introduce a single solid solution as well as a refined and homogeneous microstructure, without the need for extra treatments.

Although the AlCoCrCuFeNi based alloys are one of the most extensively studied systems among the multicomponent alloys, their fabrications by SLM remain scarce, especially when comparing to CoCrFeNiMn alloy. Some research has been conducted on the additively manufactured multicomponent alloys composed of similar chemical compositions, including the AlCrCuFeNi [81], AlCoCuFeNi [82], AlCrCoFeNi [83] and AlCoCrFeMnNi [84]. Novak et al. [85] prepared the  $\text{Al}_{0.5}\text{CoCrCuFeNi}$  alloy by laser melting, and detected the segregation of copper into the interdendrite, similar to conventionally produced AlCoCrCuFeNi alloys, as mentioned in Section 2.3.1. Wang et al. [86] studied the influences of VED on the microstructure and mechanical performances of selective laser melted equimolar AlCoCrCuFeNi alloy. It was disclosed that the formation of cracks was difficult to avoid in the as-built samples. All samples consisted of a mixing of FCC and BCC phase structure, and the volume fraction of FCC phase increased gradually along with the increase of input VED, which was ascribed to the higher temperature achieved under the larger VED. A high cracking sensitivity was observed, which was also found in other Al-containing alloys [87]. In this case, it was resulting from the presence of HAGBs, segregation of copper, and the different strengths between the dual phase structure. Despite the cracks, the as-printed sample revealed the highest Vickers hardness of 710.4 HV, and this was benefited from the refined grains and a large density of dislocations introduced by the rapid solidification process [86]. More investigations need to be performed in order to obtain a better and deeper knowledge, and provide a perspective on the additively manufactured AlCoCrCuFeNi based alloys.

It is described in the former section that in the AlCoCrCuFeNi based alloy, the copper element tends to segregate into the interdendritic phase. The mixing enthalpy of copper with other elements in the system is relatively positively high, and consequently it is not favored in the dendrite where other elements are concentrated [9]. By reducing the content of Cu, the elemental segregation, as well as the volume fraction of interdendrite, were significantly decreased, and the as-cast sample exhibited a microstructure like recrystallized grain structure [9]. In addition, lower copper concentration contributes to a decreased density as well as cost [85]. Srivastava et al. [88] reported the manufacturing of  $\text{AlCoCr}_{0.75}\text{Cu}_{0.5}\text{FeNi}$  alloy by spray forming, in which relatively rapid solidification occurs. The microstructure was compared among the spray-formed, as-cast, spray-formed-heat-treated alloys, and the overspray powder obtained as the by-product of the spray forming process. It was noticed that all overspray powders exhibited a single BCC phase structure, while the as-cast alloy consisted of multiple phases including BCC, FCC (referred as FCC1) and  $\sigma$  phase, and the spray formed alloy was composed of two types of FCC phases (referred as FCC1 and FCC2) and BCC phase, as well as some unidentified phases. After heat treatment, only FCC1 and BCC phase were observed in the spray-formed-heat-treated sample. The segregation of copper at the interfaces between BCC and FCC phase was detected in both spray-formed and as-cast

samples, and the former showed less segregation than the latter, owing to the fast cooling induced supersaturation of solid solution phases. They concluded that cooling rate contributed significantly to the formation of phase structure, i.e., as the first formed phase during cooling was BCC phase, a faster cooling rate would suppress the formation of FCC phase, and result in a larger amount of BCC phase up until the formation of single BCC phase. Their results were in accordance with the spinodal decomposition stated by former researchers [15,89,90].

The phase evolution in correlation to spinodal decomposition during the solidification of AlCoCrCuFeNi alloy was first established by Singh et al. [15], based on the investigations conducted on the splat-quenched sample (cooling rate was in range of  $10^6\text{-}10^7$  K/s, similar to the SLM process [91,92]) and as-cast sample (which experienced a cooling rate of  $10\text{-}20$  K/s). Then Zhang et al. [89] characterized the melt-spun sample as well as the spray-cast sample, which were produced under a cooling rate of  $10^6\text{-}10^7$  K/s and  $10^2\text{-}10^3$  K/s, respectively. At last, Peter et al. [90] provided the knowledge between the high and low cooling rates, by characterizing the microstructure of overspray AlCoCr<sub>0.75</sub>Cu<sub>0.5</sub>FeNi powder, which experienced an intermediate cooling rate of  $10^3\text{-}10^4$  K/s. Based on these studies, the phase evolution during solidification is summarized and schematically illustrated in Fig. 2.5. At the highest cooling rate, a polycrystalline single BCC phase structure is formed; as the cooling rate decreases to an intermediate level, the segregation of grain boundary from the melt initiates first, then the spinodal decomposition of grain interior occurs, and separates into BCC A<sub>2</sub> and BCC B<sub>2</sub> phases at the nanoscale, followed by a formation of Cu precipitates during the nucleation process in the B<sub>2</sub> phase; with the further decline of cooling rate, the formation of dendrites and interdendrites is detected, and the dendrites consist of A<sub>2</sub> and B<sub>2</sub> structure, while interdendrites indicate Cu-rich precipitates. Finally, at relatively low cooling rates typical of as-cast and annealed conditions, an equilibrium state is reached, and the dendrites as well as interdendrites are observed, i.e., interdendrites containing Cu enriched L<sub>1</sub><sub>2</sub> structure (FCC1), and dendrites composed of the rhombohedral Cu enriched L<sub>1</sub><sub>2</sub> structured precipitates (FCC2), plate-like Cu enriched precipitates (B<sub>2</sub>), Al-Ni enriched plates (B<sub>2</sub>), and Cr-Fe enriched interplates (BCC) [15,89,90].

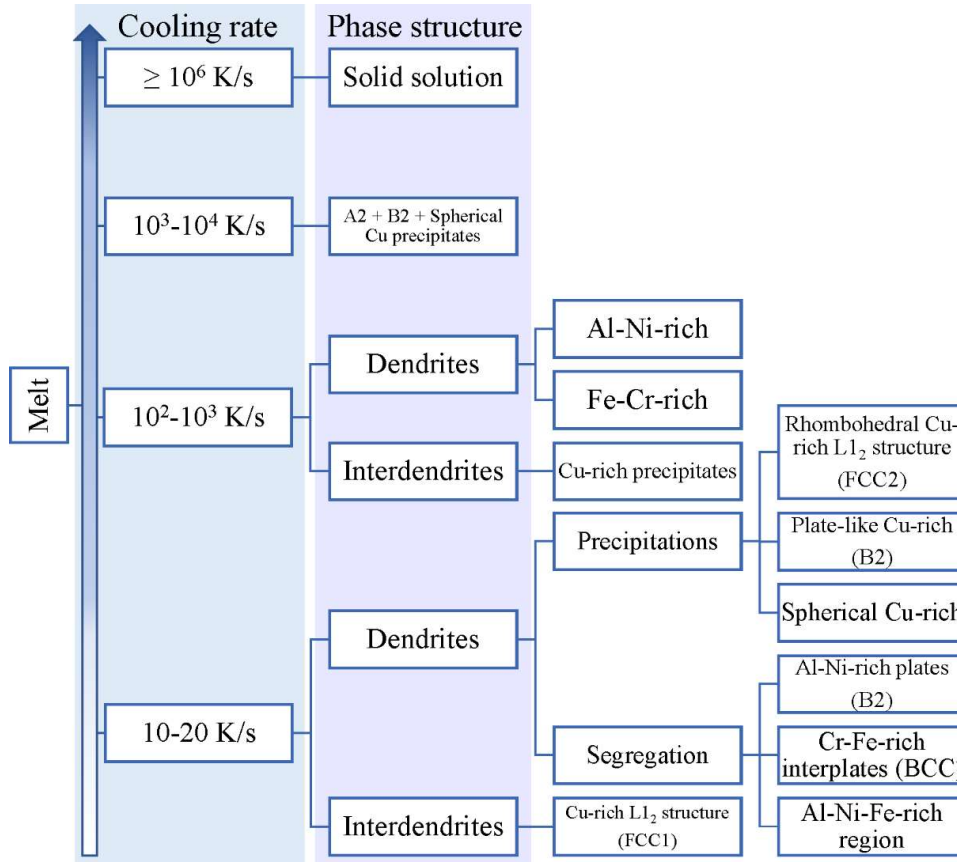


**Fig. 2.5.** Schematic illustrations of phase formation during solidification of AlCoCrCuFeNi alloy (summarized and modified from [15,89,90]).

The microstructural evolution results in changes of the properties. Since the cooling rate governs the spinodal decomposition in AlCoCrCuFeNi based alloys, it is feasible to achieve the desired properties by controlling the cooling rate. This can be easily conducted in SLM, by adjusting the scanning speed. Magnetic behavior is one of the attractive functional properties to start with, considering that it is relatively more sensitive to structural changes than other properties [93]. Recently, the improvement of magnetic properties through spinodal decomposition in  $\text{Fe}_{15}\text{Co}_{15}\text{Ni}_{20}\text{Mn}_{20}\text{Cu}_{30}$  HEA has been carried out by Rao et al. [94]. Therefore, it is rational to expect that the variation of cooling rate would introduce a different degree of spinodal decomposition, and lead to the enhancement in the magnetic behavior. In turn, the magnetic measurements represent the phase structure in the samples. The combination of high level of controllability in SLM with the spinodal decomposition provides a promising strategy to conduct the design and fabrication of new magnetic materials.



## 3. Experimental

This chapter briefly introduces the methodology of processing and characterization of the multicomponent alloys i.e., equiatomic CrFeNiMn alloy (studied in **Publications I** and **II**) and AlCoCr<sub>0.75</sub>Cu<sub>0.5</sub>FeNi alloy (studied in **Publication III**). More detailed information can be found in the attached publications.

### 3.1 Manufacturing Cr-Fe-Ni based multicomponent alloys

#### 3.1.1 Gas atomization (GA)

The powder manufactured by gas atomization has been selected as the starting material in the SLM process. The atomization was performed at the Department of Production Engineering, Foundation Institute of Materials Science (IWT), University of Bremen, Germany.

For the equiatomic CrFeNiMn powder, the raw metal materials (Cr, Fe and Ni: > 99.6 wt%; Mn 98.9 wt%) were melted at a temperature of 1920 K and then atomized with argon gas at a mass flow rate of 252 kg/h, and pressure of 1.2 MPa. Anti-satellite was also employed to increase the powder flowability. More information is given in ref. [46].

The AlCoCr<sub>0.75</sub>Cu<sub>0.5</sub>FeNi powder used was a byproduct of spray forming process. During the process, the raw materials was melted at a temperature of 1773 K and then atomized employing nitrogen gas with a gas flow rate of 850 kg/h and a mass flow rate of 430 kg/h under a pressure of 4 bars. Those overspray powder particles which were not involved in the sprayed deposit were collected and sieved. The detailed description can be found in [88,90].

#### 3.1.2 Laser powder bed fusion (LPBF)

Specimens investigated in **Publications I** and **II** were selectively laser melted from the equiatomic CrFeNiMn powder, with the particle class size in the range of 20-45 µm. SLM process was carried out at the Department of Industrial and Mechanical Engineering, Tallinn University of Technology, Estonia. A Realizer SLM-50 machine equipped with a laser source, producing a maximum power of 120 W and a laser beam with a diameter of 50 µm, was utilized. Specimens with dimensions of 20 × 20 × 3 mm<sup>3</sup> were additively manufactured in a protective argon atmosphere, and the oxygen level in

chamber was kept below 0.2%. The process parameters were optimized on the basis of research conducted by Liu et al. [95]. In the preliminary experiments, series of samples were produced using different process parameters. Then two samples possessing an acceptable density were selected from the set of samples. The corresponding process parameters are given in Table 3.1. During the building process,  $P$  of 70 W, a layer thickness ( $t$ ) of 25  $\mu\text{m}$ , and a hatch spacing ( $h$ ) of 98  $\mu\text{m}$  were employed. The  $v$  adopted in the fabrication of two samples i.e., SLM-1 and SLM-2, was 200 and 150 mm/s, corresponding to energy density ( $E$ ) or volumetric energy density (VED) of 142.86 and 190.48 J/mm<sup>3</sup>, respectively. The VED was calculated according to equation (5) given in Section 2.2.2. The island scanning strategy with islands of  $5 \times 5$  mm<sup>2</sup> in size was employed, and a rotation angle of 90° was applied between each deposited layer, as delineated in Fig. 3.1. This strategy ensures that each layer is re-melted to achieve a high density [96], and it also reduces residual stresses [97].

**Table 3.1.** Process parameters of SLM-built equiautomic CrFeNiMn specimens.

Sample	Power (W)	Scanning speed (mm/s)	VED (J/mm <sup>3</sup> )
SLM-1	70	200	142.86
SLM-2	70	150	190.48

Island scanning strategy

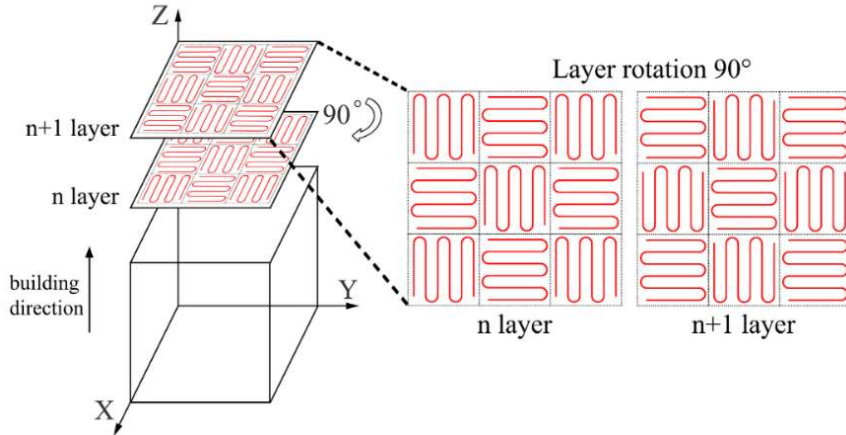


**Fig. 3.1.** Schematic illustrations of island scanning strategy.

The AlCoCr<sub>0.75</sub>Cu<sub>0.5</sub>FeNi powder used was with a particle class size between 20 and 63  $\mu\text{m}$ . Fabrication of specimens was carried out at the Department of Mechanical Engineering, Aalto University School of Engineering, Finland. For the printing, EOS M290 machine equipped with a 400 W Ytterbium fiber laser source possessing a focus diameter of ~100  $\mu\text{m}$  was used. Printing was conducted under a protective argon atmosphere, and content of oxygen in chamber was maintained below 0.1%. The laser beam was moving according to the meander scanning strategy during the process, and a rotation angle of 67° was adopted between each layer, as illustrated in Fig. 3.2a. The meander strategy is chosen to achieve a more homogeneous microstructure [98], while maintaining a relatively low porosity, as the microstructure affects the targeted functional properties. The  $h$  of 90  $\mu\text{m}$  and  $t$  of 20  $\mu\text{m}$  were applied. The as-built

samples had dimensions of  $15 \times 15 \times 3.5$  mm<sup>3</sup> as shown in Fig. 3.2b. The process parameters were selected according to the research carried out by Wang et al. [86], in which they produced the equimolar AlCoCrCuFeNi alloy by LPBF employing  $P$  in the range from 160 to 400 W,  $v$  in the range from 400 to 1600 mm/s, and obtained the highest density when applying the VED of 52.08 J/mm<sup>3</sup>. The parameters are listed in Table 3.2. One set of the samples, i.e., samples #1-3, were produced under the same  $P$  of 200 W, while increasing  $v$  from 1200 to 2000 mm/s. This was done to determine the influence of  $v$  during the SLM process. Another set of samples, namely #3-5, was fabricated under the same VED of 55.56 J/mm<sup>3</sup>, while the combinations of  $P$  and  $v$  were altered, to investigate the effects of these factors.

**Table 3.2.** Process parameters of the SLM-built AlCoCr<sub>0.75</sub>Cu<sub>0.5</sub>FeNi specimens.

Sample #	Power (W)	Scanning speed (mm/s)	VED (J/mm <sup>3</sup> )
1	200	1200	92.59
2	200	1500	74.07
3	200	2000	55.56
4	180	1800	55.56
5	160	1600	55.56

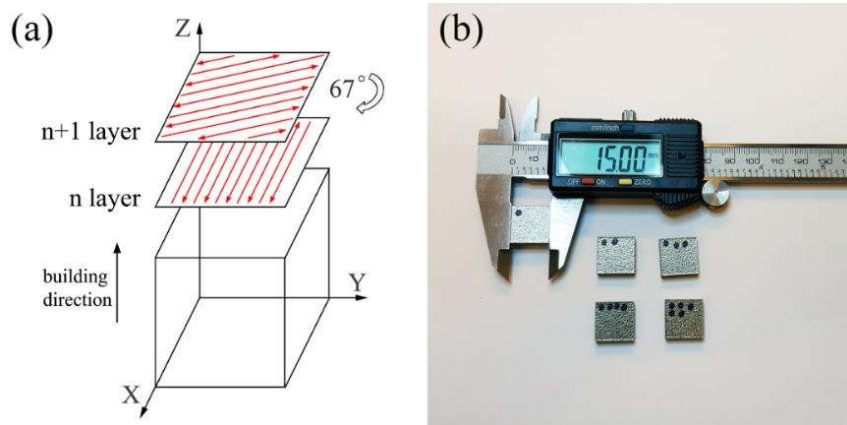


**Fig. 3.2.** (a) A schematic illustration of meander scanning strategy and (b) as-printed samples.

For microscopy characterization, the samples were cut into small slices or pieces using a Buehler IsoMet low-speed cutting machine. The samples on the xy-plane of SLM-1 and SLM-2 equiatomic CrFeNiMn alloys were prepared by first grinding with SiC paper to P1200, and electrochemically etching with a voltage of 18 V at -23 °C. TEM discs studied were punched from the slices on the xy-plane ground to a thickness of 100 µm, followed by a polishing process carried out in a Struers TenuPol-5 twin jet polisher, employing a 13 vol% HNO<sub>3</sub>-ethanol solution under a voltage of 20.5 V at a temperature of -23 °C. The samples on the xy- and xz-plane of SLM-built AlCoCr<sub>0.75</sub>Cu<sub>0.5</sub>FeNi specimens #1-5 were initially pre-ground with SiC paper to P1200. The mechanically polished samples were polished with Al<sub>2</sub>O<sub>3</sub> suspension down to a particle diameter of 0.3 µm, followed by a final polishing for 18 h by a Buehler VibroMet 2 vibratory polisher, applying Al<sub>2</sub>O<sub>3</sub> suspension having a particle diameter of 0.05 µm. Electrochemical polishing of the samples was carried out in a 13 vol%

$\text{HNO}_3$ -ethanol solution, at -23 °C under a voltage of 8 V. SEM samples were cleaned with ethanol in an ultrasonic cleaner and dried with hot air. TEM discs were loaded into a Gatan Solarus 950 plasma cleaner for 10 min before each characterization.

### 3.1.3 Pulsed electric current sintering (PECS)

In order to compare the microstructure introduced by different techniques, pulsed electric current sintering (PECS) was employed to process the corresponding set of gas-atomized powders. The sintering process of both multicomponent alloys was carried out in a FCT HP D 25-2 unit, in Ar atmosphere. The powder having a particle class size below 200  $\mu\text{m}$  was loaded into a cylindrical graphite die having an internal diameter of 20 mm. For the equiatomic CrFeNiMn alloy, the powder was consolidated at a temperature of 1110 °C under a pressure of 35 MPa, and held for one minute. The AlCoCr<sub>0.75</sub>Cu<sub>0.5</sub>FeNi alloy samples were sintered at a temperature of 1000 °C under a pressure of 35 MPa, and held for 5 minutes. The heating and cooling rates were adjusted to 100 °C/min. The sintered samples were thus in the annealed state. After sintering, the samples were ground with SiC paper from P120 down to P2500, and polished to a mirror finish consecutively with alumina ( $\text{Al}_2\text{O}_3$ ) suspensions having particle sizes of 5, 1, and 0.05  $\mu\text{m}$ . Finally, the samples were cleaned with ethanol in an ultrasonic cleaner and dried with hot air.

## 3.2 Characterization methods

### 3.2.1 Physical properties

The relative density and porosity of the samples were measured using Archimedes' method, and the Vickers hardness was evaluated by a low-force Innovatest Nexus 4303 tester according to standard ISO 6507-1:2018 [99]. Measurements were performed at a force of 4.903 N and a dwell time of 10 s, and nine to ten points were examined for each sample.

A Quantum Design physical property measurement system (PPMS) equipped with a vibrating sample magnetometer (VSM) was utilized to examine the magnetic properties. The evaluations of saturation magnetization from magnetization loops were carried out in field strengths of up to 9 T, at temperatures of both 10 and 300 K. Temperature dependence of the magnetization curves was recorded in both fields of 0.01 T (low) and 2 T (saturation), at temperature from 10 to 800 K, to determine the ferromagnetic Curie point of each specimen. The measurements of magnetic coercivity from magnetization loops were performed by a VSM PAR with an electromagnet.

### 3.2.2 Microstructure

Microstructural studies were conducted using a JEOL JIB-4700F focused-ion-beam scanning electron microscope (FIB-SEM), and a TESCAN Mira3 field

emission gun scanning electron microscope (FEG-SEM). A JEOL JEM-2800 transmission electron microscope (TEM) was employed for studying the finer details, in which both TEM and scanning transmission electron microscope (STEM) images were obtained.

### 3.2.3 Crystal structures and defects

The crystal structures were identified by X-ray diffraction (XRD). The phase constitutions were examined by a PANalytical X'Pert PRO MPD diffractometer applying Co-K $\alpha$  radiation. The device was operated at an acceleration voltage of 40 kV and a filament emission current of 40 mA, employing a step size of 0.0131° and a count time of 119.85 s per step. Analysis of the patterns was carried out by X'Pert HighScore Plus software (version 4.8), including the phase identification and phase quantification by the Rietveld refinement method.

The lattice defects were determined by positron annihilation spectroscopy (PAS), studying the Doppler broadening of positron annihilation radiation spectrum, which was conducted by a variable energy slow positron beam. The applied positron energy was in the range of 0.5–25 keV. Preparation of the samples included grinding with SiC paper to P1200, and then electrochemically polishing with a 13 vol. % HNO<sub>3</sub>-ethanol solution at a temperature of -23 °C, in order to remove the damaged layer on subsurface.

Grain size was determined utilizing electron backscatter diffraction (EBSD), performed by a Zeiss Ultra 55 field-emission scanning electron microscope (FE-SEM) equipped with an Oxford Instruments Nordlys F<sup>+</sup> EBSD camera.

### 3.2.4 Chemical composition

Chemical composition was measured using either energy-dispersive X-ray spectroscopy (EDX or EDS) or X-ray fluorescence spectroscopy (XRF). The elemental EDS analysis was performed either by a JEOL JED-2300 Analysis Station Plus EDX system installed on a JEOL JIB-4700F FIB-SEM, or on JEOL JEM-2800 TEM, or by Thermo Fisher Scientific EDX detector installed on the TESCAN Mira 3 FEG-SEM. In order to obtain the average chemical composition, forty measurements distributed at different areas were conducted for each sample.

A PANalytical Axios<sup>MAX</sup> 3 kW wavelength-dispersive X-ray fluorescence spectrometer (WDXRF) was adopted for the determination of chemical composition of selected samples.

### 3.2.5 Hydrogen permeation and desorption

Influence of hydrogen in SLM-built CrFeNiMn alloy was evaluated in **Publication II**. Before hydrogen charging, the samples having dimensions of 10.5 × 3.0 × (0.3–0.4) mm<sup>3</sup> were ground with SiC paper down to P2500, followed by the polishing process to a mirror finish utilizing Al<sub>2</sub>O<sub>3</sub> suspensions with particle sizes in the order of 5, 1, and 0.05 μm. Electrochemical hydrogen permeation was carried out at a temperature of 40 °C for 25 h, under -950

## Experimental

$\text{mV}_{\text{Hg}/\text{Hg}_2\text{SO}_4}$  in 1 N  $\text{H}_2\text{SO}_4$  solution with the addition of 20 mg/L of thiourea ( $\text{CH}_4\text{N}_2\text{S}$ ) acting as a hydrogen poison. Hydrogen desorption was studied by thermal desorption spectroscopy (TDS). The measurements were conducted by means of heating the hydrogen charged sample from room temperature up to 850 °C with a heating rate of 6 K/min, while recording the spectra of effusion of diffusible hydrogen, through examining the partial pressure of hydrogen in the ultra-high vacuum chamber. The vacuum in the chamber was maintained at better than  $5 \times 10^{-9}$  mbar. Hydrogen was cathodically introduced also to the 3 mm TEM discs using the same electrochemical hydrogen permeation solution as above. Current density of 50 mA/cm<sup>2</sup> was applied for 30 min at ambient temperature.

## 4. Results and discussion

This chapter elucidates the main findings in this thesis concerning the research objectives and questions presented in Chapter 1. The first section (Section 4.1) contains the characterizations on the microstructure and the analysis of hydrogen effects in the SLM-built equiatomic CrFeNiMn alloy. The second section (Section 4.2) focuses on the microstructural evolution and resulting changes in properties of  $\text{AlCoCr}_{0.75}\text{Cu}_{0.5}\text{FeNi}$  alloy produced by SLM. More detailed results and discussions are presented in **Publications I-III**.

### 4.1 Equiatomic CrFeNiMn alloy produced via SLM

#### 4.1.1 SLM-induced hierarchical microstructure

The relative density and chemical composition of two SLM-produced CrFeNiMn specimens are summarized in Table 4.1, along with corresponding process parameters. It is found that the decrease of scanning speed from 200 to 150 mm/s causes little effect to the relative density of each specimen, i.e., both as-built specimens exhibit a relative density of ~98%. The porosity may emerge from the unmelted particles, gas pores or cracks [100]. On the other hand, the chemical composition alters noticeably depending on the applied parameters. The bulk specimens experience a loss of Mn element compared to the raw powder, and Mn content reduces more noticeably in SLM-2. This results from the lower scanning speed applied in SLM-2, corresponding to a higher VED. When the high energy laser beam melts the powder, the local temperature increases significantly, which leads to the vaporization of volatile elements such as Mn. Similar loss of Mn element has also been observed in other selective laser melted Mn-containing alloys [101]. Since a higher VED is employed in SLM-2 than in SLM-1, more loss of Mn is detected in SLM-2, while the Mn content in SLM-1 remains similar to the starting powder.

**Table 4.1.** Process parameters in relation to the relative density and chemical composition (in at%) of SLM-produced CrFeNiMn specimens, along with the chemical composition of the starting powder. Most of the measurement errors of chemical composition are below 0.3 at% for all elements except Mn element, which varies more noticeably due to segregation.

Specimen	Process parameters		Relative Density	Chemical composition (at%)			
	VED/ J·mm <sup>3</sup>	Scanning speed /mm·s <sup>-1</sup>		Cr	Mn	Fe	Ni
Powder	-	-	-	26.9	25.1	24.5	23.5

SLM-1	142.86	200	$98.0\% \pm 0.1\%$	25.5	24.9	24.8	24.8
SLM-2	190.48	150	$97.9\% \pm 0.2\%$	25.8	24.0	25.3	24.9

The small BCC 100 peak indicates the coexistence of BCC and FCC phase in the starting powder, as displayed in Fig. 4.1. The amount of BCC phase is higher in the powder with a larger particle class size [46]. After SLM process, the higher relative intensity of 220 peak detected in SLM-built specimens suggests that the preferred crystallographic texture is formed during the process. More importantly, single FCC phase structure is found in both as-built specimens. In a former research by Raghavan [32], it has been demonstrated that in order to obtain a single FCC structure formation in Cr-Fe-Ni-Mn alloying system, the Cr content has to be lower than 18 wt%. The formation of a single FCC phase structure in SLM-built CrFeNiMn specimens is attributed to the favored FCC formation by RS process during SLM (**Publication I**).

In solidification, the smallest liquid droplet is most unlikely to possess a nucleant, because the probability for a droplet to contain potent heterogeneous nucleants is proportional to its volume. When the melt solidifies, small droplets have the tendency to achieve the largest supercooling prior to the initiation of nucleation, in comparison to large droplets. The small powder particles that solidify from small droplets are thereby expected to experience a higher degree of supercooling than the large particles. In combination with the observation that a higher amount of BCC is found in the powder with a larger particle class size, it indicates that the formation of BCC structure is preferred when the degree of supercooling is higher (**Publication I**). Once a small fraction of BCC phase is formed, it serves as a site for heterogeneous nucleation of thermodynamically stable FCC structure. FCC phase forms next to BCC phase, where Ni and Mn are enriched (**Publication I**). These results are in agreement with Kelly et al. [102], who rationalized the formation of BCC phase under large supercooling by the isolation of heterogeneous nucleants. FCC formation is favored in the large powder particles and SLM-built specimens, as in both scenarios, heterogeneous nucleants are readily available (**Publication I**). The heterogeneous nucleation induced epitaxial growth in SLM process is also represented by the high intensity of 220 peaks in Fig. 4.1.

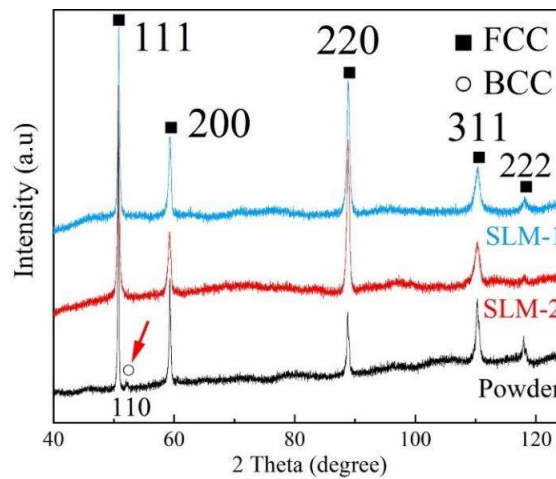


**Fig. 4.1.** XRD curves of raw powder and SLM-built CrFeNiMn specimens [**Publication I**].

Defect formation in SLM- and PECS-produced specimens was studied by positron annihilation experiments. In order to investigate the vacancy information, Doppler broadening spectrum of positron annihilation was employed.  $S$  parameter refers to the fraction of annihilation with low-momentum valence electron, and  $W$  parameter represents the fraction of annihilation with high-momentum core electron [103].  $S$  parameter is delineated as a function of incident positron energy ( $E$ ) in Fig. 4.2a, along with the mean penetration depth indicating the average detection depth of mono-energy slow positrons [104]. The  $S$  parameter, with a value of 0.408 displayed by a dashed line, is evaluated using a pure nickel sample annealed at a temperature of 1173 K, which represents the reference value in a defect-free solid. As can be seen, the values of  $S$  parameter measured in all SLM- and PECS-produced specimens are larger than that in pure Ni, revealing the existence of vacancies in these specimens.  $S$  parameter is found to increase in the order of PECS, SLM-2 and SLM-1, demonstrating that the amount of vacancy defects is rising in that order, and SLM-1 exhibits the maximal amount of vacancies among all specimens. The difference results from the cooling rate variation during the fabrication process (**Publication II**). Under a high cooling rate, more vacancies are retained in the solid, because the thermal vacancies are less annealed out during rapid cooling. The cooling rate in SLM process is much higher than that in PECS process, and a higher scanning speed is applied in SLM-1, consequently, the amount of vacancies in SLM-1 is the largest (**Publication II**).  $S$  parameter versus  $W$  parameter values of the tested specimens are plotted in Fig. 4.2b. The ( $S, W$ ) -data points obtained in one sample can be easily fitted to a straight line and all other sample data points are also approximately distributed along that same line. This indicates that in all tested specimens, merely one type of vacancy defect is identified, and the structure of the vacancies are similar (**Publication II**).

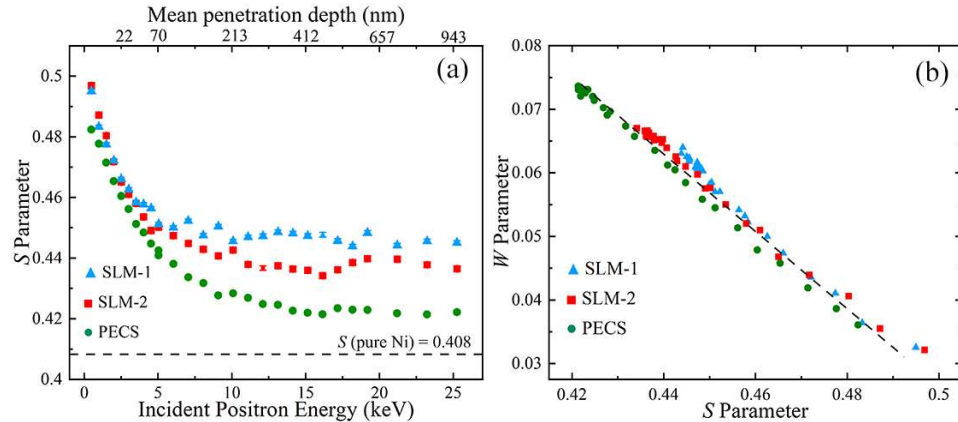


**Fig. 4.2.** Doppler broadening positron annihilation spectra determined on SLM- and PECS-built CrFeNiMn specimens and reference pure Ni sample. (a)  $S$  parameter as a function of implanted positron energy. (b)  $S$  parameter versus  $W$  parameter. Error bars are within the size of the markers [**Publication II**].

As a result of RS, the microstructure in SLM-built specimens is different from that obtained by other manufacturing processes, especially the conventional methods. A representative hierarchical microstructure introduced by SLM

process is given based on the SEM observations on the xy-plane of SLM-2 CrFeNiMn alloy, as summarized and depicted in Fig. 4.3. The electrochemically etched surface shows tracks of melt pools, and the mechanically polished surface presents the grain structures, as displayed by the back-scattered electrons (BSE) images in Figs. 4.3a and b, respectively. A high magnification secondary electron (SE) image in Fig. 4.3c manifests more microstructural features, such as melt pool boundaries (as indicated by dashed lines), equiaxed cells, elongated cells, and nano-inclusions. All types of cellular structures produced by SLM process are further observed individually, including dendritic cells, equiaxed cells, and elongated cells, as shown in Figs. 4.3d, e, and f, respectively. In the island scanning strategy, re-melting of the former scan by the next scan always occurs in the area where these two adjacent and parallel melt pools overlap. The dendrites are thereby resulted from the epitaxial growth along the building direction, which is opposite to the heat flux direction [105]. The formation of equiaxed and elongated cells is attributed to the differences in temperature gradient and solidification velocity at the solid-liquid interface [106]. Nano-inclusions tend to embed at the walls of cellular structure. Moreover, as further magnified in Fig. 4.3g, ultrafine sub-cells inside the general cells are identified on most of the surface area (**Publication I**).

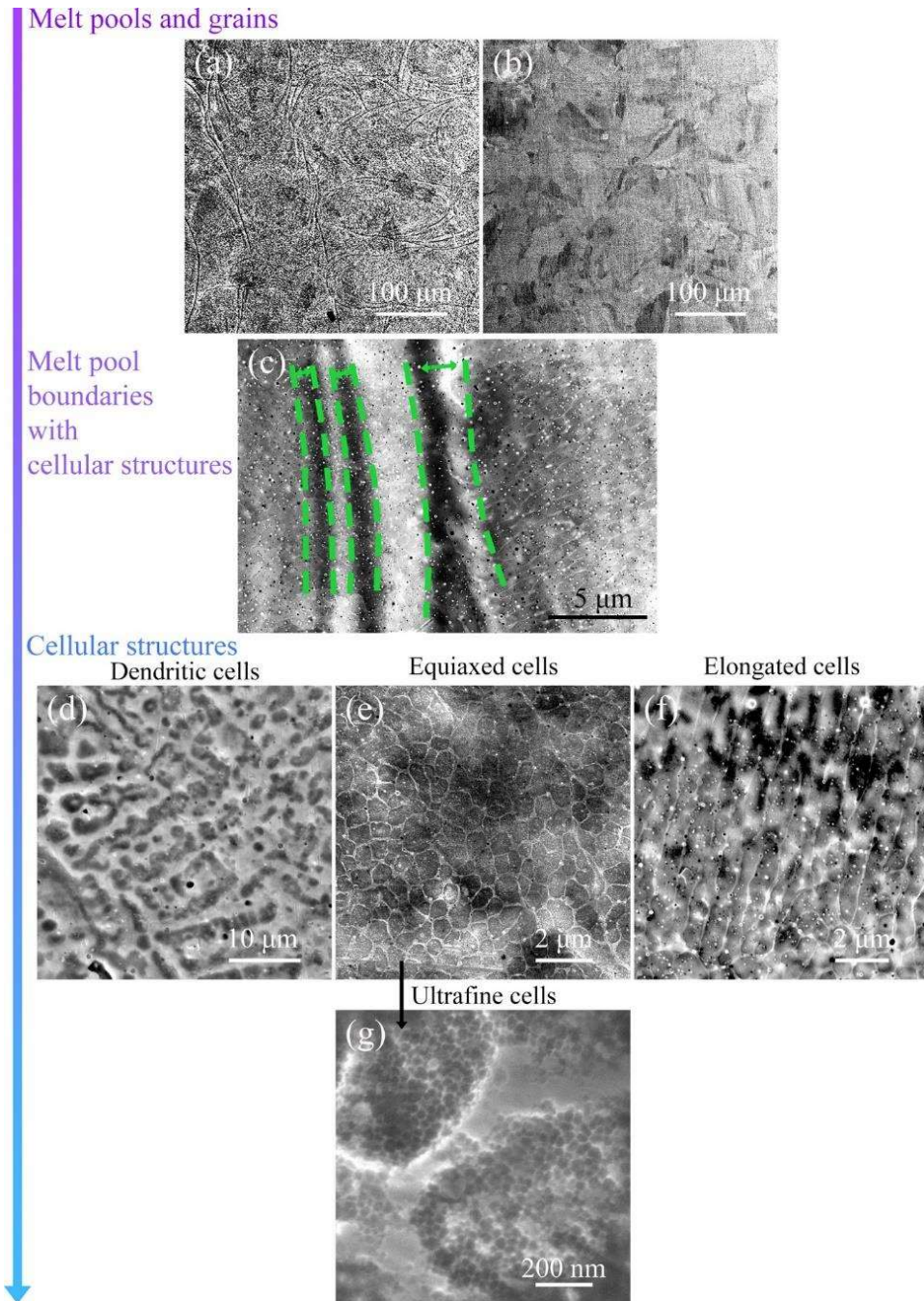


**Fig. 4.3.** Typical SLM-produced hierarchical microstructure obtained on the xy-plane of SLM-2 CrFeNiMn alloy. BSE micrographs showing (a) tracks of melt pools and (b) grains. SE images presenting (c) melt pool boundaries and cellular structures including (d) dendritic cells, (e) equiaxed cells, (f) elongated cells, (g) ultrafine cells. (g) represents a random magnified area in (e). Green dashed lines in (c) indicate melt pool boundaries.

SEM elemental distribution maps of microstructural features are displayed in Fig. 4.4. Mn and Ni are found to slightly enrich at the boundaries of melt pools, in which Cr and Fe are depleted, as depicted in Figs. 4.4a-1 and a-2. The circled particle indicates the presence of Mn-enriched nano-inclusion. Similar segregation is also detected at the walls of dendritic cells, as shown in Figs. 4.4b-1 and b-2. Furthermore, the circled particle suggests the formation of Mn-Cr-enriched nano-inclusion.

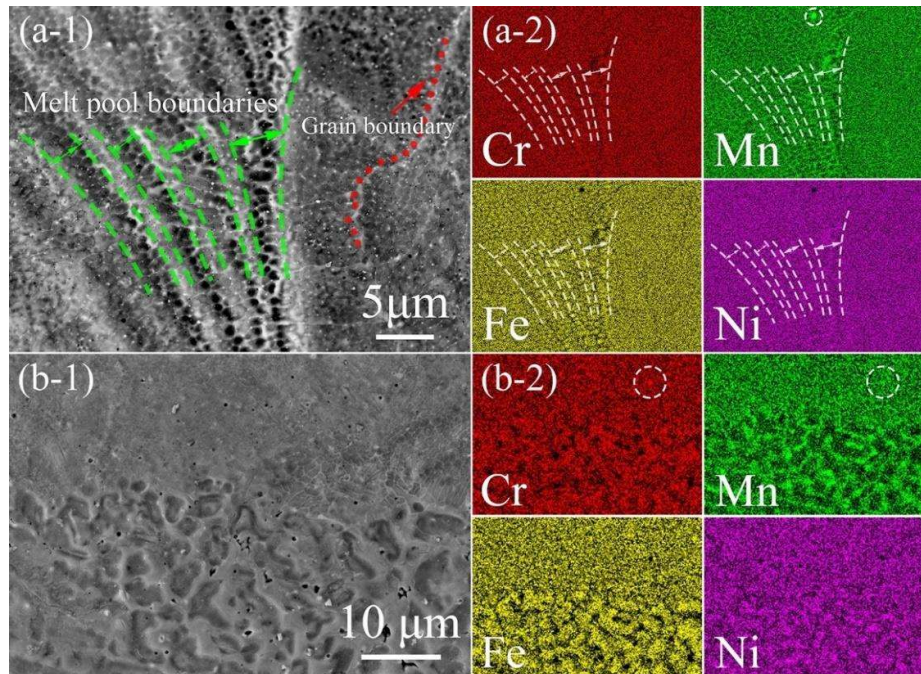


**Fig. 4.4.** SE images on the xy-plane of SLM-2 CrFeNiMn alloy displaying (a-1) melt pool boundaries and (b-1) dendritic cells with quantitative elemental distribution analysis in (a-2) and (b-2), respectively (adapted from **Publication I**).

TEM observations and elemental distribution analysis are presented in Fig. 4.5. The bright-field scanning transmission electron microscope (BF-STEM) image in Fig. 4.5a-1 depicts a large density of dislocations networks constituting the boundaries of cellular structures inside the grains. Mn and Ni segregate at the grain boundaries and cell walls, as demonstrated by corresponding EDS mapping analysis in Fig. 4.5a-2. Mn map delineates that nearly all the Mn-enriched nano-inclusions are embedded at the cell walls. The elemental map of Cr depicts that the Cr-enriched nano-inclusions also have a tendency to locate close to the cell walls, although some are evidenced within the cells. Furthermore, dislocations are also found within the cells. Inside one typical cell, ultrafine sub-cells with an estimated size from 150 to 300 nm are observed, as shown in Figs. 4.5b-1 and b-2. Mn enriches mostly at the sub-cell walls, in which a greater density of dislocations concentrates. On the other hand, part of the sub-cell walls exhibits dislocations yet without the segregation.

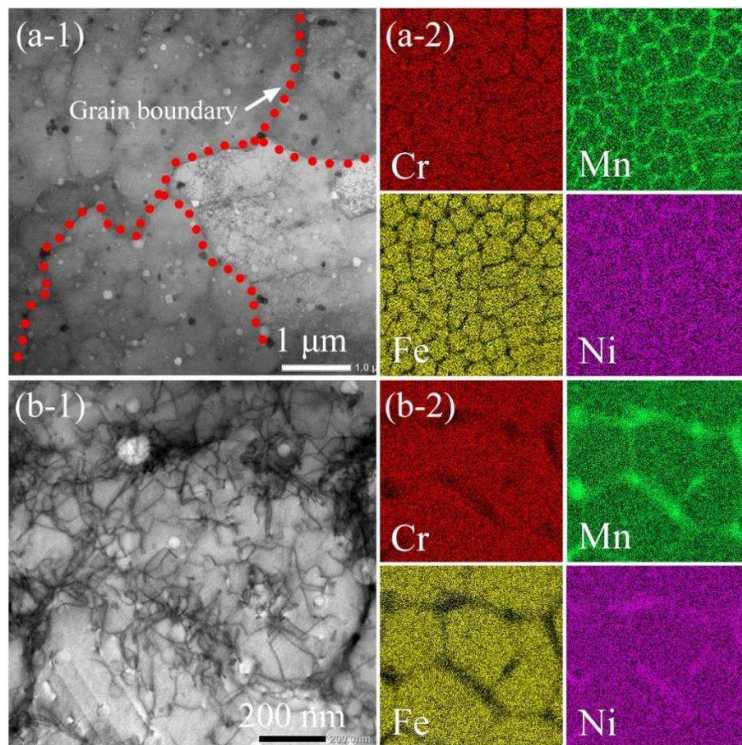


**Fig. 4.5.** BF-STEM images on the xy-plane of SLM-2 CrFeNiMn alloy depicting (a-1) equiaxed cells and (b-1) sub-cell structure with quantitative elemental distribution analysis in (a-2) and (b-2), respectively (adapted from **Publication I**).

At the beginning of solidification, due to the presence of temperature gradient, the portions of the solid-liquid interface enriched with high melting point elements, i.e., Cr and Fe, are solidified prior to the other parts of interface, and form protuberances. While the low melting point elements are rejected by the solidified material, referring to Mn and Ni in this case, they are inclined to concentrate in the melt at the solid interface and slow down the growth. As a consequence, the interface solidifies into cellular structures, with segregation of Mn and Ni at the cell walls. The Mn-enriched nano-inclusions are likely to originate from the recondensation of evaporated Mn. The Mn-Cr-enriched nano-inclusions are formed due to the reaction with residual oxygen in the chamber of SLM equipment, as both elements exhibit a higher affinity to oxygen than the other two elements (**Publication I**).

Employing a higher cooling rate contributes to the refining of microstructure, and correspondingly properties such as Vickers hardness alter as well (**Publication I**). The average equiaxed cell size of SLM-1 is estimated to be 390 nm, and that of SLM-2 is approximately 520 nm. As a result, SLM-1 exhibits a higher hardness of  $248 \pm 8$  HV<sub>0.5</sub>, and SLM-2 exhibits a hardness of  $221 \pm 14$  HV<sub>0.5</sub>. It can be therefore summarized that when applying a higher scanning speed under the same laser power, more uniform and refined cellular structures possessing less segregation of alloying elements are formed. In combination with the residual stress, cellular structure, high density of dislocations and nano-inclusions produced by SLM, as well as the high controllability of SLM, better and desired mechanical properties are feasible to achieve by optimizing process parameters (**Publication I**).

#### 4.1.2 Hydrogen induced effects

Hydrogen induced effects on the TEM disc prepared from xy-plane of SLM-2 CrFeNiMn specimen were studied using electrochemical introduction of hydrogen into the sample. After 3 h of aging, some stacking faults are observed, as presented in Fig. 4.6a. They are introduced by the hydrogen gradient induced stress field, and appear magnified in the dark-field (DF) TEM image of Fig. 4.6b. This suggests that a decrease of stacking fault energy results from the introduction of hydrogen. Identical effect has also been detected in conventional austenitic stainless steels (ASS) [107,108]. Hydrogen-induced cracking and subsequent failures initiate from stress gradient and/or phase transitions, according to the stability of austenite [109], i.e., cracking as well as  $\alpha'$ - and  $\varepsilon$ -martensite formation are found in metastable ASS [110], and merely expanded FCC phase structure and correlative deformation occur in high-alloyed stable ASS [111]. Here, the high-alloyed stable ASS correspond to steels containing alloying elements which is high enough to prevent the deformation induced martensite formation, i.e.,  $M_d$  temperature must be below room temperature [112]. Furthermore, cracks are observed along the planar faults, and after 24 h of aging, part of the specimen is separated along the cracks, as circled with the green dotted lines in Figs. 4.6a and d. Fig. 4.6c shows an FCC-structured ring pattern from nanocrystals located in one matrix grain, overlapping with spot pattern from the matrix, which suggests the lattice parameter of the nanocrystals is very similar to that of the matrix. The nanocrystals can likely be attributed to the hydrogen-induced deformation, which results from the increase of volume upon hydrogen charging (**Publication II**). DF TEM image of magnified (blue) rectangular area in (b) shows the presence of planar defects, most likely overlapping with stacking faults. It is possible that the localized high hydrogen concentration in the tensile strain field of dislocations may also result in the hydride formation distributed along the dislocation lines [113]. The elemental distribution analysis in Fig. 4.6e, taken from the region shown in Fig. 4.6d, displays that cracks propagate along the grain boundaries and cell walls area.

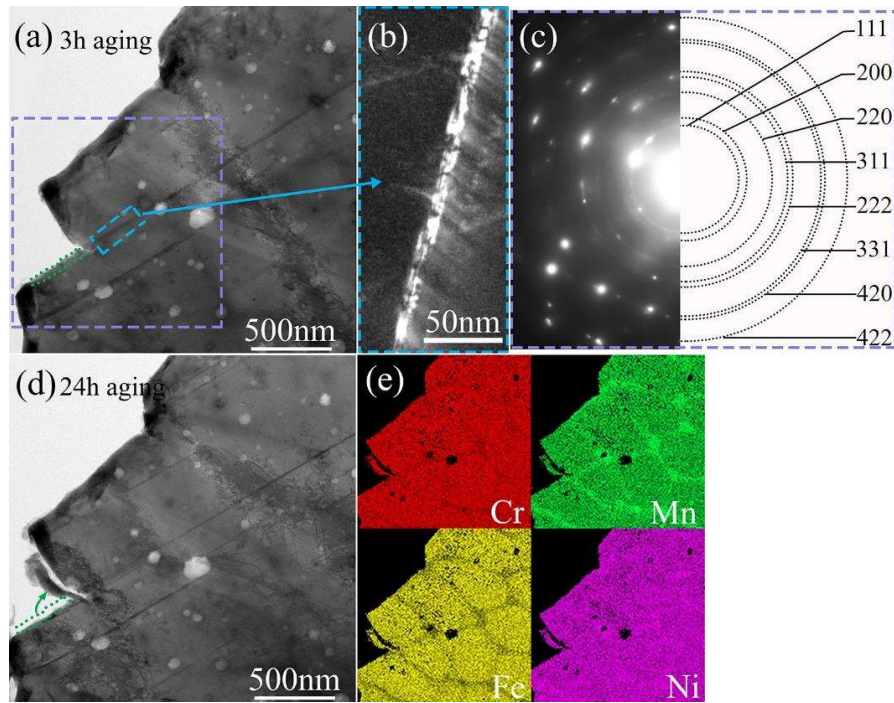


**Fig. 4.6.** TEM micrographs on the xy-plane of hydrogen-charged SLM-2 CrFeNiMn alloy. (a) BF-STEM image taken after 3 h of aging. (b) DF-TEM image of magnified rectangle area in (a) depicting planar defects, most presumably be overlapping stacking faults. (c) SAD and ring pattern obtained from purple rectangle (d) BF-STEM image taken after 24 h of aging with (e) quantitative elemental distribution analysis (adapted from **Publication II**).

Hydrogen uptake abilities of SLM-2, SLM-1, PECS and reference 316L steel were evaluated by TDS, as illustrated in Fig. 4.7. The first peak of all the four TDS curves is located near a temperature of 200 °C, and the peak height decreases in the order of SLM-2, SLM-1, PECS and 316L steel. The amount of absorbed hydrogen in each specimen is determined from the area under the curve, and also decreases in the order of SLM-2, SLM-1, PECS and 316L steel, and the corresponding amounts are estimated to be 423, 311, 239, and 23 wppm, respectively. A second peak is also revealed in each SLM specimen, located at a temperature of 337 °C, and SLM-2 has a higher second peak than SLM-1.

In a TDS curve, peaks located at different temperatures correspond to the hydrogen binding in different trapping sites, i.e., the higher the binding energy is, the higher the required temperature is. The first peak located at around 200 °C refers to the hydrogen released from relatively weak trapping sites, including dislocations and interstitial sites [114]. SLM- and PECS-built specimens exhibit higher first peaks than 316L steel, which suggests that a larger concentration of hydrogen is trapped in the weak trapping sites of these specimens. The higher first peaks in SLM-built specimens than that in PECS sample are caused by the greater density of dislocations in SLM-built specimens. The second peak merely revealed in each SLM-built specimen, at a temperature of 337 °C, relates to defects such as vacancies [115]. Since similar porosity and no blistering are observed in SLM-built specimens, the main factors determining the absorbed hydrogen concentration are considered to be dislocations and vacancies. However, SLM-1 has a higher density of vacancy defects than SLM-2 due to the

employed faster cooling rate, as presented in Fig. 4.2. Therefore the observed low intensity of second peak in SLM-1 indicates that the vacancies do not appear to contribute significantly to the absorption of hydrogen. This peak is thus likely ascribed to the hydrogen diffused across the thickness of specimen and released from the opposite side of surface (**Publication II**).

More hydrogen is clearly absorbed by the CrFeNiMn alloy than conventional 316L steel, whether being produced by SLM or PECS. This is attributed to the higher content of Cr and Mn elements, as well as higher lattice strain energy and short-range order in the multicomponent alloys. SLM-induced hierarchical microstructure (see in Fig. 4.3) is further beneficial for the hydrogen uptake ability, due to the high density of dislocations, as well as the cellular structure in combination with the segregation of Cr and Mn element (**Publication II**). Lin et al. [63] stated that the walls of cellular structure act as rapid transportation paths for hydrogen. This is in agreement with our observation that a higher absorbed hydrogen concentration is present in SLM-2 sample than in SLM-1 sample. This is attributed to the severer segregation at consequently broader cell walls found in SLM-2 (**Publication II**).

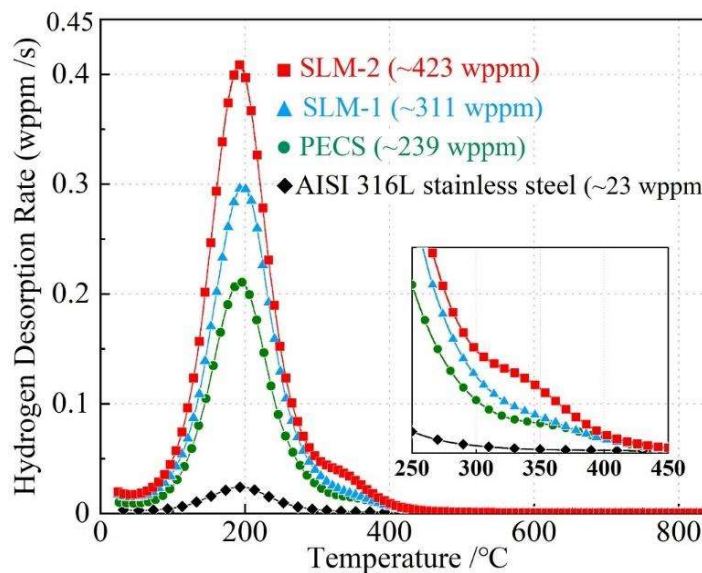


**Fig. 4.7.** TDS spectra of SLM- and PECS-prepared CrFeNiMn specimens and reference AISI 316L stainless steel [**Publication II**].

A small peak in relation to the formation of BCC phase is determined by XRD after TDS test, in each SLM-built specimen, as presented in Fig. 4.8. The peak is noticeably reduced after polishing off  $\sim 150 \mu\text{m}$  from surface, yet it remains detectable. Furthermore, the chemical composition listed in Table 4.2 demonstrates that Mn loss occurs in SLM-built specimens during the TDS test, and SLM-2 experiences the most loss among all specimens. However, the Mn content increases back to the as-built composition after polishing off  $\sim 150 \mu\text{m}$  from the surface. These results indicate that the BCC phase is likely to form due to a) Mn loss, which decreases the FCC phase stability; or b) deformation-

induced martensite transformation caused by hydrogen gradient (**Publication II**).

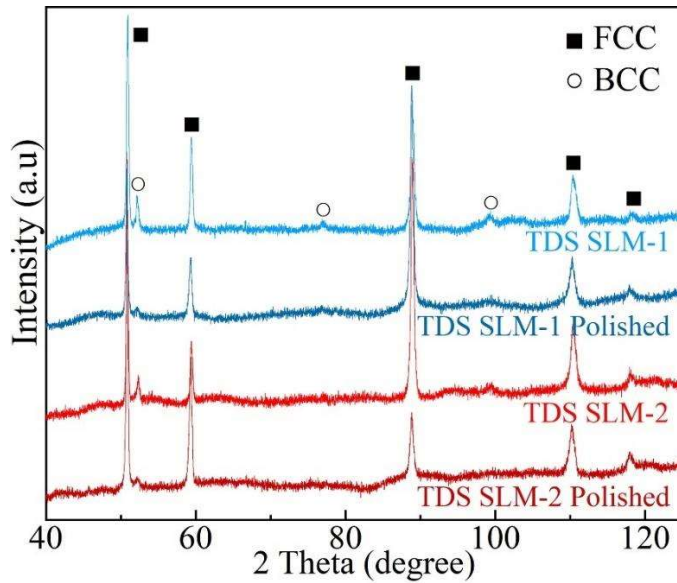


**Fig. 4.8.** XRD curves of TDS-tested SLM-built CrFeNiMn specimens before and after polishing off ~150  $\mu\text{m}$  from the surface [**Publication II**].

**Table 4.2.** Porosity and chemical composition (in at%) of SLM-built CrFeNiMn specimens before and after TDS tests. Most of the measurement errors of chemical composition are below 0.3 at% for all elements except Mn element, which varies more noticeably due to segregation.

Specimen	Porosity	Chemical composition (at%)			
		Cr	Mn	Fe	Ni
SLM-1	2.0	25.5	24.9	24.8	24.8
TDS SLM-1	-	25.7	24.7	25.0	24.6
TDS SLM-1 Polished	-	25.1	25.0	25.2	24.7
SLM-2	2.1	25.8	24.0	25.3	24.9
TDS SLM-2	-	26.1	23.4	25.5	25.0
TDS SLM-2 Polished	-	25.3	23.9	25.6	25.2

Analysis on the TDS-tested specimens presents other differences. SE images in Figs. 4.9a-1 and b-1 indicate the formation of pits distributed along the grain boundaries, and the TDS-tested SLM-2 specimen reveals a more rough and uneven morphology in comparison to the TDS-tested SLM-1 specimen. These pits exhibit depths and widths in the submicron scale, and they are deeper and broader on the surface of TDS-tested SLM-2 specimen than on that of TDS-tested SLM-1 specimen, as shown in Figs. 4.9a-2 and b-2. The pits are likely to result from the hydrogen-induced cracking and detachment of inclusions.

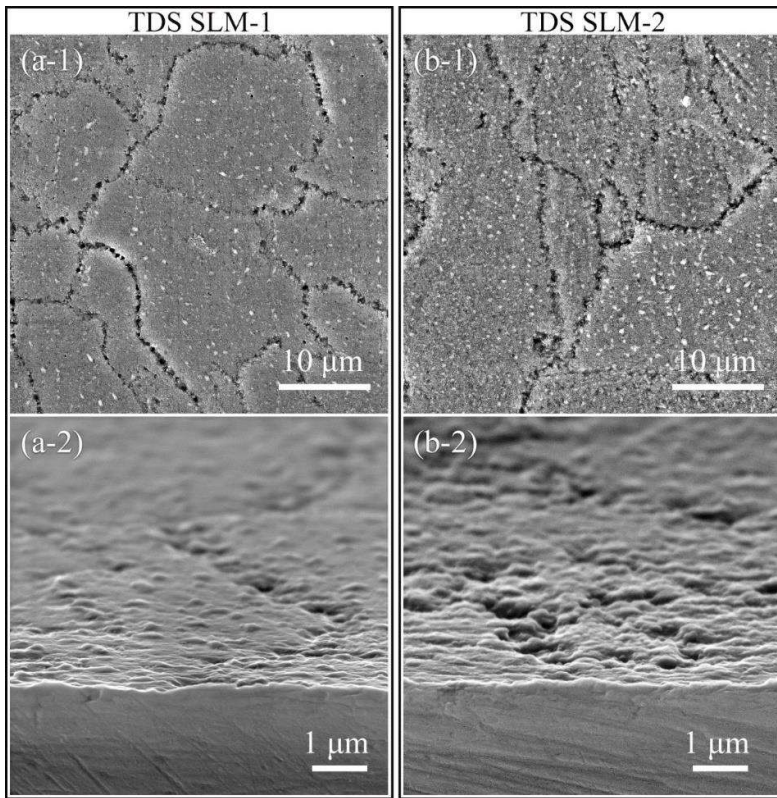


**Fig. 4.9.** SE micrographs on the (a-1) xy-plane and (a-2) xz-plane of TDS-tested SLM-1 CrFeNiMn specimen, and on the (b-1) xy-plane and (b-2) xz-plane of TDS-tested SLM-2 CrFeNiMn specimen.

Fig. 4.10 displays the BSE images on the xy-plane of TDS-tested SLM-1 and SLM-2 specimens and their corresponding SEM-EDS line scan results across the surface. It can be seen that the Cr and Fe content reveal an identical variation trend, and Mn content varies along with Ni content. This is ascribed to the Mn and Ni elements segregation detected in the cell walls as well as boundaries of grains and melt pools. All four alloying elements in TDS-tested SLM-2 specimen fluctuate more noticeably than those in TDS-tested SLM-1 specimen. Furthermore, Mn content fluctuation in SLM-2 before TDS test is from 22.9 to 25.3 at%, and after TDS test is from 21.9 to 25.2 at%. As Mn content decreases during TDS test, the atomic percent of other elements increases accordingly.

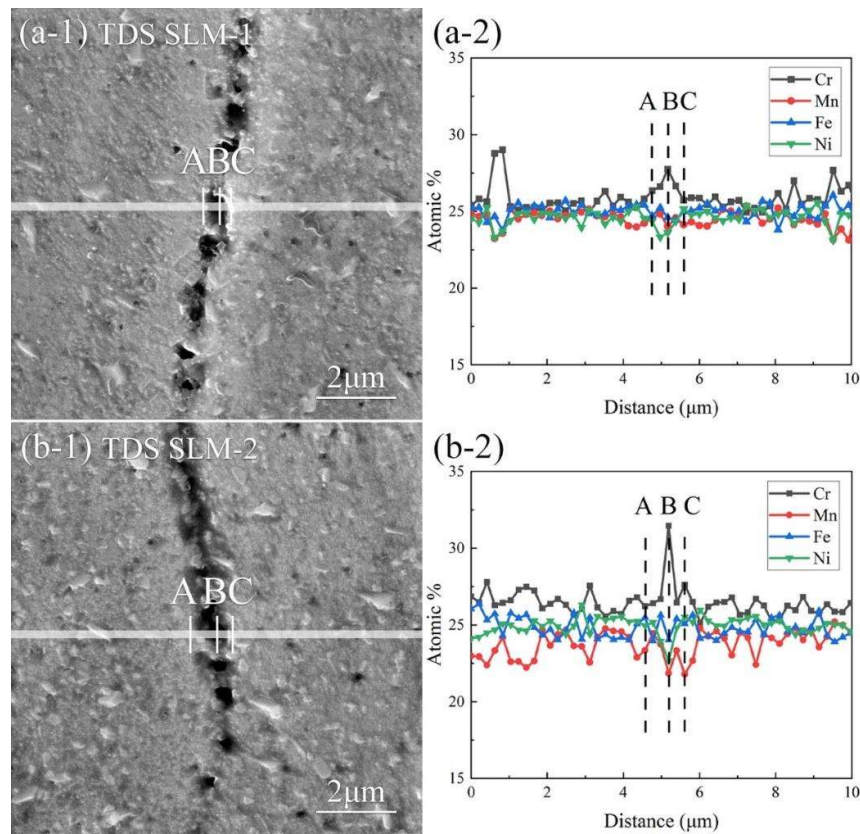


**Fig. 4.10.** BSE micrographs on the xy-plane of TDS-tested SLM-built CrFeNiMn specimens with corresponding SEM-EDS line scan analysis [adapted from **Publication II**].

## 4.2 AlCoCr<sub>0.75</sub>Cu<sub>0.5</sub>FeNi alloy produced via SLM

### 4.2.1 SLM-produced microstructure

The influences of two sets of process parameters, i.e., i) same laser power of 200 W with various scanning speeds and ii) same VED of 55.56 J/mm<sup>3</sup> with different combinations of laser power and scanning speed, on the physical and chemical properties of SLM-built AlCoCr<sub>0.75</sub>Cu<sub>0.5</sub>FeNi specimens are summarized in Table 4.3. Additionally, one reference PECS sample was investigated for comparison. It is found that the highest Archimedes density (AD) of  $7.070 \pm 0.017$  g/cm<sup>3</sup> and the highest relative density (RD) of ~97% are produced by employing the largest VED input of 92.59 J/mm<sup>3</sup>. Under the same laser power of 200 W, with scanning speed is increased from 1200 to 2000 mm/s (corresponding to a decline of VED from 92.59 to 55.56 J/mm<sup>3</sup>), both AD and RD slightly decrease. Under the same VED of 55.56 J/mm<sup>3</sup>, AD and RD also show a declining trend when the laser power and scanning speed are decreased from 200 W and 2000 mm/s to 160 W and 1600 mm/s.

Vickers microhardness was determined on both xy- and xz-plane of the SLM-built AlCoCr<sub>0.75</sub>Cu<sub>0.5</sub>FeNi specimens. As displayed in Table 4.3, the highest microhardness values of  $603.6 \pm 6.8$  HV<sub>0.05</sub> on xy-plane and  $598.6 \pm 7.5$  HV<sub>0.05</sub> on xz-plane are achieved when applying the largest VED input of 92.59 J/mm<sup>3</sup>. The microhardness of each specimen on xy- and xz-plane is similar, as

the difference between two planes fall within the measurement uncertainty. While each specimen on xy-plane exhibits a slightly higher average value of microhardness than on xz-plane. When the scanning speed is increased from 1200 to 2000 mm/s, VED decreases accordingly from 92.59 to 55.56 J/mm<sup>3</sup>, but the microhardness is found to alter only slightly. However, even though a same VED is applied, as both laser power and scanning speed are declined, the microhardness is lowered noticeably. Anyhow, the hardness of each SLM-built specimen is higher than that of the reference PECS sample. The microhardness of SLM-built specimens reveals a nearly linear relation with RD, i.e., the microhardness is enhanced with decreasing porosity (**Publication III**). PECS sample retains the chemical composition of the starting powder. A slight loss of aluminum likely due to evaporation is detected in the SLM-built specimens when compared to other alloying elements (**Publication III**). The content of copper reduces as well, but not as clearly. As a result, the contents of the other four elements increase marginally. Furthermore, it is observed that among all employed process parameters, the variation of VED, scanning speed or laser power does not influence the Al content significantly (**Publication III**).

**Table 4.3.** Physical and chemical properties of SLM- and PECS-built AlCoCr<sub>0.75</sub>Cu<sub>0.5</sub>FeNi specimens, along with chemical composition of starting powder.

Sample	Archimedes density (g/cm <sup>3</sup> )	Relative density (%)	Vickers microhardness (HV0.05)		Element (at%)					
			xy	xz	Al	Cu	Fe	Ni	Co	Cr
Powder [90]	-	-	-	-	19.5	9.57	18.8	19.5	19.6	12.9
VED = 92.59 J/mm <sup>3</sup> (P = 200 W, v = 1200 mm/s)	7.070 ± 0.017	96.95 ± 0.23	603.6 ± 6.8	598.6 ± 7.5	17.8 ± 0.12	9.3 ± 0.01	19.2 ± 0.09	20.1 ± 0.05	20.5 ± 0.04	13.1 ± 0.03
VED = 74.07 J/mm <sup>3</sup> (P = 200 W, v = 1500 mm/s)	7.039 ± 0.015	96.54 ± 0.20	583.7 ± 10.4	577.2 ± 10.9	17.8 ± 0.35	9.3 ± 0.02	19.2 ± 0.13	20.0 ± 0.08	20.5 ± 0.10	13.2 ± 0.08
VED = 55.56 J/mm <sup>3</sup> (P = 200 W, v = 2000 mm/s)	7.041 ± 0.023	96.73 ± 0.32	598.3 ± 10.7	590.1 ± 12.3	18.1 ± 0.10	9.4 ± 0.02	19.1 ± 0.03	19.8 ± 0.07	20.3 ± 0.02	13.3 ± 0.03
VED = 55.56 J/mm <sup>3</sup> (P = 180 W, v = 1800 mm/s)	6.929 ± 0.015	94.91 ± 0.21	572.7 ± 16.3	567.0 ± 12.7	17.7 ± 0.30	9.5 ± 0.05	19.1 ± 0.08	20.0 ± 0.07	20.4 ± 0.07	13.3 ± 0.08
VED = 55.56 J/mm <sup>3</sup> (P = 160 W, v = 1600 mm/s)	6.898 ± 0.014	94.48 ± 0.19	567.2 ± 17.2	559.5 ± 16.2	17.6 ± 0.26	9.5 ± 0.02	19.2 ± 0.04	20.0 ± 0.10	20.4 ± 0.13	13.3 ± 0.06
PECS sample	7.235 ± 0.014	-	409.5 ± 4.2 HV1		19.3 ± 0.15	9.6 ± 0.09	18.7 ± 0.07	19.6 ± 0.06	19.9 ± 0.09	12.9 ± 0.08

Surface morphologies on xy- and xz-plane of three specimens are displayed in Fig. 4.11. It can be noted that the porosity results from cracks, gas pores and lack-of-fusion defects. Gas pores are produced in a smaller and near-spherical form. Lack-of-fusion defects are revealed with a relatively large size and irregular shape. The specimen produced with the highest VED of 92.59 J/mm<sup>3</sup> (P = 200 W, v = 1200 mm/s) exhibits relatively fewer defects, mainly consisting of cracks and gas pores, as shown in Figs. 4. 11a-1 and b-1. When the VED is decreased to 55.56 J/mm<sup>3</sup> (P = 200 W, v = 2000 mm/s), the three types of

defects are observed more frequently, especially the lack-of-fusion defects, as manifested and pointed with arrows in Figs. 4.11b-1, b-2. Furthermore, under the same VED of  $55.56 \text{ J/mm}^3$ , more lack-of-fusion defects are produced due to laser power is reduced from 200 to 160 W, as presented and indicated with arrows in Figs. 4.11c-1 and c-2. These observations demonstrate that laser power, scanning speed and VED need to be optimized carefully, as their influences lie on different aspects. Laser power is the key to carry out full melting of the powder, which is crucial to high relative density, and good mechanical properties. Scanning speed determines the formation of microstructural features including elemental distribution as well as the size of grains and cells. VED refers to the combined effects of former two parameters, yet it alone is inadequate to predict the quality of the final product (**Publication III**).

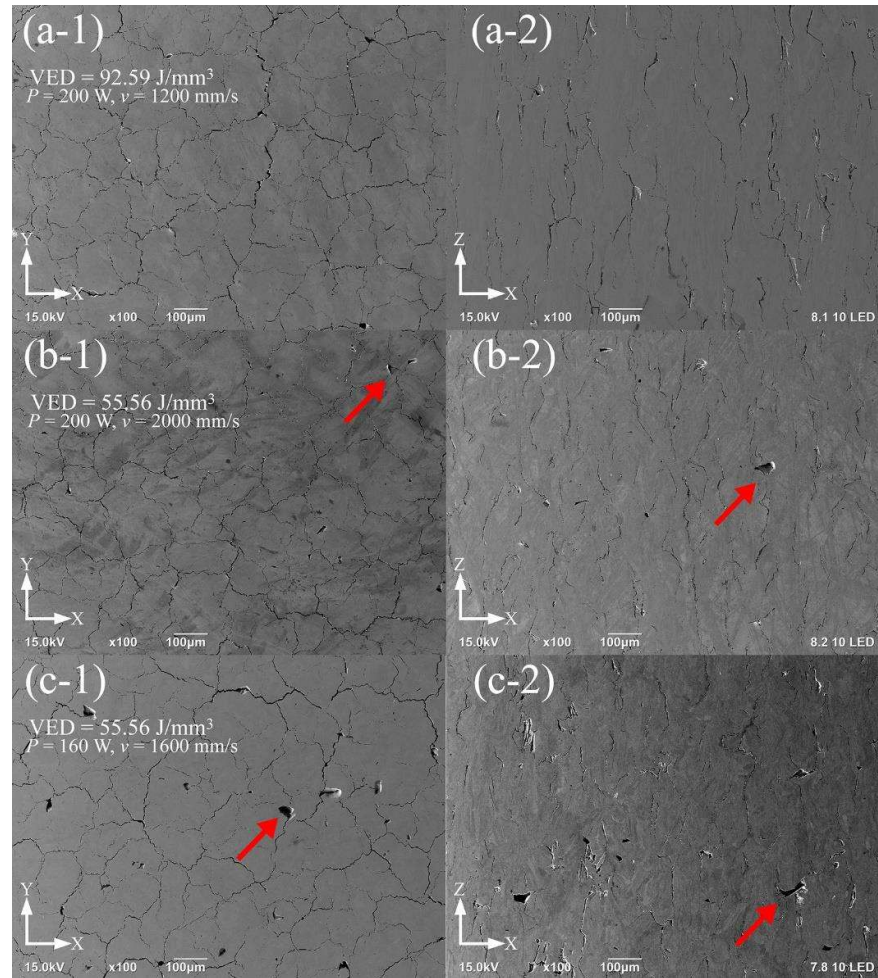


**Fig. 4.11.** Surface morphology of different SLM-built  $\text{AlCoCr}_{0.75}\text{Cu}_{0.5}\text{FeNi}$  specimens. (a-1) and (a-2) refer to images of one sample obtained on xy- and xz-plane, respectively. Same for the other two samples. Representative lack-of-fusion defects are indicated with arrows in (b-1), (b-2), (c-1) and (c-2).

Some representative microstructural features are presented in Fig. 4.12, where SEM characterization is performed on a specimen fabricated with the VED of  $55.56 \text{ J/mm}^3$  ( $P = 200 \text{ W}$ ,  $v = 1200 \text{ mm/s}$ ). On the surface of the mechanically

polished sample shown in Fig. 4.12a, elongated grains along with some cracks are observed. On the other hand, grains on xy-plane are found to be polygonal equiaxed. The grain sizes on xy-plane determined by EBSD are  $\sim 9.84$  and  $\sim 9.47$   $\mu\text{m}$  correspondingly, for samples produced at the scanning speeds of 1200 and 2000 mm/s and employing the same laser power of 200 W (**Publication III**). A uniform elemental distribution at microscale is identified at the magnified BSE image in Fig. 4.12b as shown by the EDS mapping results. Figs. 4.12c and d display the typical cellular structures, melt pool boundaries and grain boundaries on the electrochemically etched surface, which are observed on both xy- and xz-plane, respectively. Most cells on xy-plane tend to be equiaxed, and those on xz-plane are elongated. The difference is caused by the thermal gradient (**Publication III**).

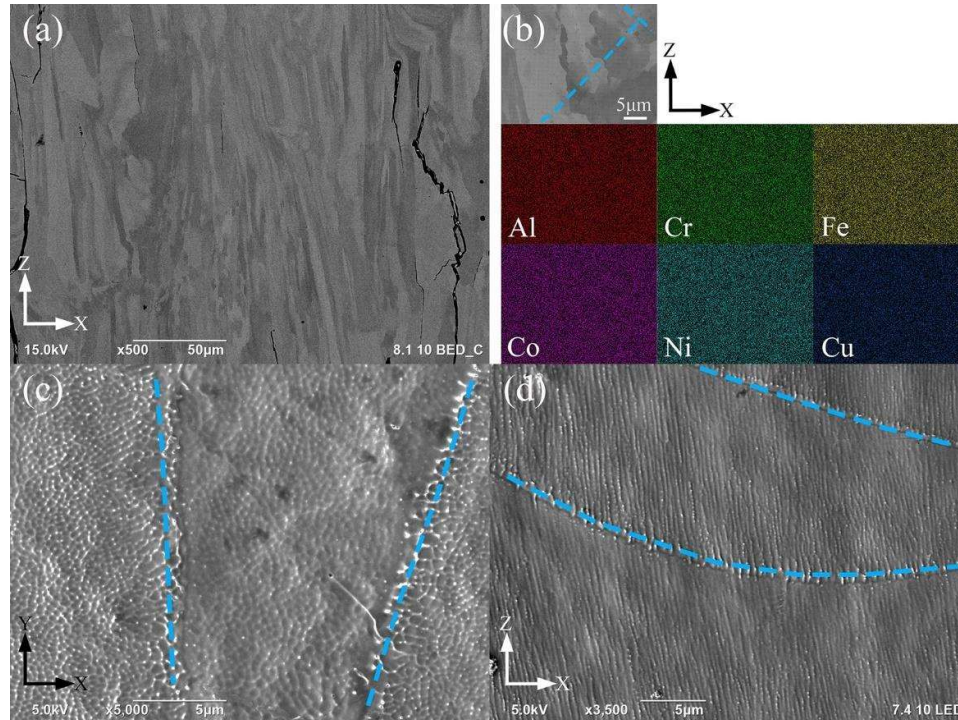


**Fig. 4.12.** SEM characterization on SLM-built  $\text{AlCoCr}_{0.75}\text{Cu}_{0.5}\text{FeNi}$  specimen produced with the VED of  $55.56 \text{ J/mm}^3$  ( $P = 200 \text{ W}$ ,  $v = 1200 \text{ mm/s}$ ). (a) BSE micrograph on xz-plane. (b) High magnification BSE micrograph on xz-plane with corresponding quantitative EDS maps. SE images on (c) xy-plane and (d) xz-plane. (a) and (b) are determined on the mechanically polished sample, (c) and (d) are obtained on the electrochemically etched sample. Blue dashed lines indicate melt pool boundaries.

Peaks corresponding to BCC phase are detected on both xy- and xz-plane of all SLM-built specimens, as shown in the XRD spectra in Fig. 4.13, while the PECS sample contains a mixture of FCC and BCC phases (**Publication III**). Fig. 4.13a displays a high intensity of 100 and 200 diffraction peaks on the xy-plane of the specimen produced by the largest VED input of  $92.59 \text{ J/mm}^3$ , indicating preferred orientation along  $\{100\}$  plane, perpendicular to the building direction. This preferred orientation gradually declines as the VED is reduced. The diffraction patterns on xy-plane appear to be similar when applying the same VED of  $55.56 \text{ J/mm}^3$ , despite the alterations in the

combination of laser power and scanning speed. Furthermore, the magnified  $2\theta$  in the range of  $51.5\text{--}53.5^\circ$  depicts that there is a shift of  $110$  peak of SLM-built specimens to a higher angle in comparison to powder. This suggests that the interplanar spacing in each bulk specimen is smaller than that in the powder (**Publication III**). Under the same laser power of  $200$  W, the degree of shift of  $110$  peak decreases when the scanning speed is increased. This implies that the stress concentration introduced by RS is growing due to the higher scanning speed. On the other hand, the diffraction patterns look similar on the  $xz$ -plane, as presented in Fig. 4.13b. The magnified  $2\theta$  in the range of  $51.5\text{--}53.5^\circ$  depicts the less shifted yet broader  $110$  peaks on  $xz$ -plane than those on  $xy$ -plane, which suggest that a larger lattice strain is produced by RS in SLM than in powder. The larger broadening might be related to the texture and non-symmetrical cellular structure (**Publication III**).

As has been observed both in [90] and **Publication III**, the starting  $\text{AlCoCr}_{0.75}\text{Cu}_{0.5}\text{FeNi}$  powder is constituted of a mixing of two types of BCC phase structures, i.e., ordered  $B_2$  phase and disordered  $A_2$  phase, as a result of spinodal decomposition. The phase separation into  $A_2$  and  $B_2$  structure appears at the early stage of solidification of melt, even when the cooling rate reaches  $10^6\text{--}10^7$  K/s [77]. In Fig. 4.13, the  $100$  peak refers to  $B_2$  phase, and  $200$  peak relates to the coexistence of  $A_2$  and  $B_2$  phase. Previous research works [15,89] have identified a single  $B_2$  structure in equiatomic  $\text{AlCoCrCuFeNi}$  alloys produced both by splat quenching and melt spinning. Because SLM exhibits a comparable cooling rate with those processes, it is likely that the specimen produced by the highest scanning speed of  $2000$  mm/s contains a single  $B_2$  phase.

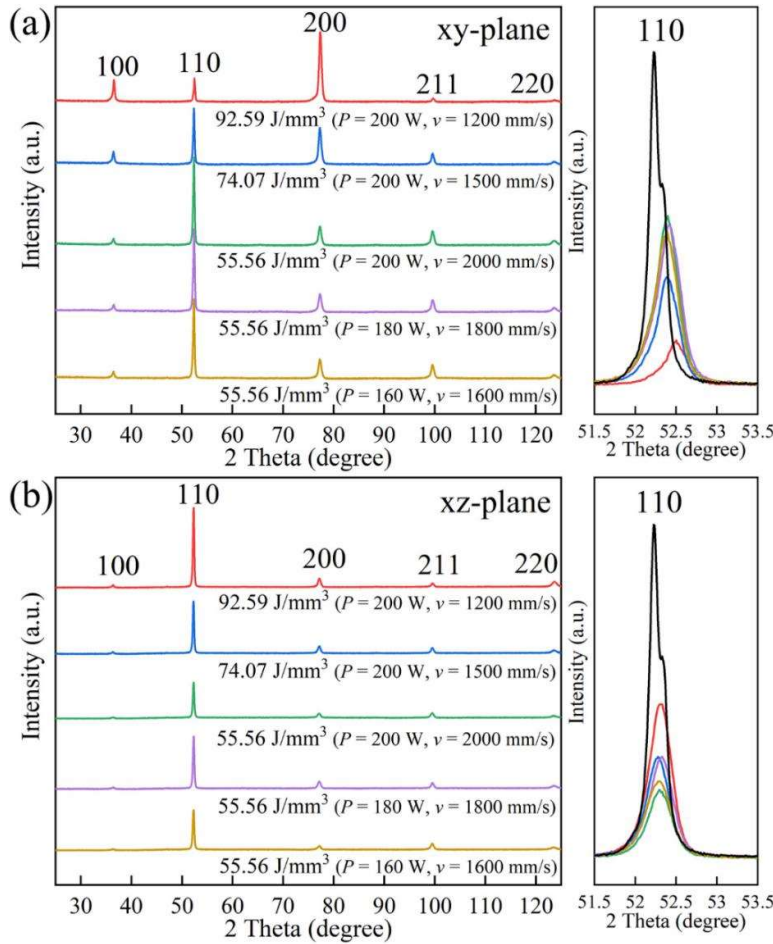


**Fig. 4.13.** XRD curves of SLM-built AlCoCr<sub>0.75</sub>Cu<sub>0.5</sub>FeNi specimens with magnified 2θ of 110 peak tested on (a) xy-plane (b) xz-plane.

#### 4.2.2 Tailoring magnetic properties by spinodal decomposition

The magnetization  $M$  versus magnetic field strength  $H$  curve of raw powder, SLM- and PECS-produced specimens, measured at temperatures of 10 K and 300 K, are presented in Figs. 4.14a and b, respectively. Soft magnetic behavior is identified in all tested specimens. Saturation magnetization  $M_s$  of each specimen at 9 T is presented in Table 4.4. When comparing to two sets of powder with different particle class size, all SLM-produced specimens reveal higher values of  $M_s$  both at 10 and 300 K.  $M_s$  is found to be decreasing as the scanning speed is increased under the same laser power, while it shows merely a small distinction among three specimens produced by the same VED input. Overall, each SLM-built specimen in this research reveals a higher  $M_s$  than previously reported alloys with similar compositions, including the splat-quenched AlCoCrCuFeNi alloy possessing a  $M_s$  of 41 emu/g evaluated at 320 K [77]. Moreover, a similar ratio  $M_s$  (300 K)/ $M_s$  (10 K) and declining trend of  $M_s$  suggest that SLM-built specimens exhibit a close to ferromagnetic Curie temperature ( $T_c$ ) (**Publication III**). Coercive force of the SLM-built specimen is estimated to be close to that of the starting powder, which implies that internal stress only marginally affects the magnetic properties. For comparison,

$M_s$  of the PECS sample is the lowest among all. Moreover, Fig. 4.14c displays that  $M_s$  of the specimen produced by applying a VED of  $74.07 \text{ J/mm}^3$  ( $P = 200 \text{ W}$  and  $v = 1500 \text{ mm/s}$ ) obtained at  $2 \text{ T}$  and  $305 \text{ K}$  is increased by  $10 \text{ emu/g}$  after annealing for 10 minutes at a temperature of  $800 \text{ K}$ .

$M_s$  of the SLM-built specimen is dependent on the degree of spinodal decomposition in each specimen, and the decomposition is controlled by the cooling rate, i.e., under a relatively low cooling rate, more Fe-Cr-rich A2 phase having strong ferromagnetism and less Al-Ni-rich B2 phase having weak ferromagnetism are produced (**Publication III**). Accordingly, under the same laser power of  $200 \text{ W}$ ,  $M_s$  is increased as the scanning speed is reduced from  $2000$  to  $1200 \text{ mm/s}$ , as displayed in Table 4.4. This enhancement of  $M_s$  at  $300 \text{ K}$  is comparable with what Singh et al. [77] achieved by annealing the as-cast AlCoCrCuFeNi alloy at a temperature of  $600 \text{ }^\circ\text{C}$  for 2 hours, which proves that SLM yields an efficient method to design and improve the magnetic properties without time-consuming heat treatments (**Publication III**). Once the relations among cooling rate, spinodal decomposition and magnetic properties are well established, the desired magnetic properties can be materialized via the high controllability of SLM.

**Table 4.4.** Saturation magnetization at  $9 \text{ T}$  of starting powder, SLM- and PECS-built AlCoCr<sub>0.75</sub>Cu<sub>0.5</sub>FeNi specimens evaluated at  $10$  and  $300 \text{ K}$  [adapted from **Publication III**].

Sample	$M_s$ (emu/g)		
	10 K	300 K	$M_s$ (300 K)/ $M_s$ (10 K)
VED = $92.59 \text{ J/mm}^3$ ( $P = 200 \text{ W}$ , $v = 1200 \text{ mm/s}$ )	80.5	65.3	0.81
VED = $74.07 \text{ J/mm}^3$ ( $P = 200 \text{ W}$ , $v = 1500 \text{ mm/s}$ )	80.1	64.4	0.80
VED = $55.56 \text{ J/mm}^3$ ( $P = 200 \text{ W}$ , $v = 2000 \text{ mm/s}$ )	78.7	63.0	0.80
VED = $55.56 \text{ J/mm}^3$ ( $P = 180 \text{ W}$ , $v = 1800 \text{ mm/s}$ )	78.9	63.0	0.80
VED = $55.56 \text{ J/mm}^3$ ( $P = 160 \text{ W}$ , $v = 1600 \text{ mm/s}$ )	78.9	62.6	0.79
PECS sample	33.9	17.6	0.52
Powder ( $20\text{-}63 \mu\text{m}$ )	71.3	55.3	0.78
Powder ( $< 200 \mu\text{m}$ )	68.4	53.8	0.79

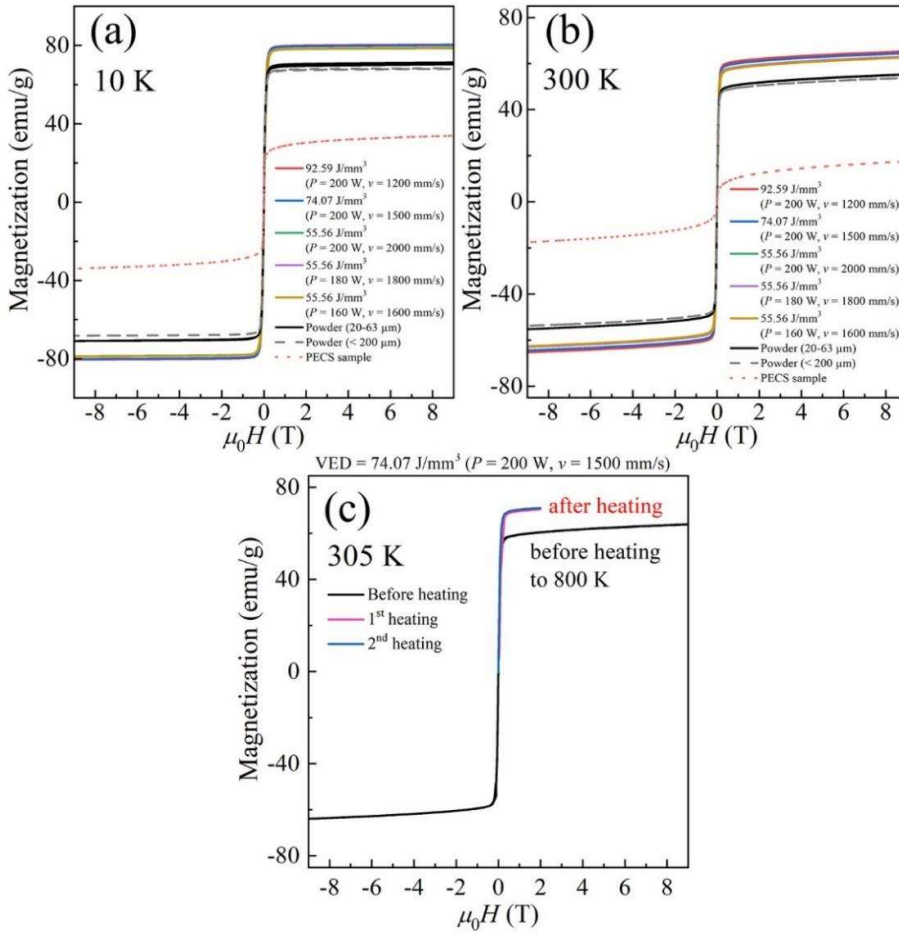


**Fig. 4.14.**  $M$ - $H$  curves of raw powder, SLM- and PECS-built  $\text{AlCoCr}_{0.75}\text{Cu}_{0.5}\text{FeNi}$  specimens determined at (a) 10 K and (b) 300 K. (c)  $M$ - $H$  curve at 305 K of one SLM-built specimen before and after heating to 800 K.

The temperature dependence of magnetization ( $M$ - $T$ ) has been investigated in a low field of 0.01 T, at temperatures in the range of 5 to 400 K, as shown in Fig. 4.15. Ferromagnetic transition does not occur in SLM-built specimens or powder, but only in PECS sample, in which the  $T_c$  is estimated to be 300 K. Distinctions in  $M$ - $T$  curves between powder and bulk samples are related to different demagnetization factors and susceptibility (**Publication III**).

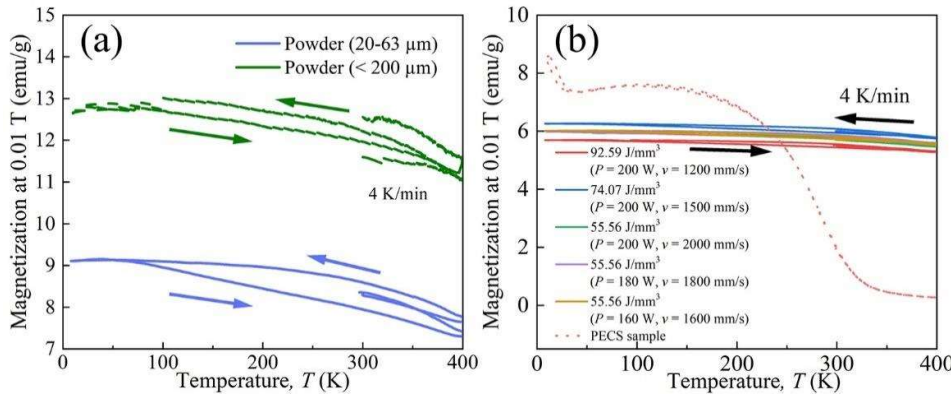


**Fig. 4.15.**  $M$ - $T$  curves of raw powder, SLM- and PECS-built  $\text{AlCoCr}_{0.75}\text{Cu}_{0.5}\text{FeNi}$  specimens evaluated at a temperature range from 10 to 400 K.

Fig. 4.16 presents the evolution of magnetization of one specimen fabricated by applying a VED of  $55.56 \text{ J/mm}^3$  ( $P = 180 \text{ W}$  and  $v = 1800 \text{ mm/s}$ ), which shows a similarly increased magnetization at 2 T and 305 K by  $\sim 15 \text{ emu/g}$ , when first heated to a temperature of 800 K and annealed for 10 minutes. While the magnetization does not increase significantly during the second heating, it is found to decrease noticeably as the temperature rises to 1000 K during the third heating. Three kinks during the cooling process in the third round are observed, and each  $T_c$  is indicated with a dashed line, which refers to phase transition. This is in agreement with former research on spray-cast equiatomic AlCoCrCuFeNi alloy, in which it was observed that the vanishment of decomposition structures occurred when heating up to 913 K [89].

The improved  $M_s$  when annealing at a temperature of 800 K for 10 minutes demonstrates that this temperature of 800 K lies within the miscibility gap of spinodal decomposition, and more A<sub>2</sub> structure is formed due to annealing (**Publication III**). Once the temperature is increased to 1000 K, it is not only above the range of miscibility gap, but also initiates the phase transitions (**Publication III**). Correspondingly,  $M_s$  is decreased when further heating to a temperature of 1000 K. This also explains the PECS sample exhibiting the lowest  $M_s$ , as it is sintered at a temperature of 1000 °C. Another reason for low  $M_s$  found in PECS sample is the formation of a mixing of FCC and BCC phase under a slow cooling rate of 100 °C/min, which concurs with the previous observations on AlCoCrCuFeNi based alloy produced traditionally by slow cooling rates [5,67].

It can be thus concluded, that in the solidification of AlCoCrCuFeNi based alloy, when the employed high cooling rate exceeds  $10^3 \text{ K/s}$ , spinodal decomposition into Fe-Cr enriched A<sub>2</sub> and Al-Ni enriched B<sub>2</sub> phase initiates. The formation of A<sub>2</sub> structure is promoted when the cooling rate is relatively low (but still  $\geq 10^3 \text{ K/s}$ ). Accordingly, ferromagnetism is enhanced (**Publication III**). The solidification under a low cooling rate such as in conventional casting is different, involving formation of dendrites and interdendrites (for details see **Publication III**).

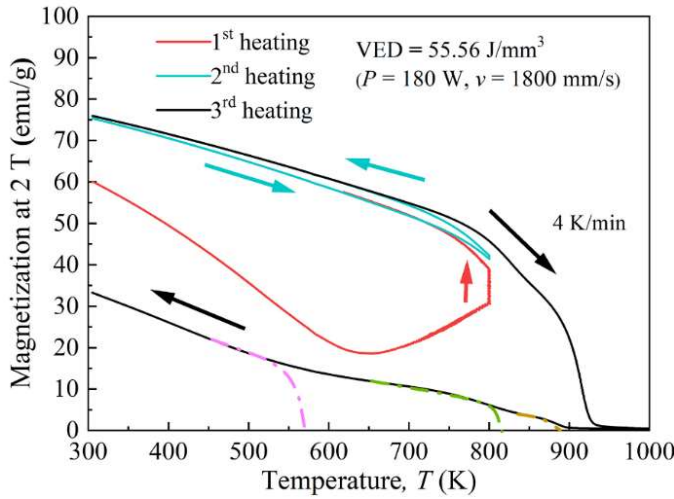


**Fig. 4.16.**  $M$ - $T$  curves of SLM-built AlCoCr<sub>0.75</sub>Cu<sub>0.5</sub>FeNi specimen measured in the range of temperature from 305 to 1000 K.



## 5. Conclusions

This thesis investigates the microstructure and properties of two types of Cr-Fe-Ni-based multicomponent alloys, i.e., equiatomic CrMnFeNi alloy and non-equiatomic AlCoCr<sub>0.75</sub>Cu<sub>0.5</sub>FeNi alloy, which are produced by SLM from corresponding gas-atomized powder. A reference for each alloy is also prepared by PECS for comparison. The influence of process parameters on the microstructure and properties has been explored. Moreover, for the equiatomic CrMnFeNi alloy targeting nuclear application scenarios, hydrogen-induced effects have been determined by characterizing the structure of hydrogen-charged TEM sample, and hydrogen uptake ability by TDS. For the AlCoCr<sub>0.75</sub>Cu<sub>0.5</sub>FeNi alloy aiming at functional applications, magnetic properties have been studied, particularly the magnetization associated with the degree of spinodal decomposition, which can be easily controlled in SLM by altering process parameters.

A single FCC structure is identified in the CrMnFeNi alloy produced by SLM, instead of a mixture of BCC and FCC phase detected in the starting powder, which has scarcely been reported before. The formation of a single FCC structure is attributed to RS during SLM process, in which the FCC structure formation is favored. The relative density of each SLM-built specimen reaches ~98%, and it is not evidently affected by the use of two different scanning speeds under the same laser power. The SLM process produces a hierarchical microstructure, including melt pools, grains, cell structures in forms of dendritic, elongated and equiaxed cells, and ultrafine sub-cells. Thermal gradient and time-varying process parameters result in a high density of dislocations concentrated in the grain boundaries and cell walls, and also within the cells. Segregation of Mn and Ni elements into the boundaries of melt pools and grains, as well as the cell walls, is ascribed to the relatively slow solidification of low melting point elements during SLM. In addition, SLM process creates sub-cell walls containing elemental segregation which usually reveal a large density of dislocations, while dislocations are also found in sub-cell walls but without segregation. Mn-rich and Mn-Cr-rich nano inclusions are observed, where the former is likely to form due to the recondensation of evaporated manganese, and the latter is related to the reaction with residual oxygen in equipment chamber. The rise of scanning speed when employing the same laser power corresponds to the decrease of VED, resulting in i) a larger amount of vacancies retained in the solid; ii) less loss of Mn element, due to the evaporation of volatile element during laser melting of powder; iii) smaller

cellular structures with less segregation of alloying elements and narrower cell walls, indicating that a more uniform and refined microstructure is produced; and iv) a higher Vickers hardness of  $248 \pm 8$  HV<sub>0.5</sub>. It is concluded that an essentially single phase CrMnFeNi alloy with a hierarchical and refined microstructure, and having high hardness, can be produced via SLM.

When hydrogen is electrochemically introduced into the SLM-built CrMnFeNi specimen, it leads to the formation of stacking faults, and cracks obviously due to the decline of stacking fault energy, similar to austenitic stainless steels. The absorbed hydrogen concentrations in SLM- and PECS-produced CrMnFeNi specimens are higher than that in conventional 316L steel, which is resulted from the high content of chromium and manganese, high lattice strain energy and short-range order, introduced by multicomponent alloy design strategy. SLM-built samples absorb more hydrogen than PECS sample and nearly twenty times more than 316L steel. This demonstrates that the multicomponent alloy design strategy and SLM result not only in large density of dislocations, and cellular structures with elemental segregation, but also contribute significantly towards absorption of hydrogen. A small amount of BCC phase detected after TDS test is ascribed to the loss of manganese or hydrogen-induced phase transformation due to heating cycle.

Two sets of process parameters have been employed in the fabrication of AlCoCr<sub>0.75</sub>Cu<sub>0.5</sub>FeNi alloy, and the results can be summarized as follows: i) laser power contributes to melting of powder particles, thus affecting relative density, and accordingly mechanical properties; ii) scanning speed governs the microstructural formation including elemental distribution and scale of cellular structure; and iii) VED corresponds to effects induced by the combination of laser power and scanning speed. All parameters in SLM process should be deliberately optimized. The highest relative density achieved in SLM-built AlCoCr<sub>0.75</sub>Cu<sub>0.5</sub>FeNi specimens is ~97%. Porosity is mainly resulted from cracks, lack-of-fusion, and gas pores. Cracks are caused by internal stress and localized strains produced by SLM, lack-of-fusion is due to insufficient laser power, and gas pores are ascribed to vaporization of volatile elements when melting the powder by laser. SLM process introduces a typical rapidly solidified hierarchical microstructure, including equiaxed grains and cellular structures on xy-plane, and elongated versions of them on xz-plane. The investigated variations of process parameters do not result in severe aluminum loss, and a similar small loss of aluminum is observed among all SLM-built AlCoCr<sub>0.75</sub>Cu<sub>0.5</sub>FeNi specimens. This is attributed to the vaporization of the most volatile element in laser melting of the powder. The employed process parameters neither introduce elemental segregations, as homogeneous elemental distributions are detected even in the specimen produced with the slowest scanning speed. The highest microhardness of  $604.6 \pm 6.8$  HV<sub>0.05</sub> is reached on xy-plane of the specimen produced by adopting the highest VED input of  $92.59$  J/mm<sup>3</sup> (corresponding to laser power of 200 W and scanning speed of 1200 mm/s). Employing a higher scanning speed under the same laser power leads to the formation of smaller grains and finer cellular structures, but also higher internal stresses.

Most importantly, the spinodal decomposition into BCC A2 phase and BCC B2 phase is found to be dependent on cooling rate, i.e., the formation of Fe-Cr-rich A2 structure is suppressed, and more Al-Ni-rich B2 phase is produced under a higher cooling rate. As a result, the highest  $M_s$  of 65.3 emu/g at 9 T and 300 K is produced at the lowest scanning speed, and the value of  $M_s$  is decreased as the scanning speed is increased under the same laser power. Alteration of scanning speed under the same laser power corresponds to varying cooling rates during solidification, and accordingly, the degree of spinodal decomposition can be controlled by altering the process parameters in SLM process. In addition,  $M_s$  is further improved when the formation of A2 phase is promoted by annealing the sample at a temperature that falls into the miscibility gap of spinodal decomposition. It is concluded that the magnetic properties of the alloy can be tailored via spinodal decomposition even locally, which can be easily carried out with the greater controllability of SLM, and without the need for time-consuming post treatments. This strategy broadens the application of SLM technique, and contributes to the innovations of functional materials.

More investigations on these two alloys are needed to acquire a better understanding and a deeper knowledge of the microstructure and properties. One of the interesting and crucial topics is to find the optimized process parameters which can bring full density to the final productions. Regarding the CrMnFeNi alloy, its performance for specific environments such as nuclear power plants can be evaluated. Other interstitial atoms such as nitrogen, boron and carbon can be introduced into it, and their influence on physical and chemical properties can be evaluated. For AlCoCr<sub>0.75</sub>Cu<sub>0.5</sub>FeNi alloy, the relationship between spinodal decomposition, cooling rate and process parameter can be systematically established. Concerning further research on multicomponent alloys, SLM technique, as well as other additive manufacturing methods, are recommended. This combination between multicomponent alloys and additive manufacturing provides a promising foreground for the future to come.



## References

- [1] ASM Handbook Committee, Properties and Selection: Irons, Steels, and High-Performance Alloys, ASM International, 1990.  
<https://doi.org/10.31399/asm.hb.v01.9781627081610>.
- [2] M.C. Gao, J.-W. Yeh, P.K. Liaw, Y. Zhang, eds., High-Entropy Alloys, Springer International Publishing, Cham, 2016.  
<https://doi.org/10.1007/978-3-319-27013-5>.
- [3] B. Cantor, I.T.H. Chang, P. Knight, A.J.B. Vincent, Microstructural development in equiatomic multicomponent alloys, *Mater. Sci. Eng. A.* 375–377 (2004) 213–218. <https://doi.org/10.1016/j.msea.2003.10.257>.
- [4] P.-K. Huang, J.-W. Yeh, T.-T. Shun, S.-K. Chen, Multi-Principal-Element Alloys with Improved Oxidation and Wear Resistance for Thermal Spray Coating, *Adv. Eng. Mater.* 6 (2004) 74–78.  
<https://doi.org/10.1002/adem.200300507>.
- [5] J.-W. Yeh, S.-K. Chen, S.-J. Lin, J.-Y. Gan, T.-S. Chin, T.-T. Shun, C.-H. Tsau, S.-Y. Chang, Nanostructured High-Entropy Alloys with Multiple Principal Elements: Novel Alloy Design Concepts and Outcomes, *Adv. Eng. Mater.* 6 (2004) 299–303.  
<https://doi.org/10.1002/adem.200300567>.
- [6] C.-Y. Hsu, J.-W. Yeh, S.-K. Chen, T.-T. Shun, Wear resistance and high-temperature compression strength of Fcc CuCoNiCrAl<sub>0.5</sub>Fe alloy with boron addition, *Metall. Mater. Trans. A.* 35 (2004) 1465–1469.  
<https://doi.org/10.1007/s11661-004-0254-x>.
- [7] E.P. George, D. Raabe, R.O. Ritchie, High-entropy alloys, *Nat. Rev. Mater.* 4 (2019) 515–534. <https://doi.org/10.1038/s41578-019-0121-4>.
- [8] Y.-F. Kao, S.-K. Chen, T.-J. Chen, P.-C. Chu, J.-W. Yeh, S.-J. Lin, Electrical, magnetic, and Hall properties of Al<sub>x</sub>CoCrFeNi high-entropy alloys, *J. Alloys Compd.* 509 (2011) 1607–1614.  
<https://doi.org/10.1016/j.jallcom.2010.10.210>.
- [9] C.-C. Tung, J.-W. Yeh, T. Shun, S.-K. Chen, Y.-S. Huang, H.-C. Chen, On the elemental effect of AlCoCrCuFeNi high-entropy alloy system, *Mater. Lett.* 61 (2007) 1–5. <https://doi.org/10.1016/j.matlet.2006.03.140>.
- [10] J.W. Elmer, S.M. Allen, T.W. Eagar, Microstructural development during solidification of stainless steel alloys, *Metall. Trans. A.* 20 (1989) 2117–2131. <https://doi.org/10.1007/BF02650298>.
- [11] H. Ocken, Reducing the Cobalt Inventory in Light Water Reactors, *Nucl. Technol.* 68 (1985) 18–28. <https://doi.org/10.13182/NT85-A33563>.
- [12] Z. Wu, H. Bei, Microstructures and mechanical properties of compositionally complex Co-free FeNiMnCr<sub>18</sub> FCC solid solution alloy, *Mater. Sci. Eng. A.* 640 (2015) 217–224.  
<https://doi.org/10.1016/j.msea.2015.05.097>.
- [13] N.A.P.K. Kumar, C. Li, K.J. Leonard, H. Bei, S.J. Zinkle, Microstructural stability and mechanical behavior of FeNiMnCr high entropy alloy under ion irradiation, *Acta Mater.* 113 (2016) 230–244.  
<https://doi.org/10.1016/j.actamat.2016.05.007>.

- [14] M. Ogura, T. Fukushima, R. Zeller, P.H. Dederichs, Structure of the high-entropy alloy Al CrFeCoNi: fcc versus bcc, *J. Alloys Compd.* 715 (2017) 454–459. <https://doi.org/10.1016/j.jallcom.2017.04.318>.
- [15] S. Singh, N. Wanderka, B.S. Murty, U. Glatzel, J. Banhart, Decomposition in multi-component AlCoCrCuFeNi high-entropy alloy, *Acta Mater.* 59 (2011) 182–190. <https://doi.org/10.1016/j.actamat.2010.09.023>.
- [16] E.J. Lavernia, T.S. Srivatsan, The rapid solidification processing of materials: science, principles, technology, advances, and applications, *J. Mater. Sci.* 45 (2010) 287–325. <https://doi.org/10.1007/s10853-009-3995-5>.
- [17] S.K. Das, L.A. Davis, High performance aerospace alloys via rapid solidification processing, *Mater. Sci. Eng.* 98 (1988) 1–12. [https://doi.org/10.1016/0025-5416\(88\)90116-4](https://doi.org/10.1016/0025-5416(88)90116-4).
- [18] S. Kumar, Additive Manufacturing Processes, Springer International Publishing, Cham, 2020. <https://doi.org/10.1007/978-3-030-45089-2>.
- [19] Y. Brif, M. Thomas, I. Todd, The use of high-entropy alloys in additive manufacturing, *Scr. Mater.* 99 (2015) 93–96. <https://doi.org/10.1016/j.scriptamat.2014.11.037>.
- [20] U. Fritsching, V. Uhlenwinkel, Hybrid Gas Atomization for Powder Production, in: K. Kondoh (Ed.), *Powder Metall.*, InTech, 2012. <https://doi.org/10.5772/35807>.
- [21] Y. Zhang, Y.J. Zhou, J.P. Lin, G.L. Chen, P.K. Liaw, Solid-Solution Phase Formation Rules for Multi-component Alloys, *Adv. Eng. Mater.* 10 (2008) 534–538. <https://doi.org/10.1002/adem.200700240>.
- [22] A. Gali, E.P. George, Tensile properties of high- and medium-entropy alloys, *Intermetallics.* 39 (2013) 74–78. <https://doi.org/10.1016/j.intermet.2013.03.018>.
- [23] F. Otto, Y. Yang, H. Bei, E.P. George, Relative effects of enthalpy and entropy on the phase stability of equiatomic high-entropy alloys, *Acta Mater.* 61 (2013) 2628–2638. <https://doi.org/10.1016/j.actamat.2013.01.042>.
- [24] D.B. Miracle, O.N. Senkov, A critical review of high entropy alloys and related concepts, *Acta Mater.* 122 (2017) 448–511. <https://doi.org/10.1016/j.actamat.2016.08.081>.
- [25] C. Li, X. Hu, T. Yang, N.K. Kumar, B.D. Wirth, S.J. Zinkle, Neutron irradiation response of a Co-free high entropy alloy, *J. Nucl. Mater.* 527 (2019) 151838. <https://doi.org/10.1016/j.jnucmat.2019.151838>.
- [26] C. Li, J. Yin, K. Odbadrakh, B.C. Sales, S.J. Zinkle, G.M. Stocks, B.D. Wirth, First principle study of magnetism and vacancy energetics in a near equimolar NiFeMnCr high entropy alloy, *J. Appl. Phys.* 125 (2019) 155103. <https://doi.org/10.1063/1.5086172>.
- [27] M. Fedorov, J.S. Wróbel, A. Fernández-Caballero, K.J. Kurzydłowski, D. Nguyen-Manh, Phase stability and magnetic properties in fcc Fe–Cr–Mn–Ni alloys from first-principles modeling, *Phys. Rev. B.* 101 (2020) 174416. <https://doi.org/10.1103/PhysRevB.101.174416>.
- [28] N.D. Stepanov, D.G. Shaysultanov, M.A. Tikhonovsky, G.A. Salishchev, Tensile properties of the Cr–Fe–Ni–Mn non-equiatomic multicomponent alloys with different Cr contents, *Mater. Des.* 87 (2015) 60–65. <https://doi.org/10.1016/j.matdes.2015.08.007>.
- [29] R.K. Nutor, M. Azeemullah, Q.P. Cao, X.D. Wang, D.X. Zhang, J.Z. Jiang, Microstructure and properties of a Co-free Fe<sub>50</sub>Mn<sub>27</sub>Ni<sub>10</sub>Cr<sub>13</sub> high entropy alloy, *J. Alloys Compd.* 851 (2021) 156842. <https://doi.org/10.1016/j.jallcom.2020.156842>.
- [30] Y. Zhang, H. Wu, X. Yu, D. Tang, R. Yuan, H. Sun, Microstructural evolution and strengthening mechanisms in Cr<sub>x</sub>MnFeNi high-entropy

- alloy, J. Mater. Res. Technol. 12 (2021) 2114–2127.  
<https://doi.org/10.1016/j.jmrt.2021.04.020>.
- [31] J. Dong, X. Feng, X. Hao, W. Kuang, The environmental degradation behavior of FeNiMnCr high entropy alloy in high temperature hydrogenated water, Scr. Mater. 204 (2021) 114127.  
<https://doi.org/10.1016/j.scriptamat.2021.114127>.
- [32] V. Raghavan, Effect of manganese on the stability of austenite in Fe-Cr-Ni alloys, Metall. Mater. Trans. A. 26 (1995) 237–242.  
<https://doi.org/10.1007/BF02664662>.
- [33] B.B. Bian, N. Guo, H.J. Yang, R.P. Guo, L. Yang, Y.C. Wu, J.W. Qiao, A novel cobalt-free FeMnCrNi medium-entropy alloy with exceptional yield strength and ductility at cryogenic temperature, J. Alloys Compd. 827 (2020) 153981. <https://doi.org/10.1016/j.jallcom.2020.153981>.
- [34] W.E. King, A.T. Anderson, R.M. Ferencz, N.E. Hodge, C. Kamath, S.A. Khairallah, A.M. Rubenchik, Laser powder bed fusion additive manufacturing of metals; physics, computational, and materials challenges, Appl. Phys. Rev. 2 (2015) 041304.  
<https://doi.org/10.1063/1.4937809>.
- [35] J.P. Kruth, L. Froyen, J. Van Vaerenbergh, P. Mercelis, M. Rombouts, B. Lauwers, Selective laser melting of iron-based powder, J. Mater. Process. Technol. 149 (2004) 616–622.  
<https://doi.org/10.1016/j.jmatprotec.2003.11.051>.
- [36] J. Kruth, P. Mercelis, J. Van Vaerenbergh, L. Froyen, M. Rombouts, Binding mechanisms in selective laser sintering and selective laser melting, Rapid Prototyp. J. 11 (2005) 26–36.  
<https://doi.org/10.1108/13552540510573365>.
- [37] P. Mercelis, J. Kruth, Residual stresses in selective laser sintering and selective laser melting, Rapid Prototyp. J. 12 (2006) 254–265.  
<https://doi.org/10.1108/13552540610707013>.
- [38] L. Thijs, F. Verhaeghe, T. Craeghs, J.V. Humbeeck, J.-P. Kruth, A study of the microstructural evolution during selective laser melting of Ti–6Al–4V, Acta Mater. 58 (2010) 3303–3312.  
<https://doi.org/10.1016/j.actamat.2010.02.004>.
- [39] K. Kempen, E. Yasa, L. Thijs, J.-P. Kruth, J. Van Humbeeck, Microstructure and mechanical properties of Selective Laser Melted 18Ni-300 steel, Phys. Procedia. 12 (2011) 255–263.  
<https://doi.org/10.1016/j.phpro.2011.03.033>.
- [40] R. Li, P. Niu, T. Yuan, P. Cao, C. Chen, K. Zhou, Selective laser melting of an equiatomic CoCrFeMnNi high-entropy alloy: Processability, non-equilibrium microstructure and mechanical property, J. Alloys Compd. 746 (2018) 125–134. <https://doi.org/10.1016/j.jallcom.2018.02.298>.
- [41] Z.G. Zhu, Q.B. Nguyen, F.L. Ng, X.H. An, X.Z. Liao, P.K. Liaw, S.M.L. Nai, J. Wei, Hierarchical microstructure and strengthening mechanisms of a CoCrFeNiMn high entropy alloy additively manufactured by selective laser melting, Scr. Mater. 154 (2018) 20–24.  
<https://doi.org/10.1016/j.scriptamat.2018.05.015>.
- [42] Y. Zhong, L. Liu, S. Wikman, D. Cui, Z. Shen, Intragranular cellular segregation network structure strengthening 316L stainless steel prepared by selective laser melting, J. Nucl. Mater. 470 (2016) 170–178.  
<https://doi.org/10.1016/j.jnucmat.2015.12.034>.
- [43] Y.M. Wang, T. Voisin, J.T. McKeown, J. Ye, N.P. Calta, Z. Li, Z. Zeng, Y. Zhang, W. Chen, T.T. Roehling, R.T. Ott, M.K. Santala, P.J. Depond, M.J. Matthews, A.V. Hamza, T. Zhu, Additively manufactured hierarchical stainless steels with high strength and ductility, Nat. Mater. 17 (2018) 63–71. <https://doi.org/10.1038/nmat5021>.
- [44] L. Liu, Q. Ding, Y. Zhong, J. Zou, J. Wu, Y.-L. Chiu, J. Li, Z. Zhang, Q. Yu, Z. Shen, Dislocation network in additive manufactured steel breaks

- strength–ductility trade-off, *Mater. Today.* 21 (2018) 354–361.  
<https://doi.org/10.1016/j.mattod.2017.11.004>.
- [45] R.W. Hertzberg, R.P. Vinci, J.L. Hertzberg, Deformation and fracture mechanics of engineering materials, 5th Edition, John Wiley & Sons, 2020.
- [46] J. Lehtonen, Y. Ge, N. Ciftci, O. Heczko, V. Uhlenwinkel, S.-P. Hannula, Phase structures of gas atomized equiatomic CrFeNiMn high entropy alloy powder, *J. Alloys Compd.* 827 (2020) 154142.  
<https://doi.org/10.1016/j.jallcom.2020.154142>.
- [47] M. Suarez, A. Fernandez, J.L. Menendez, R. Torrecillas, H. U., J. Hennicke, R. Kirchner, T. Kessel, Challenges and Opportunities for Spark Plasma Sintering: A Key Technology for a New Generation of Materials, in: B. Ertug (Ed.), *Sinter. Appl.*, InTech, 2013.  
<https://doi.org/10.5772/53706>.
- [48] V. Mamedov, Spark plasma sintering as advanced PM sintering method, *Powder Metall.* 45 (2002) 322–328.  
<https://doi.org/10.1179/003258902225007041>.
- [49] R.K. Dayal, N. Parvathavarthini, Hydrogen embrittlement in power plant steels, *Sadhana.* 28 (2003) 431–451.  
<https://doi.org/10.1007/BF02706442>.
- [50] G.A. Young, E. Richey, D.S. Morton, Hydrogen embrittlement in nuclear power systems, in: *Gaseous Hydrog. Embrittlement Mater. Energy Technol.*, Elsevier, 2012: pp. 149–176.  
<https://doi.org/10.1533/9780857093899.1.149>.
- [51] A. Turnbull, R.B. Hutchings, D.H. Ferriss, Modelling of thermal desorption of hydrogen from metals, *Mater. Sci. Eng. A.* 238 (1997) 317–328. [https://doi.org/10.1016/S0921-5093\(97\)00426-7](https://doi.org/10.1016/S0921-5093(97)00426-7).
- [52] Y. Yagodzinsky, T. Saukkonen, S. Kilpeläinen, F. Tuomisto, H. Hänninen, Effect of hydrogen on plastic strain localization in single crystals of austenitic stainless steel, *Scr. Mater.* 62 (2010) 155–158.  
<https://doi.org/10.1016/j.scriptamat.2009.10.005>.
- [53] G. Hultquist, M.J. Graham, J.L. Smialek, B. Jönsson, Hydrogen in metals studied by Thermal Desorption Spectroscopy (TDS), *Corros. Sci.* 93 (2015) 324–326. <https://doi.org/10.1016/j.corsci.2015.01.003>.
- [54] H. Luo, Z. Li, D. Raabe, Hydrogen enhances strength and ductility of an equiatomic high-entropy alloy, *Sci. Rep.* 7 (2017).  
<https://doi.org/10.1038/s41598-017-10774-4>.
- [55] H. Luo, W. Lu, X. Fang, D. Ponge, Z. Li, D. Raabe, Beating hydrogen with its own weapon: Nano-twin gradients enhance embrittlement resistance of a high-entropy alloy, *Mater. Today.* 21 (2018) 1003–1009.  
<https://doi.org/10.1016/j.mattod.2018.07.015>.
- [56] H. Luo, Z. Li, W. Lu, D. Ponge, D. Raabe, Hydrogen embrittlement of an interstitial equimolar high-entropy alloy, *Corros. Sci.* 136 (2018) 403–408. <https://doi.org/10.1016/j.corsci.2018.03.040>.
- [57] A.J. Zaddach, C. Niu, C.C. Koch, D.L. Irving, Mechanical Properties and Stacking Fault Energies of NiFeCrCoMn High-Entropy Alloy, *JOM.* 65 (2013) 1780–1789. <https://doi.org/10.1007/s11837-013-0771-4>.
- [58] Y. Zhao, D.-H. Lee, J.-A. Lee, W.-J. Kim, H.N. Han, U. Ramamurty, J.-Y. Suh, J. Jang, Hydrogen-Induced Nanohardness Variations in a CoCrFeMnNi High-Entropy Alloy, *Int. J. Hydrog. Energy.* 42 (2017) 12015–12021. <https://doi.org/10.1016/j.ijhydene.2017.02.061>.
- [59] Y. Zhao, D.-H. Lee, M.-Y. Seok, J.-A. Lee, M.P. Phaniraj, J.-Y. Suh, H.-Y. Ha, J.-Y. Kim, U. Ramamurty, J. Jang, Resistance of CoCrFeMnNi high-entropy alloy to gaseous hydrogen embrittlement, *Scr. Mater.* 135 (2017) 54–58. <https://doi.org/10.1016/j.scriptamat.2017.03.029>.
- [60] K.E. Nygren, K.M. Bertsch, S. Wang, H. Bei, A. Nagao, I.M. Robertson, Hydrogen embrittlement in compositionally complex FeNiCoCrMn FCC

- solid solution alloy, *Curr. Opin. Solid State Mater. Sci.* (2017). <https://doi.org/10.1016/j.cossms.2017.11.002>.
- [61] D.-H. Lee, B. Sun, S. Lee, D. Ponge, E.A. Jägle, D. Raabe, Comparative study of hydrogen embrittlement resistance between additively and conventionally manufactured 304L austenitic stainless steels, *Mater. Sci. Eng. A.* 803 (2021) 140499. <https://doi.org/10.1016/j.msea.2020.140499>.
- [62] J.-M. Park, Y. Zhao, T. Voisin, D.-H. Lee, S. Komazaki, Y. Ko, D.-I. Kim, J.-Y. Suh, H.N. Han, Y.M. Wang, U. Ramamurty, J. Jang, Hydrogen uptake and its influence in selective laser melted austenitic stainless steel: A nanoindentation study, *Scr. Mater.* 194 (2021) 113718. <https://doi.org/10.1016/j.scriptamat.2020.113718>.
- [63] J. Lin, F. Chen, F. Liu, D. Xu, J. Gao, X. Tang, Hydrogen permeation behavior and hydrogen-induced defects in 316L stainless steels manufactured by additive manufacturing, *Mater. Chem. Phys.* 250 (2020) 123038. <https://doi.org/10.1016/j.matchemphys.2020.123038>.
- [64] D. Kong, C. Dong, X. Ni, L. Zhang, H. Luo, R. Li, L. Wang, C. Man, X. Li, Superior resistance to hydrogen damage for selective laser melted 316L stainless steel in a proton exchange membrane fuel cell environment, *Corros. Sci.* 166 (2020) 108425. <https://doi.org/10.1016/j.corsci.2019.108425>.
- [65] Y.-K. Kim, J.-Y. Suh, K.-A. Lee, Effect of gaseous hydrogen embrittlement on the mechanical properties of additively manufactured CrMnFeCoNi high-entropy alloy strengthened by in-situ formed oxide, *Mater. Sci. Eng. A.* 796 (2020) 140039. <https://doi.org/10.1016/j.msea.2020.140039>.
- [66] Z. Fu, B. Yang, K. Gan, D. Yan, Z. Li, G. Gou, H. Chen, Z. Wang, Improving the hydrogen embrittlement resistance of a selective laser melted high-entropy alloy via modifying the cellular structures, *Corros. Sci.* 190 (2021) 109695. <https://doi.org/10.1016/j.corsci.2021.109695>.
- [67] C.-J. Tong, Y.-L. Chen, J.-W. Yeh, S.-J. Lin, S.-K. Chen, T.-T. Shun, C.-H. Tsau, S.-Y. Chang, Microstructure characterization of Al<sub>x</sub>CoCrCuFeNi high-entropy alloy system with multiprincipal elements, *Metall. Mater. Trans. A.* 36 (2005) 881–893. <https://doi.org/10.1007/s11661-005-0283-0>.
- [68] Y.J. Zhou, Y. Zhang, F.J. Wang, G.L. Chen, Phase transformation induced by lattice distortion in multiprincipal component CoCrFeNiCuxAl<sub>1-x</sub> solid-solution alloys, *Appl. Phys. Lett.* 92 (2008) 241917. <https://doi.org/10.1063/1.2938690>.
- [69] K.B. Zhang, Z.Y. Fu, J.Y. Zhang, J. Shi, W.M. Wang, H. Wang, Y.C. Wang, Q.J. Zhang, Annealing on the structure and properties evolution of the CoCrFeNiCuAl high-entropy alloy, *J. Alloys Compd.* 502 (2010) 295–299. <https://doi.org/10.1016/j.jallcom.2009.11.104>.
- [70] A.V. Kuznetsov, D.G. Shaysultanov, N.D. Stepanov, G.A. Salishchev, O.N. Senkov, Tensile properties of an AlCrCuNiFeCo high-entropy alloy in as-cast and wrought conditions, *Mater. Sci. Eng. A.* 533 (2012) 107–118. <https://doi.org/10.1016/j.msea.2011.11.045>.
- [71] M.V. Ivchenko, V.G. Pushin, A.N. Uksusnikov, N. Wanderka, N.I. Kourov, Specific features of cast high-entropy AlCrFeCoNiCu alloys produced by ultrarapid quenching from the melt, *Phys. Met. Metallogr.* 114 (2013) 503–513. <https://doi.org/10.1134/S0031918X13060057>.
- [72] Z. Tang, M.C. Gao, H. Diao, T. Yang, J. Liu, T. Zuo, Y. Zhang, Z. Lu, Y. Cheng, Y. Zhang, K.A. Dahmen, P.K. Liaw, T. Egami, Aluminum Alloying Effects on Lattice Types, Microstructures, and Mechanical Behavior of High-Entropy Alloys Systems, *JOM.* 65 (2013) 1848–1858. <https://doi.org/10.1007/s11837-013-0776-z>.

- [73] K. Zhang, Z. Fu, Effects of annealing treatment on phase composition and microstructure of CoCrFeNiTiAl<sub>x</sub> high-entropy alloys, *Intermetallics*. 22 (2012) 24–32. <https://doi.org/10.1016/j.intermet.2011.10.010>.
- [74] J.Y. He, W.H. Liu, H. Wang, Y. Wu, X.J. Liu, T.G. Nieh, Z.P. Lu, Effects of Al addition on structural evolution and tensile properties of the FeCoNiCrMn high-entropy alloy system, *Acta Mater.* 62 (2014) 105–113. <https://doi.org/10.1016/j.actamat.2013.09.037>.
- [75] Y. Qiu, S. Thomas, D. Fabijanic, A.J. Barlow, H.L. Fraser, N. Birbilis, Microstructural evolution, electrochemical and corrosion properties of Al CoCrFeNiTi high entropy alloys, *Mater. Des.* 170 (2019) 107698. <https://doi.org/10.1016/j.matdes.2019.107698>.
- [76] C. Miclea, C. Tanasoiu, C.F. Miclea, A. Gheorghiu, V. Tanasoiu, Soft ferrite materials for magnetic temperature transducers and applications, *J. Magn. Magn. Mater.* 290–291 (2005) 1506–1509. <https://doi.org/10.1016/j.jmmm.2004.11.561>.
- [77] S. Singh, N. Wanderka, K. Kiefer, K. Siemensmeyer, J. Banhart, Effect of decomposition of the Cr–Fe–Co rich phase of AlCoCrCuFeNi high-entropy alloy on magnetic properties, *Ultramicroscopy*. 111 (2011) 619–622. <https://doi.org/10.1016/j.ultramic.2010.12.001>.
- [78] M.-R. Chen, S.-J. Lin, J.-W. Yeh, S.-K. Chen, Y.-S. Huang, C.-P. Tu, Microstructure and Properties of Al<sub>0.5</sub>CoCrCuFeNiTi<sub>x</sub> (x = 0–2.0) High-Entropy Alloys, *Mater. Trans.* 47 (2006) 1395–1401. <https://doi.org/10.2320/matertrans.47.1395>.
- [79] M.-R. Chen, S.-J. Lin, J.-W. Yeh, M.-H. Chuang, S.-K. Chen, Y.-S. Huang, Effect of vanadium addition on the microstructure, hardness, and wear resistance of Al<sub>0.5</sub>CoCrCuFeNi high-entropy alloy, *Mater. Trans. A*. 37 (2006) 1363–1369. <https://doi.org/10.1007/s11661-006-0081-3>.
- [80] X. Liu, W. Lei, L. Ma, J. Liu, J. Liu, J. Cui, On the microstructures, phase assemblages and properties of Al<sub>0.5</sub>CoCrCuFeNiSix high-entropy alloys, *J. Alloys Compd.* 630 (2015) 151–157. <https://doi.org/10.1016/j.jallcom.2014.11.085>.
- [81] S. Luo, P. Gao, H. Yu, J. Yang, Z. Wang, X. Zeng, Selective laser melting of an equiatomic AlCrCuFeNi high-entropy alloy: Processability, non-equilibrium microstructure and mechanical behavior, *J. Alloys Compd.* 771 (2019) 387–397. <https://doi.org/10.1016/j.jallcom.2018.08.290>.
- [82] M. Zhang, X. Zhou, D. Wang, W. Zhu, J. Li, Y.F. Zhao, AlCoCuFeNi high-entropy alloy with tailored microstructure and outstanding compressive properties fabricated via selective laser melting with heat treatment, *Mater. Sci. Eng. A*. 743 (2019) 773–784. <https://doi.org/10.1016/j.msea.2018.11.118>.
- [83] P.D. Niu, R.D. Li, T.C. Yuan, S.Y. Zhu, C. Chen, M.B. Wang, L. Huang, Microstructures and properties of an equimolar AlCoCrFeNi high-entropy alloy printed by selective laser melting, *Intermetallics*. 104 (2019) 24–32. <https://doi.org/10.1016/j.intermet.2018.10.018>.
- [84] H.Y. Jung, N.J. Peter, E. Gärtner, G. Dehm, V. Uhlenwinkel, E.A. Jägle, Bulk nanostructured AlCoCrFeMnNi chemically complex alloy synthesized by laser-powder bed fusion, *Addit. Manuf.* 35 (2020) 101337. <https://doi.org/10.1016/j.addma.2020.101337>.
- [85] T.G. Novak, H.D. Vora, R.S. Mishra, M.L. Young, N.B. Dahotre, Synthesis of Al<sub>0.5</sub>CoCrCuFeNi and Al<sub>0.5</sub>CoCrFeMnNi High-Entropy Alloys by Laser Melting, *Metall. Mater. Trans. B*. 45 (2014) 1603–1607. <https://doi.org/10.1007/s11663-014-0170-4>.
- [86] Y. Wang, R. Li, P. Niu, Z. Zhang, T. Yuan, J. Yuan, K. Li, Microstructures and properties of equimolar AlCoCrCuFeNi high-entropy alloy additively manufactured by selective laser melting,

- Intermetallics. 120 (2020) 106746.  
<https://doi.org/10.1016/j.intermet.2020.106746>.
- [87] A. Sonawane, G. Roux, J.-J. Blandin, A. Despres, G. Martin, Cracking mechanism and its sensitivity to processing conditions during laser powder bed fusion of a structural aluminum alloy, *Materialia*. 15 (2021) 100976. <https://doi.org/10.1016/j.mtla.2020.100976>.
- [88] V.C. Srivastava, G.K. Mandal, N. Ciftci, V. Uhlenwinkel, L. Mädler, Processing of High-Entropy AlCoCr<sub>0.75</sub>Cu<sub>0.5</sub>FeNi Alloy by Spray Forming, *J. Mater. Eng. Perform.* 26 (2017) 5906–5920. <https://doi.org/10.1007/s11665-017-3071-2>.
- [89] Y. Zhang, Z. Chen, D. Cao, J. Zhang, P. Zhang, Q. Tao, X. Yang, Concurrence of spinodal decomposition and nano-phase precipitation in a multi-component AlCoCrCuFeNi high-entropy alloy, *J. Mater. Res. Technol.* 8 (2019) 726–736. <https://doi.org/10.1016/j.jmrt.2018.04.020>.
- [90] N.J. Peter, M.J. Duarte, C.H. Liebscher, V.C. Srivastava, V. Uhlenwinkel, E.A. Jägle, G. Dehm, Early stage phase separation of AlCoCr<sub>0.75</sub>Cu<sub>0.5</sub>FeNi high-entropy powder at the nanoscale, *J. Alloys Compd.* 820 (2020) 153149. <https://doi.org/10.1016/j.jallcom.2019.153149>.
- [91] U. Scipioni Bertoli, G. Guss, S. Wu, M.J. Matthews, J.M. Schoenung, In-situ characterization of laser-powder interaction and cooling rates through high-speed imaging of powder bed fusion additive manufacturing, *Mater. Des.* 135 (2017) 385–396. <https://doi.org/10.1016/j.matdes.2017.09.044>.
- [92] P.A. Hooper, Melt pool temperature and cooling rates in laser powder bed fusion, *Addit. Manuf.* 22 (2018) 548–559. <https://doi.org/10.1016/j.addma.2018.05.032>.
- [93] B.D. Cullity, C.D. Graham, *Introduction to magnetic materials*, John Wiley & Sons, Hoboken, New Jersey, 2011. <https://doi.org/10.1002/9780470386323>.
- [94] Z. Rao, B. Dutta, F. Körmann, W. Lu, X. Zhou, C. Liu, A.K. Silva, U. Wiedwald, M. Spasova, M. Farle, D. Ponge, B. Gault, J. Neugebauer, D. Raabe, Z. Li, Beyond Solid Solution High-Entropy Alloys: Tailoring Magnetic Properties via Spinodal Decomposition, *Adv. Funct. Mater.* 31 (2021) 2007668. <https://doi.org/10.1002/adfm.202007668>.
- [95] B. Liu, R. Wildman, C. Tuck, I. Ashcroft, R. Hague, Investigation the effect of particle size distribution on processing parameters optimisation in selective laser melting process, *Addit. Manuf. Res. Group Loughb. Univ.* (2011) 227–238.
- [96] C. Kamath, B. El-dasher, G.F. Gallegos, W.E. King, Density of additively-manufactured, 316L SS parts using laser powder-bed fusion at powers up to 400W, (2013) 21. <https://doi.org/10.2172/1116929>.
- [97] J.-P. Kruth, J. Deckers, E. Yasa, R. Wauthlé, Assessing and comparing influencing factors of residual stresses in selective laser melting using a novel analysis method, *Proc. Inst. Mech. Eng. Part B J. Eng. Manuf.* 226 (2012) 980–991. <https://doi.org/10.1177/0954405412437085>.
- [98] L.N. Carter, C. Martin, P.J. Withers, M.M. Attallah, The influence of the laser scan strategy on grain structure and cracking behaviour in SLM powder-bed fabricated nickel superalloy, *J. Alloys Compd.* 615 (2014) 338–347. <https://doi.org/10.1016/j.jallcom.2014.06.172>.
- [99] ISO Standard, 6507-1: 2018—Metallic Materials—Vickers Hardness Test—Part 1: Test Method, (2018).
- [100] B. Zhang, Y. Li, Q. Bai, Defect Formation Mechanisms in Selective Laser Melting: A Review, *Chin. J. Mech. Eng.* 30 (2017) 515–527. <https://doi.org/10.1007/s10033-017-0121-5>.

- [101] F. Nilsén, I.F. Ituarte, M. Salmi, J. Partanen, S.-P. Hannula, Effect of process parameters on non-modulated Ni-Mn-Ga alloy manufactured using powder bed fusion, *Addit. Manuf.* 28 (2019) 464–474.  
<https://doi.org/10.1016/j.addma.2019.05.029>.
- [102] T.F. Kelly, M. Cohen, J.B. Sande, Rapid solidification of a droplet-processed stainless steel, *Metall. Trans. A.* 15 (1984) 819–833.  
<https://doi.org/10.1007/BF02644556>.
- [103] F. Tuomisto, I. Makkonen, Defect identification in semiconductors with positron annihilation: Experiment and theory, *Rev. Mod. Phys.* 85 (2013) 1583–1631. <https://doi.org/10.1103/RevModPhys.85.1583>.
- [104] E. Lu, X. Cao, S. Jin, P. Zhang, C. Zhang, J. Yang, Y. Wu, L. Guo, B. Wang, Investigation of vacancy-type defects in helium irradiated FeCrNi alloy by slow positron beam, *J. Nucl. Mater.* 458 (2015) 240–244.  
<https://doi.org/10.1016/j.jnucmat.2014.12.070>.
- [105] G. Bi, C.-N. Sun, H. Chen, F.L. Ng, C.C.K. Ma, Microstructure and tensile properties of superalloy IN100 fabricated by micro-laser aided additive manufacturing, *Mater. Des.* 60 (2014) 401–408.  
<https://doi.org/10.1016/j.matdes.2014.04.020>.
- [106] E. Kannatey-Asibu, *Principles of Laser Materials Processing*, John Wiley & Sons, Inc., Hoboken, NJ, USA, 2009.  
<https://doi.org/10.1002/9780470459300>.
- [107] M.B. Whiteman, A.R. Troiano, The Influence of Hydrogen on the Stacking Fault Energy of an Austenitic Stainless Steel, *Phys. Status Solidi B.* 7 (1964) K109–K110.  
<https://doi.org/10.1002/pssb.19640070241>.
- [108] A.E. Pontini, J.D. Hermida, X-Ray diffraction measurement of the stacking fault energy reduction induced by hydrogen in an AISI 304 steel, *Scr. Mater.* 37 (1997) 1831–1837. [https://doi.org/10.1016/S1359-6462\(97\)00332-1](https://doi.org/10.1016/S1359-6462(97)00332-1).
- [109] D. Eliezer, D.G. Chakrapani, C.J. Altstetter, E.N. Pugh, The influence of austenite stability on the hydrogen embrittlement and stress-corrosion cracking of stainless steel, *Metall. Trans. A.* 10 (1979) 935–941.  
<https://doi.org/10.1007/BF02658313>.
- [110] P. Rozenak, D. Eliezer, Phase changes related to hydrogen-induced cracking in austenitic stainless steel, *Acta Metall.* 35 (1987) 2329–2340.  
[https://doi.org/10.1016/0001-6160\(87\)90081-2](https://doi.org/10.1016/0001-6160(87)90081-2).
- [111] N. Narita, C.J. Altstetter, H.K. Birnbaum, Hydrogen-related phase transformations in austenitic stainless steels, *Metall. Trans. A.* 13 (1982) 1355–1365. <https://doi.org/10.1007/BF02642872>.
- [112] I. Tamura, Deformation-induced martensitic transformation and transformation-induced plasticity in steels, *Met. Sci.* 16 (1982) 245–253.  
<https://doi.org/10.1179/030634582790427316>.
- [113] J. von Pezold, L. Lymerakis, J. Neugebeauer, Hydrogen-enhanced local plasticity at dilute bulk H concentrations: The role of H–H interactions and the formation of local hydrides, *Acta Mater.* 59 (2011) 2969–2980.  
<https://doi.org/10.1016/j.actamat.2011.01.037>.
- [114] J.H. Ryu, Y.S. Chun, C.S. Lee, H.K.D.H. Bhadeshia, D.W. Suh, Effect of deformation on hydrogen trapping and effusion in TRIP-assisted steel, *Acta Mater.* 60 (2012) 4085–4092.  
<https://doi.org/10.1016/j.actamat.2012.04.010>.
- [115] Y. Fukai, M. Mizutani, S. Yokota, M. Kanazawa, Y. Miura, T. Watanabe, Superabundant vacancy–hydrogen clusters in electrodeposited Ni and Cu, *Proc. Eighth Int. Symp. Met.-Hydrog. Syst. Fundam. Appl. MH2002*. 356–357 (2003) 270–273. [https://doi.org/10.1016/S0925-8388\(02\)01270-7](https://doi.org/10.1016/S0925-8388(02)01270-7).



ISBN 978-952-64-0652-7 (printed)

ISBN 978-952-64-0653-4 (pdf)

ISSN 1799-4934 (printed)

ISSN 1799-4942 (pdf)

**Aalto University**

**School of Chemical Engineering**

**Department of Chemistry and Materials Science**

[www.aalto.fi](http://www.aalto.fi)

**BUSINESS +  
ECONOMY**

**ART +  
DESIGN +  
ARCHITECTURE**

**SCIENCE +  
TECHNOLOGY**

**CROSSOVER**

**DOCTORAL  
DISSERTATIONS**